Technische Universität München
Max-Planck-Institut für extraterrestrische Physik
Garching bei München

Gamma rays from interactions of cosmic-ray electrons

Elena Orlando

Vollständiger Abdruck der von der Fakultät für Physik der Technischen Universität München zur Erlangung des akademischen Grades eines

Doktors der Naturwissenschaften

genehmigten Dissertation.

Vorsitzender:		Univ.–Prof. Dr. M. Ratz
Prüfer:	1.	Hon.–Prof. Dr. G. Hasinger
	2.	Univ.–Prof. Dr. F. von Feilitzsch

Die Dissertation wurde am 29.07.2008 bei der Technischen Universität München eingereicht und durch die Fakultät für Physik am 29.09.2008 angenommen.

Contents

Summary

This thesis is focused on the study of the diffuse gamma-ray emission from the Galaxy and the sources that contribute to it. It addresses mainly cosmic-ray electrons that propagate in the Galaxy and the solar system producing gamma-ray emission via inverse Compton scattering on the radiation fields. Part of this work is performed also using the GALPROP code. The last part of this thesis is focused on the radio emission from the Galaxy, which can constrain the cosmic-ray electron spectrum.

The first chapter gives an introduction to cosmic rays and an overview of the emission mechanisms from interaction of cosmic rays propagating in the Galaxy.

Because a large part of the Galactic optical luminosity comes from the most luminous stars, the second chapter of my work is focused on developing models of the inverse-Compton gamma rays produced near these stars. This emission is clumpy at some level, an effect which could be detectable by GLAST. This has not been considered in previous studies.

In the third chapter, I develop the model of the same process for the Sun, taking into account the solar modulation of the cosmic-ray electrons and a more precise formalism. The emission is predicted to be extended and also contributes to the diffuse Galactic background. I analyse and detect this extended emission from the Sun in the EGRET data, with a flux in agreement with my estimates. The analysis is performed taking into account the point sources coming at small angles to the Sun, and the Galactic diffuse background. This will clearly be of interest for the GLAST (Gamma-ray Large Area Telescope launched in June 2008) as well.

In the fourth chapter I investigate the diffuse Galactic gamma-ray emission and the propagation of cosmic-ray electrons in the Galaxy using gamma-ray and radio data, and the GALPROP code. This Chapter shows the contribution of inverse Compton emission by scattering of GeV cosmic-ray electrons on the interstellar radiation field to the hard X-ray and gamma ray emission from

the Galaxy. Finally it contains also the latest results of the implementation in GALPROP of the calculation of synchrotron emission from the Galaxy. The aim is to exploit synchrotron radiation in order to constrain the cosmic-ray electron spectrum and the Galactic magnetic field.

Chapter 1

Introduction

1.1 Cosmic-rays: an overview

In 1912 V. Hess discovered the cosmic-ray (CR) radiation with balloon flights, at an altitude of 5 km, from the observation that the ionisation in gases contained in closed vessels was higher than what observed at sea level (Hess (1932) and Hess (1922)). For 15 years cosmic rays were supposed to be very penetrating gamma rays of cosmic origin. R. Millikan in 1925 coined the term "Cosmic Rays". In 1927 it was discovered that the ionisation produced by cosmic rays depends on latitude. This geomagnetic effect confirmed that cosmic rays are charged particles and it was clear that the main role was played by protons. After 1948 it was found that CR are composed of nuclei of many elements.

About 90$\%$ of the cosmic ray nuclei are protons, about 9$\%$ are helium (alpha particles), and the contribution of all of the rest of the elements is only 1$\%$, including electrons. In this one percent there are very rare elements and isotopes.

Cosmic-ray spectrum extends from 100 MeV to beyond 10^{20} eV. Particles with energy below 100 MeV come from the Sun. Below 10 GeV the CR flux is modulated by the heliospheric magnetic fields. CR with energy below 10^{17}-10^{18} eV are believed to be of Galactic origin, while above those energies are considered to be of extra-galactic origin, since they can not be magnetically bound to the Galaxy. In fact a proton with energy above 10^{18} eV has a Larmor radius above 350 pc in a magnetic field of 3 μG, that is larger than the thickness of the Galactic disc. Around 10^{9}eV, 10^{14}eV and 10^{20}eV, fluxes of 1 m^{-2} s^{-1}, 1 m^{-2} yr^{-1} and 1 km^{-2} yr^{-1} are detected respectively.

The differential spectrum of CR is shown in Fig. 1.1. The spectrum of CR protons, electrons and nuclei can be described rather well by a power law

$$N(E)\, dE = k\, E^{-\alpha} dE \tag{1.1}$$

with α around -2.7 for energy range 10^9eV <E<10^{14}eV . These particles are of Galactic origin and supernovae shocks are the favoured candidates for producing them. Below 10^{10}eV nucleon^{-1} the shape of the CR spectrum is affected by solar modulation decreasing during periods of high solar activity and increasing during phases of low solar activity.

The break at 3×10^{15}eV is called the 'knee' where the value of the spectral index is around -3. Finally, above a few 10^{18}eV, at the highest energies there is a flattening in the slope, "ankle" with the slope around -2.7 again (Longair 1994).

Thus, the main part of primary CR reach the Earth from the interstellar space and are formed in our Galaxy with exception maybe of particles with energy above 10^{17} -10^{19} eV.

Galactic CR provide a direct sample of matter from outside the solar system. The Galactic magnetic field, the solar system, and the Earth distort the paths of these particles so that CR don't point back to their sources. Thus, determining where CR come from can only be made by indirect measurements such as their composition and abundances, since nuclear interactions imply that their composition contains information on their propagation.

CR produced and accelerated in the sources such as supernovae are called primaries, while those which are created by nuclear interaction of primary with nuclei of atoms and molecules of the interstellar gas (via spallation) are called secondaries.

The CR source composition and CR propagation history are related to their isotopic abundances. In fact, there is evidence that the CR composition is similar to that of the solar system, apart from secondaries. Figure 1.2 shows the element abundances of CR compared to the solar system radiation. For example, the lithium, beryllium and boron that are rare in the solar system, are abundant in CR (around 6 order of magnitude difference) and this fact proves the important role of propagation in the interstellar medium.

This abundance difference is a result of how secondary CR are formed. After spallation of heavy nuclei components of primary cosmic rays, namely the carbon and oxygen nuclei, with interstellar medium, lithium, beryllium and boron are produced. Hence the destruction of primary nuclei via spallation

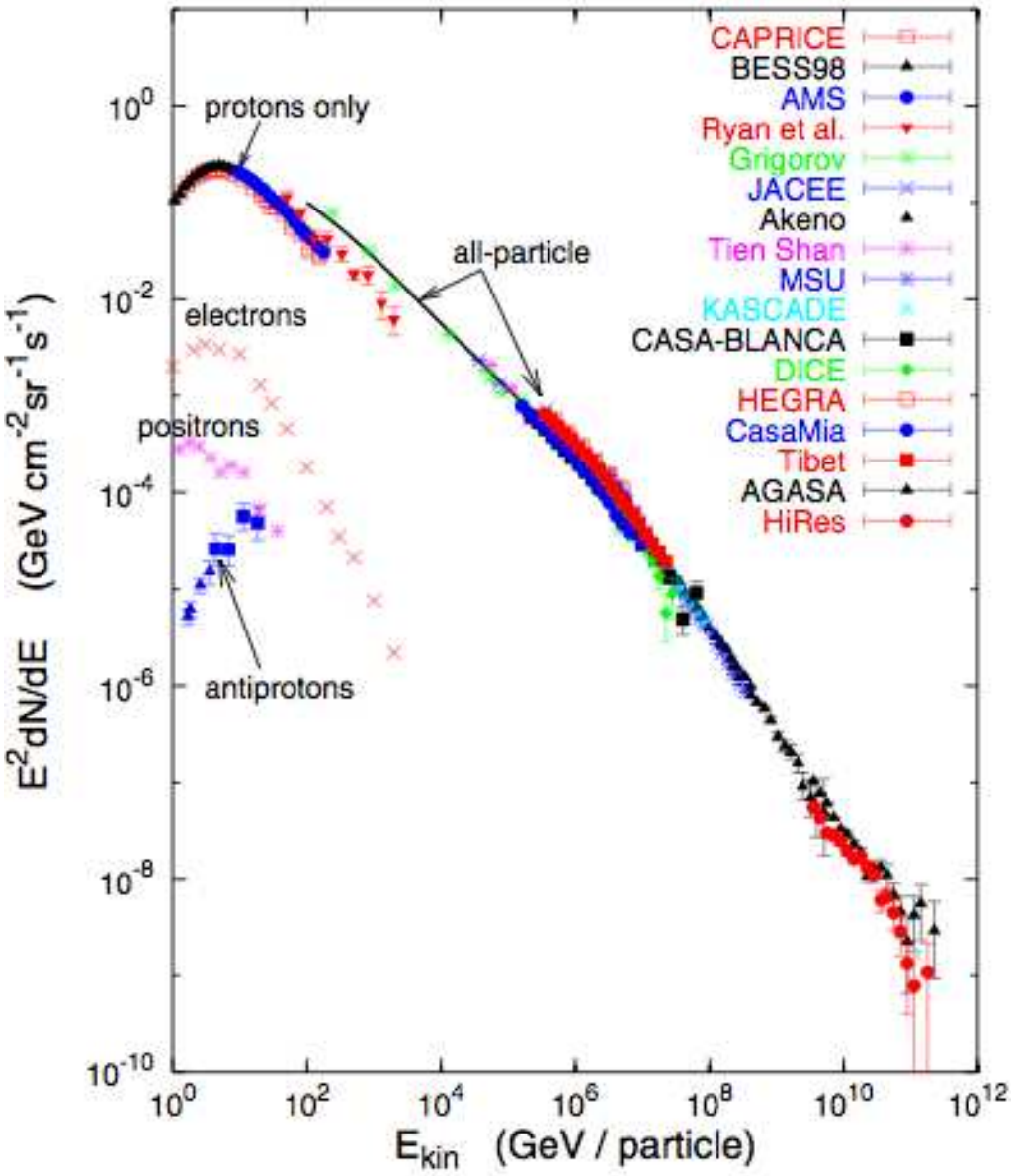

Figure 1.1: Energy spectrum of cosmic rays from (Gaisser & Stanev 2006). The plot shows measurements of protons, electrons, positrons and antiprotons with different experiments from 1 GeV to 10^{12} GeV. Up to few hundred GeV direct measurements are made with magnetic spectrometers above the atmosphere, while up to 10^5 GeV are typically made with calorimeters; above the flux becomes so low that only secondary cascades are measured from large air shower from the ground because of their larger detection area, so that it is possible to perform only indirect and very approximate measurements of the primary composition.

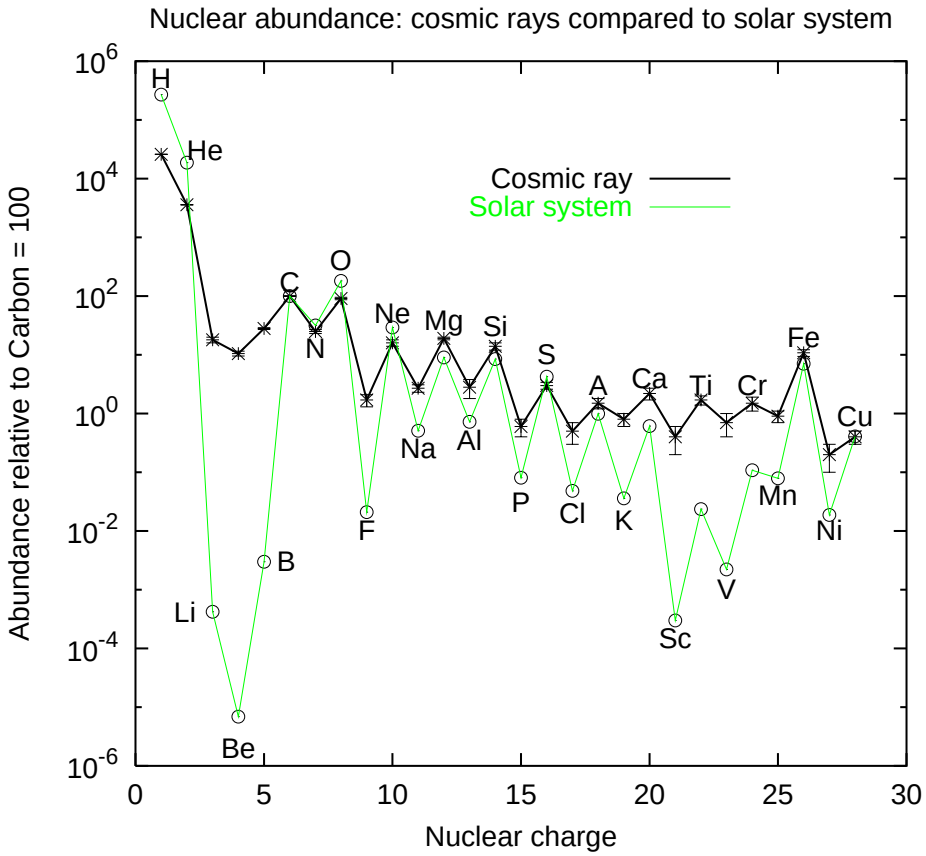

Figure 1.2: Cosmic-ray and solar system nuclear abundances. Figure taken from (Gaisser & Stanev 2006).

(when nuclei are broken up into lighter nuclei when collide with the hydrogen nuclei of the interstellar medium) gives rise to secondary nuclei and isotopes which are rare in nature, antiprotons, and charged pions that decay producing secondary positrons and electrons. Hence, investigation of the abundance like boron-to-carbon ratio give information about the density of matter traversed by the CR particles.

Galactic CR are an important part of the interstellar medium. The energy density of relativistic particles is about 1 eV cm^{-3} and is comparable to the energy density of the interstellar radiation field, magnetic field, and turbulent motions of the interstellar gas. This makes cosmic rays essential for determining the dynamics and processes in the interstellar medium. Most Galactic cosmic rays are probably accelerated in the blast waves of supernova remnants. This theory is supported by the fact that supernova remnants emit synchrotron radiation due to high energy electrons. This could be associated

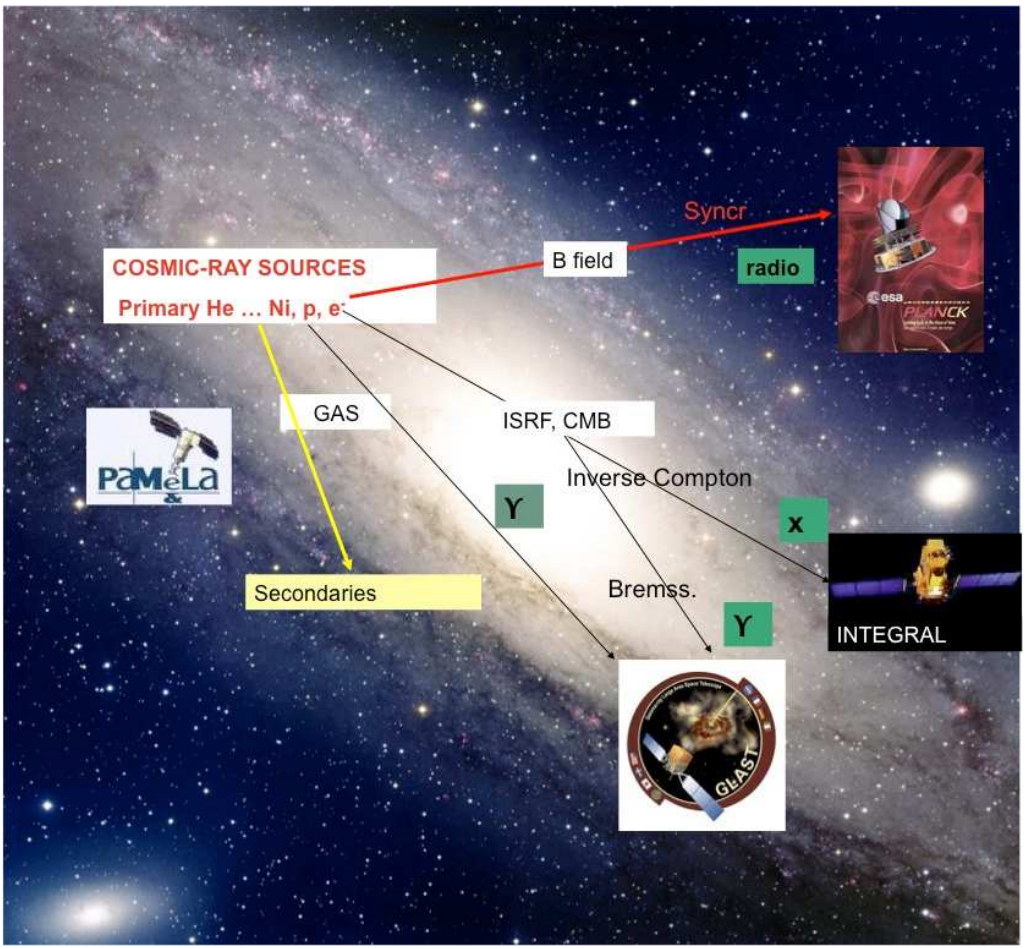

Figure 1.3: Schematic of cosmic-ray propagation in the Galaxy. For details and explanation see text.

with the shock waves in the expanding supernova shell as mechanism of acceleration for electrons and other charged particles. The remnants of the explosions can last for thousands of years, and this is where cosmic rays are accelerated. Particles accelerated near the sources propagate tens of millions years in the interstellar medium where they lose or gain energy. Their initial spectra and composition change, they produce secondary particles and gamma-rays. A schematic picture of CR propagation in the Galaxy is shown in Fig. 1.3.

The 'knee' is associated with the upper limit of of acceleration by Galactic supernovae and the beginning of increasing outflow of particles from the Galaxy. There is a gap between the top end of the low energy component and the bottom end of the extra-galactic component suggesting that an extra component is needed to explain the observed steeping of the spectrum. Hillas (2005) concludes that KASCADE data provide support for a supernova origin of CR and the knee near 3 PeV would be related to emission by the expansion phase of SNRs and the slope would be explained by CR originating in very young type II SNR expanding into dense stellar winds where the interaction generates much stronger magnetic fields, as suggested by Berezhko & Völk (1997).

On the other hand the ankle is associated with the transition from Galactic to an extra-galactic population that is less intense but with a harder spectrum (Peters 1959). and the shape could reflect the transition to dominance of extra-galactic CR.

Both gamma-ray burst and active galactic nuclei are candidates for producing the extra-galactic ultra-high-energy CR.

Recently, with the Pierre Auger Observatory it was demonstrated (The Pierre Auger Collaboration et al. 2007) a correlation between the arrival directions of cosmic rays with energy above 6×10^{19} eV and the nearby extra-galactic sources whose flux has not been substantially reduced by interaction with the cosmic background radiation. Hence, The Pierre Auger Collaboration et al. (2007) demonstrated that AGN or objects having a similar spatial distribution are possible sources of ultra high-energy CR.

1.2 Galactic cosmic-ray propagation

The CR propagation in the Galaxy in a convection-diffusion model is described by the following general equation:

$$\begin{aligned}\frac{\partial\psi(\vec{r},p,t)}{\partial t} &= q(\vec{r},p,t)+\vec{\nabla}\cdot(D_{xx}\vec{\nabla}\psi-\vec{V}\psi)\\ &+ \frac{\partial}{\partial p}p^2D_{pp}\frac{\partial}{\partial p}\frac{1}{p^2}\psi-\frac{\partial}{\partial p}\left[\dot{p}\psi-\frac{p}{3}(\vec{\nabla}\cdot\vec{V})\psi\right]-\frac{1}{\tau_f}\psi-\frac{1}{\tau_r}\psi \quad (1.2)\end{aligned}$$

where, the terms on the right side represent respectively: CR sources (primaries and secondaries), diffusion, convection (galactic wind), diffusive re-acceleration by CR scattering in the interstellar medium, momentum losses (due to ionisation, bremsstrahlung, inverse Compton and synchrotron processes), nuclear fragmentation and radiative decay.
$\psi(\vec{r},p,t)$ is the CR density per unit of total particle momentum p at position $\vec{r}$, $\psi(p)dp = 4\pi p^2 f(\vec{p})dp$ in terms of phase-space density $f(\vec{p})$, $q(\vec{r},p)$ is the source term including primary, spallation and decay contributions, D_{xx} is the spatial diffusion coefficient and is in general a function of $(\vec{r},\beta,p/Z)$ where $\beta = v/c$ and Z is the charge, and p/Z determines the gyro-radius in a given magnetic field. The secondary/primary nuclei ratio is sensitive to the value of the diffusion coefficient and its energy dependence. A larger diffusion coefficient leads to a lower ratio since the primary nuclei escape faster from the Galaxy producing less secondaries. Typical values of the diffusion coefficient found from fitting to CR data are $D_{xx} \sim (3-5)\times 10^{28}$ cm^2 s^{-1} at energy $\sim$1 GeV/n increasing with magnetic rigidity as $D_{xx} \sim R^{1/3}$ where the value of the exponent is typical for a Kolmogorov spectrum (Strong et al. 2007). $\vec{V}$ is the convection velocity, is a function of $\vec{r}$ and depends on the nature of the Galactic wind. Diffusive re-acceleration is described as diffusion in momentum space and is determined by the coefficient D_{pp} related to D_{xx} by $D_{pp}D_{xx} \propto p^2$. $\dot{p} \equiv dp/dt$ is the momentum gain or loss rate.

The term in $\vec{\nabla}\cdot\vec{V}$ represents adiabatic momentum gain or loss in the non-uniform flow of gas. τ_f is the time scale for loss by fragmentation, and depends on the total spallation cross-section and the gas density $n(\vec{r})$ that can be based on surveys of atomic and molecular gas. Elements of the ISM heavier than helium are not important for producing CR by spallation. τ_r is the time scale for radioactive decay (Strong et al. 2007).

CR electron, positron and antiproton propagation constitute just special cases of this equation, differing only in their energy losses and production rates. The boundary conditions depend on the model; usually $\psi = 0$ is assumed at the halo where particles escape into intergalactic space, but this is an approximation.

The transport equation described above is time-dependent; the steady-state solution can be obtained either by setting $\partial\psi/\partial t = 0$ or following the time dependence until a steady state is reached. The time-dependence of q is neglected unless effects of nearby recent sources or the stochastic nature of sources are being studied. Starting with the solution for the heaviest primaries and using this to compute the spallation source for their products, the complete system can be solved including secondaries, tertiaries etc. Then the CR spectra at the solar position can be compared with direct observations, including solar modulation if required (Strong et al. 2007).

The transport equation includes diffusion, convection and re-acceleration.

Diffusion: Due to diffusion energetic charged particles are isotropically distributed and are retained well in the Galaxy. The Galactic magnetic field which tangles the trajectories of particles is very important in this process (Strong et al. 2007). The diffusion of CR results from particle scattering on random magnetohydrodynamic (MHD) waves and discontinuities. The resulting spatial diffusion is anisotropic locally and goes mostly along the magnetic field lines. However, strong fluctuations of the magnetic field on large scales $L \sim 100$ pc, where the strength of the random field is several times higher than the average field strength, lead to the isotropization of global CR diffusion in the Galaxy (Strong et al. 2007).

Convection: The existence of galactic winds in many galaxies suggests that convective transport could be important in CR transport (Strong et al. 2007). In some models the CR propagation is entirely diffusive in a zone $|z| < 1$ kpc, and diffusive-convective outside, while in others such as in GALPROP (see Chapter 4 for details) convection and diffusion are assumed everywhere. CR reaching the convective zone do not return, so it acts as a halo boundary with height varying with energy and Galactocentric radius (Strong et al. 2007).

Re-acceleration: In addition to spatial diffusion, the scattering of CR particles on randomly moving MHD waves leads to stochastic acceleration which is described in the transport equation as diffusion in momentum space with some diffusion coefficient D_{pp}.

The gas content of the Galaxy affects CR propagation for secondary pro-

duction, while the interstellar radiation field and the magnetic field affects it for electron energy losses.
The interstellar radiation field is formed by absorption and re-emission of the stars emission by interstellar dust and extends from the far infrared to the UV. The Galactic magnetic field can be determined from pulsar and extra-galactic source rotation measures and from independent estimates made by simultaneous analysis of radio synchrotron, CR and γ-ray data. For nucleon propagation in the ISM the losses are mainly due to ionisation, Coulomb scattering, fragmentation, and radioactive decay. For electrons the important processes are ionisation, Coulomb scattering, bremsstrahlung in the neutral and ionized medium, as well as Compton and synchrotron losses (Strong et al. 2007).

1.3 Cosmic-ray electron spectrum

Secondary positrons and electrons in CR are the final product of decay of charged pions and kaons which are created in collisions of cosmic-ray particles with gas. Secondary positrons and electrons are usually considered to be a minor component in CR, and this is true in the heliosphere, where the positron to lepton ratio is ≤ 0.1 at all energies. However, the secondary positron flux in the interstellar medium is about half of the total lepton flux at $\approx$1 GeV and secondary electrons around 10% (Strong et al. 2004a). The rapid energy losses of electrons above 100 GeV and the stochastic nature of their sources produces spatial and temporal variations. Supernovae are stochastic events so that they leave their imprint on the distribution of electrons. This leads to large fluctuations in the CR electron density at high energies, so that the electron spectrum measured near the Sun may not be typical (Strong et al. 2004a). Hence, dispersion in the CR injection spectra from SNR may cause the locally observed spectrum to deviate from the average. These effects are much smaller for nucleons since there are essentially no energy losses. In fact, while CR protons and stable nuclei propagate in a large fraction of the Galaxy with small energy losses, electrons of energy E diffuse only for distances $<$ 1 kpc (E/TeV)$^{-1}$ (Kobayashi et al. 2001). Because of the strong electromagnetic losses, electrons diffuse away from the source for a distance that is inversely proportional to their energy. Their average propagation length is l(E) = $2\sqrt{D(E)t}$ with spatial diffusion coefficient with D(10 GeV) = (3-5)$\times 10^{28}$ cm^2 s^{-1} at 1 GeV (Strong et al. 2007). The spectrum of secondary positrons

and electrons depends on the nucleon spectrum and the propagation model. Electrons are affected by large energy losses and the diffusion-loss equation for high energy electrons in Eq.4.18 reduces to the following formula:

$$\frac{\partial\psi(\vec{r},p,t)}{\partial t} = q(\vec{r},p,t) + D_{xx}\vec{\nabla}^2\psi - \frac{\partial}{\partial p}\dot{p}\psi \tag{1.3}$$

where $\dot{p} = dp/dt$ is the loss rate of electrons of momentum p.
To have a better view of the dependence on the momentum losses to the energy, this formulation can be approximated by four terms A, B, C and D such that Longair (1994):

$$-\dot{p} = -\frac{dp}{dt} \propto \; A\; ln\; p + B\; p + C\; p^2 + D\; p^2 \tag{1.4}$$

where
A describes ionisation losses and depends only weakly upon energy and it is proportional to the number density of the hydrogen atoms for the case of atomic hydrogen.
B represents bremsstrahlung losses and adiabatic losses. For the case of fully ionised plasma the bremsstrahlung intensity is proportional to $p\; ln\; p$ and the atomic number, while for neutral atoms it is proportional to the energy of the electron. Adiabatic losses are produced by expansion of the volume within which electrons are contained. This loss is proportional to the energy of the electron.
C describes the loss rate of an ultrarelativistic electron by inverse Compton scattering that is proportional to the p^2 and the energy density of the radiation field.
D describes the synchrotron loss, proportional to p^2 and B^2, the magnetic field.

In order to have an estimate of the origin of the electron spectral index and its dependence on the energy, we can solve the propagation equation for the steady-state and neglecting the diffusion and the position dependence. Suppose that there is a uniform distribution of sources, injecting electrons with spectral index $q(p) = k\; p^{-\alpha}$. The diffusion-loss eq.1.3 becomes (Longair 1994):

$$\psi(p) = \frac{k\; p^{-(\alpha-1)}}{(\alpha-1)\dot{p}} \tag{1.5}$$

Spectra of primary and secondary electrons and positrons are given in Fig. 1.4 as calculated by GALPROP (see for example Strong & Moskalenko (1998)

and Moskalenko & Strong (1998) and a more detailed description of the GALPROP code in Chapter 4). Briefly, this model of CR propagation in the Galaxy reproduces observational data related to cosmic-ray origin and propagation: directly via measurements of nuclei, electrons and positrons, indirectly via gamma rays and synchrotron radiation. They use a diffusive halo model for Galactic cosmic-ray propagation. The code computes the spectra of primary and secondary nucleons, primary electrons, and secondary positrons and electrons. The models are first adjusted to agree with the observed cosmic-ray Boron/Carbon ratio, and the interstellar proton and Helium spectra are then computed; these spectra are used to obtain the source function for the secondary positrons and electrons which are finally propagated with the same model parameters. Fragmentation and energy losses are computed using realistic distributions for the interstellar gas and radiation fields, and diffusive re-acceleration is also incorporated (Moskalenko et al. 2007). In this figure we can see the propagation effects given from eq.1.5.

In fact, at energies below 1 GeV, if ionisation losses dominate, the interstellar spectrum is flatter than the injection spectrum by one power, since $\psi \propto p^{-(\alpha-1)}$. If bremsstrahlung or energy losses dominate, $\psi \propto p^{-(\alpha-1)}$ and there is an intermediate energy range where the spectrum is similar to that at injection. On the contrary at high energies where inverse Compton and synchrotron losses dominate, $\psi \propto p^{-(\alpha+1)}$ and the spectral index steepens. Figure 1.5 illustrates the energy loss time scales, $E(dE/dt)^{-1}$ (Strong & Moskalenko 1998), for electrons and positrons in neutral and ionized hydrogen. The curves are computed for gas densities nH =nH II =0.01 cm^{-3}, and equal energy densities of photons and magnetic field U=UB =1 eV cm-3 (in the Thomson limit). These gas and energy densities characterize the average values seen by cosmic-rays during propagation (Strong & Moskalenko 1998).

Although supernovae are considered to be the main sources of CR in the Galaxy, many questions regarding origin and propagation of cosmic rays are still open. To answer them we have to take into account all available information, both direct measurements of CR and indirect from radio/synchrotron to gamma-ray data and compare them with theoretical models of propagation and interaction in the Galaxy. In fact, most of the information about CR propagation comes from secondary CR measurements, gamma and synchrotron radiation. More information about gamma-ray diffuse emission is given in the next paragraph.

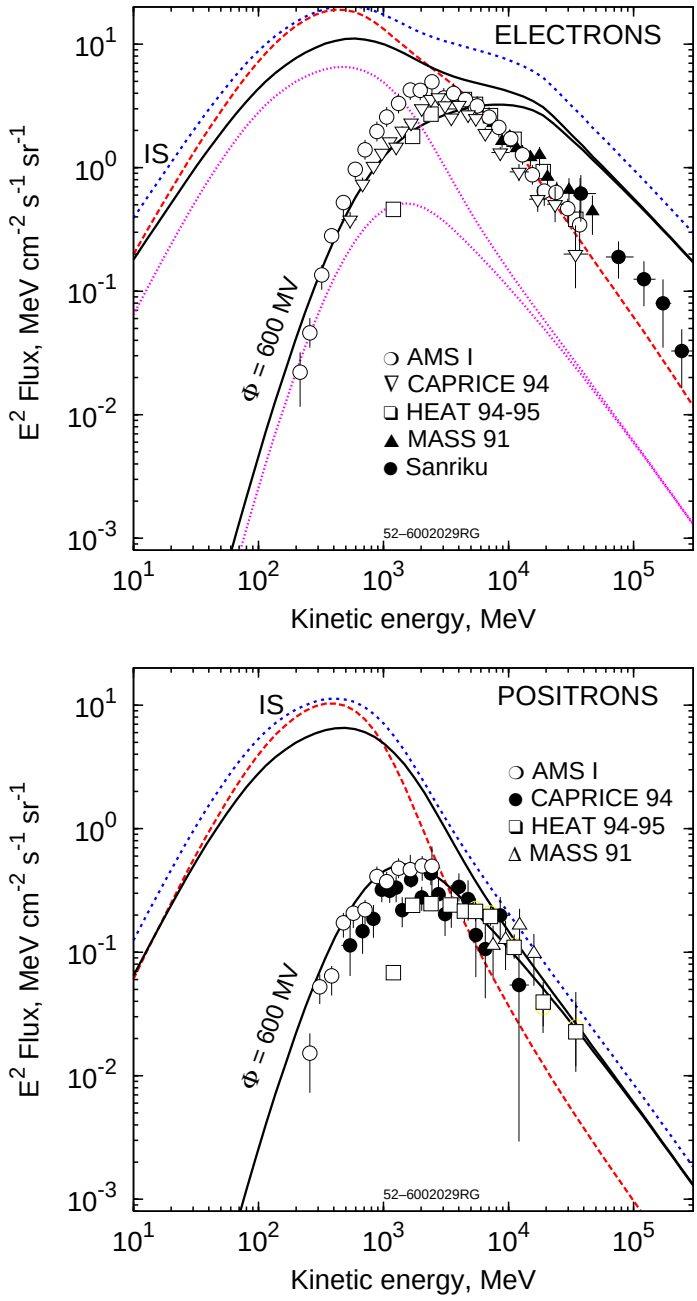

Figure 1.4: Spectra of CR electrons and positrons in the Galactic plane, as predicted by the adopted optimised GALPROP model (Porter et al. 2008). *Top:* Total (primary + secondary) and secondary electrons; *Bottom:* Secondary positrons. Interstellar spectra (IS): $R = 0$ kpc (red long dashes), $R = 4$ kpc (blue short dashes), $R = 8.5$ kpc (black solid), also shown modulated to 600 MV. Secondary electrons are shown separately as magenta lines (IS and modulated) on the left panel at $R = 8.5$ kpc. Data from various experiments: AMS 01 (Alcaraz et al. 2000), HEAT 94-95 (DuVernois 2001), CAPRICE 94 (Boezio et al. 2004) and MASS 91 (Grimani et al. 2002).

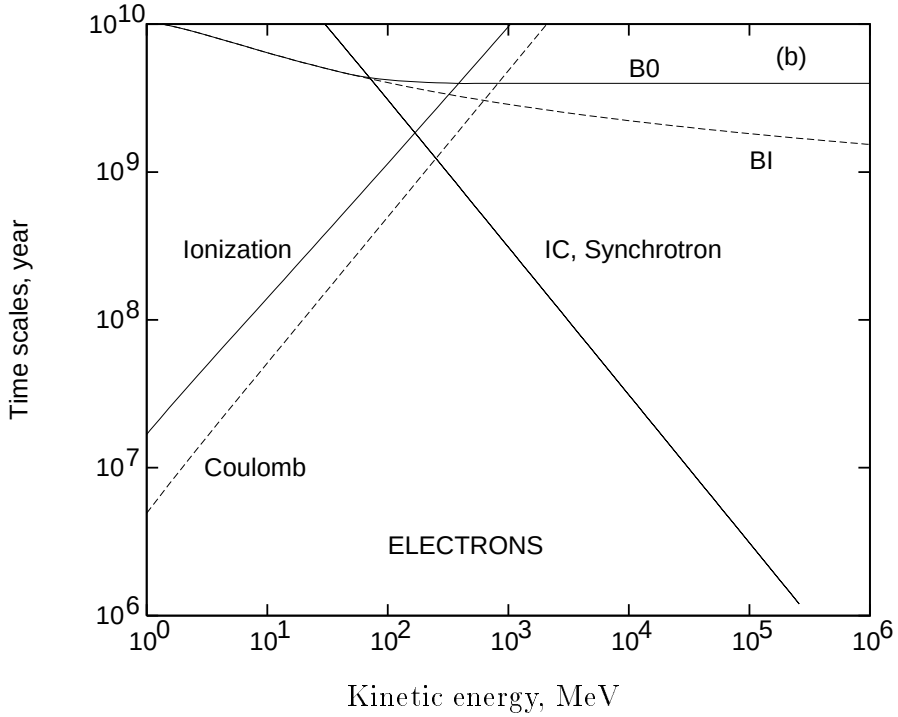

Figure 1.5: Energy loss time-scales of electrons in neutral (solid lines) and ionized (dotted lines) hydrogen (Strong & Moskalenko 1998). The curves are computed for gas densities $n_H = n_{HII} = 0.01$ cm^{-3}, and equal energy densities of photons and magnetic field $U = U_B = 1$ eV cm^{-3} (in the Thomson limit). B stands for bremsstrahlung losses.

1.4 Galactic gamma-ray diffuse emission

The spectrum of the gamma-ray emission produced by Galactic cosmic rays that interact with the interstellar medium and radiation field gives information about the CR propagation in the Galaxy and the source distribution. The gamma-rays have been observed by space observatories such as ESA's COS-B, NASA's Compton Gamma-Ray Observatory, ESA's INTEGRAL, and in the future NASA's GLAST Gamma-Ray Observatory. EGRET and COMPTEL on the Compton Gamma Ray Observatory (CGRO) provided a detailed map of the Galactic gamma-ray sky from 1991 to 2000. Fig (1.6) shows the gamma-ray sky seen by EGRET and the Galactic diffuse component. This is the most direct evidence for CR propagating also in the Galactic halo, well outside of the Galactic disc.

The emission mechanisms that produce gamma rays are 1) the decay of neutral pions generated in collisions between the nuclei of atoms and molecules

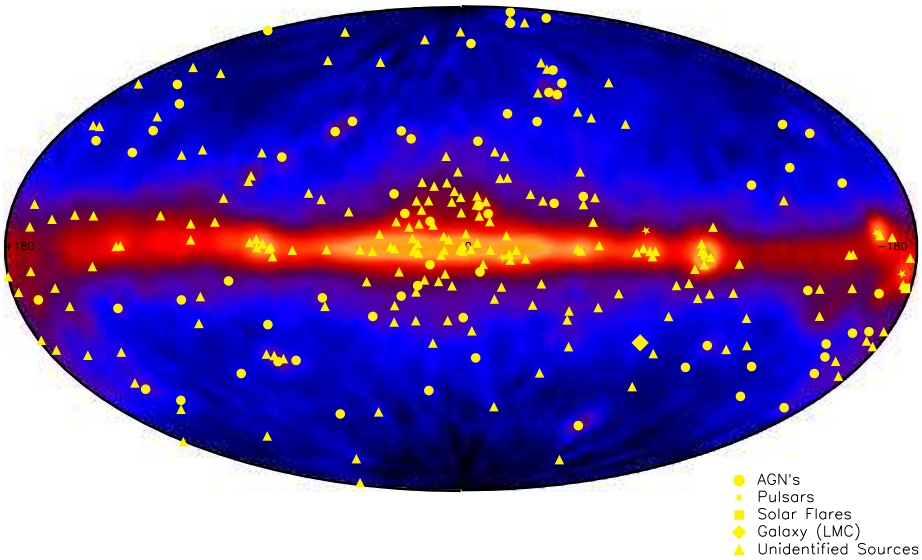

Figure 1.6: Map of the sky in gamma-ray light based on data taken with the EGRET instrument with Energy above 100 MeV. Third EGRET Catalogue sources are plotted as symbols. It is possible to see the Galactic diffuse emission and beyond our galaxy, a much fainter, extragalactic emission can be seen (blue areas in this image). Credit: EGRET Team

of the interstellar gas and CR protons and nuclei; 2) inverse Compton scattering of CR electrons on the interstellar radiation field and 3) bremsstrahlung radiation by CR electrons in the interstellar medium. The neutral pions are created in collisions between CR protons and nuclei of atoms, ions and molecules in the interstellar gas (pp interaction), decaying rapidly into two gamma-rays. In the Inverse Compton process a relativistic electron (CR) scatters a low energy photon of the interstellar radiation field and the CMB so that the photon gains and the electron loses energy. The general result is that the average frequency of scattered photons by ultra-relativistic electrons is $E = 4/3\ \gamma^2 E_0$ where E_0 is the initial photon energy and γ the Lorentz factor. The bremsstrahlung is the radiation associated with the acceleration of electrons in the electrostatic fields of ions and nuclei of atoms.

These processes are dominant in different parts of the spectra of gamma-rays and what we see is the sum of the three independent components (pion decay, IC, bremsstrahlung) which are produced in hadronic and leptonic interactions.

Therefore, the gamma-ray spectrum, if decomposed, can provide information about the large-scale spectra of nucleonic and leptonic components of cos-

Table 1.1: EGRET performance (EGRET web-site)

Energy range	20 MeV - 30 GeV
Effective area	> 1500 cm^2
Angular resolution (on-axis at 100 MeV)	5.8 deg
Angular resolution (on-axis at 10 GeV)	0.5 arcsec
FOV	0.5 sr
Point source sensitivity ($>$100 MeV)	10^{-7}cm^{-2}s^{-1}

mic rays. However, the gamma-ray intensity in certain direction in the sky is the integral along the line of sight where the CR particle spectra, gas density, and interstellar radiation field vary with the position. A proper modelling of the gamma-ray emission including also resolving the different contributions to the diffuse emission, such as from stars and Sun as studied in this work and comparison with gamma-ray data can increase the knowledge of CR and their distribution and propagation.

1.5 Gamma-ray missions cited in this work

In this work I used EGRET (Energetic Gamma-Ray Experiment Telescope) data and INTEGRAL (International Gamma-Ray Astrophysics Laboratory) data, and I made predictions for GLAST, the Gamma Ray Large Area Space Telescope lunched in June 2008. Brief description of these gamma-ray instruments are given below.

1.5.1 EGRET

EGRET (Fig. 1.7), the Energetic Gamma-Ray Experiment Telescope on the Compton Gamma Ray Observatory (CGRO), detected gamma rays in the 20 MeV - 30 GeV range, from 1991 to 2000.

EGRET (see EGRET (web-site)) detected gamma rays using a spark chamber for direction measurement and a NaI(Tl) calorimeter, the Total Absorption Shower Counter (TASC), for energy measurement. The spark chamber had interleaved tantalum foils and tracking layers. A fraction of the incoming gamma rays (about 35% above 200 MeV) interact in the foils to produce high-energy positron-electron pairs, which were tracked through subsequent

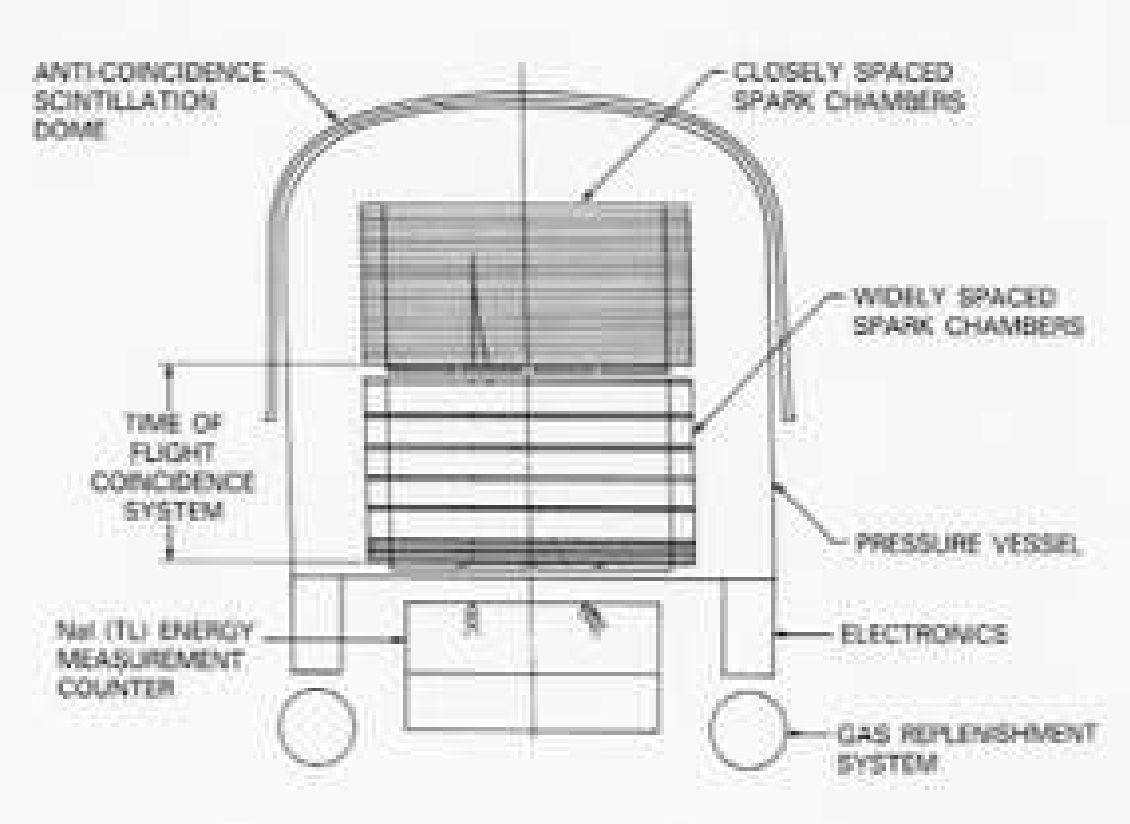

Figure 1.7: Schematic view of the EGRET satellite (EGRET web-site).

layers of the spark chamber and absorbed by the TASC at the bottom of the tracker. Reconstruction of the energies and directions of the positron-electron pairs yielded the energies and directions of the incident photons. Background signals from cosmic rays in the magnetosphere have intensities approximately 10^5 times greater than the celestial gamma-ray emission and therefore EGRET was designed to reject this background very efficiently. The spark chamber was surrounded on the top and sides with a plastic scintillator dome to veto events from charged particles entering from above and the instrument also included a time-of-flight coincidence system to identify down-going events before the spark chamber is triggered. After a trigger, the ions in the spark chamber gas created by the passage of the positron and electron were accelerated by high voltages, creating avalanches of secondary ionizations. The resulting pulses of charge were recorded in the tracking layers for analysis on the ground. Table 1.1 shows the EGRET performance.

1.5.2 INTEGRAL

INTEGRAL (see INTEGRAL (web-site)), ESA's International Gamma-Ray Astrophysics Laboratory, was launched on 17 October 2002 and it's supposed to work at least till 2012. The SPectrometer on Integral, SPI (Fig. 1.8), is dedicated to the fine spectroscopy with angular resolution: 2.5 deg FWHM of celestial gamma-ray sources in the energy range 20 keV to 8 MeV with an energy resolution of 2.2 keV (FWHM) at 1.33 MeV, and a point source sensitivity of $5 \times 10^{-5}\mathrm{cm}^{-2}\mathrm{s}^{-1}$ at 511 keV. SPI uses arrays of opaque and transparent elements arranged in a regular pattern, called coded mask. A hexagonal coded aperture mask is located 1.7 m above the detection plane in order to image large regions of the sky (fully coded field of view = 16 degrees). A point source produces a shadow of the coded mask onto the detector, the shadowgram. From the shadowgram one can obtain the source position using deconvolution algorithms.

1.5.3 GLAST

GLAST, Gamma Ray Large Area Space Telescope (see GLAST (web-site)), launched in early June 2008, consist of the Large Area Telescope (LAT), a pair tracking telescope sensitive to energies from 20 MeV to 300 GeV, and a secondary instrument, the GLAST Burst Monitor (GBM) that will detect gamma ray bursts. In this thesis I will focus on the LAT instrument.
GLAST is in a circular low Earth orbit, at an altitude of 565 km and an inclination of 28.5 degrees. Fig. 1.9 shows a schematic view of the GLAST LAT.

The LAT baseline design for the GLAST TRACKER consists of a four-by-four array of tower modules. Each tower module consists of interleaved planes of silicon-strip detectors and tracker lead converter sheets. Silicon-strip detectors are able to more precisely track the electron or positron produced from the initial gamma-ray than previous types of detectors. SSDs have the ability to determine the location of an object in the sky to within 0.5 to 5 arc minutes. The pair conversion signature is also used to help reject the much larger background of charged cosmic rays. In each module, there are 19 pairs of planes of silicon. In each pair, one plane has the strips oriented in the "x-direction", while the other has the strips oriented in the perpendicular "y-direction". When a particle interacts in the silicon, its position on the plane can therefore be determined in two dimensions. The third dimension of the

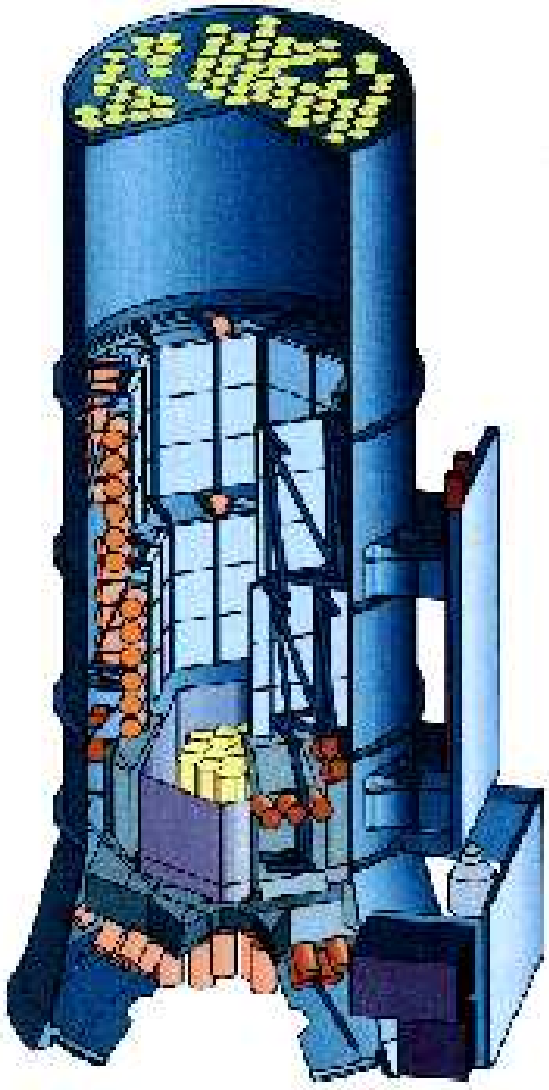

Figure 1.8: Schematic view of the SPI instrument (INTEGRAL web-site).

track is determined by analysing signals from adjacent planes, as the particle travels down through the telescope towards the calorimeter.

The CALORIMETER design for GLAST produces flashes of light that are used to determine how much energy is in each gamma-ray. CsI(Tl) bars, arranged in a segmented manner, give both longitudinal and transverse information about the energy deposition pattern. Once a gamma ray penetrates through the anti-coincidence shield, the silicon-strip tracker and lead calorimeter converter planes, it then passes into the cesium-iodide calorimeters. This causes a scintillation reaction in the cesium-iodide, and the resul-

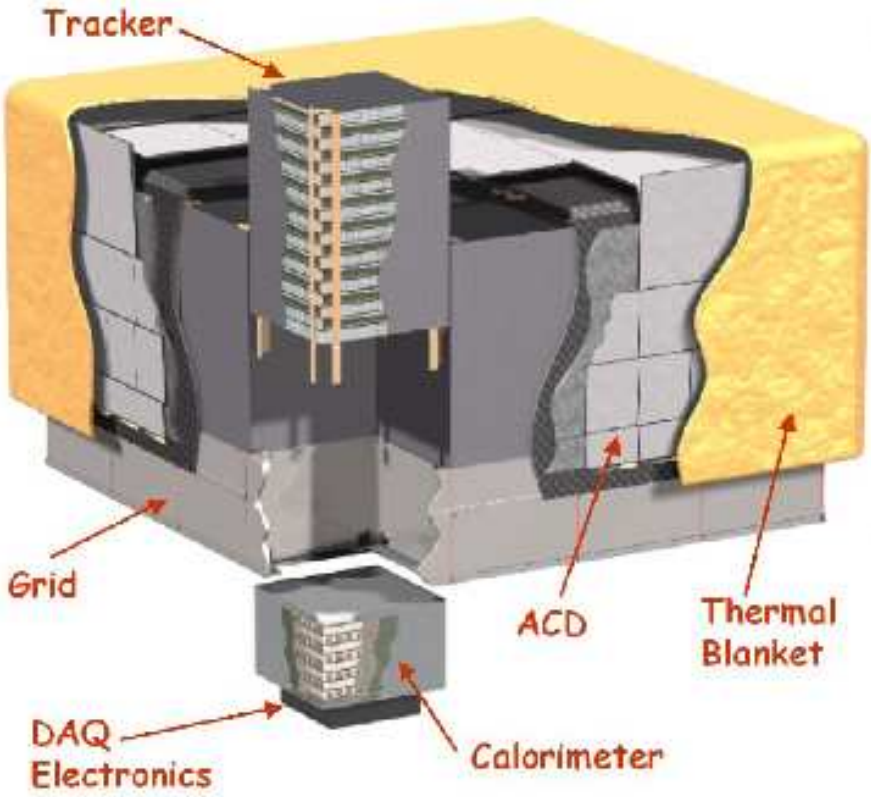

Figure 1.9: Schematic view of the GLAST LAT (GLAST web-site).

tant light flash is photoelectrically converted to a voltage. This voltage is then digitized, recorded and relayed to Earth by the spacecraft's onboard computer and telemetry antenna. Cesium-iodide blocks are arranged in two perpendicular directions, to provide additional positional information about the shower.

The DATA ACQUISITION SYSTEM (DAQ) makes the initial distinction between false signals and real gamma ray signals, and decides which of the signals should be relayed to the ground. This system collects the data from the subsystems, implements the multi-level event trigger, and provides an onboard science analysis platform to search for transients. The DAQ consists of

Table 1.2: GLAST LAT performance

Energy range	20 MeV - 300 GeV
Effective area	> 8000 cm^2
Angular resolution (on-axis at 100 MeV)	3.5 deg
Angular resolution (on-axis at 10 GeV)	0.15 arcsec
FOV	2 sr
Point source sensitivity (>100 MeV)	4×10^{-9}cm^{-2}s^{-1}

specialized electronics and processors that record and analyze the information generated by the silicon-strip detectors and the calorimeter. The DAQ is shielded from the rigors of space-flight, such as extreme high and low temperatures as well as high energy cosmic rays, which can cause the electronics to malfunction.

The ANTICOINCIDENT DETECTOR is the first line of defence against the enormous charged particle background from cosmic ray primary and Earth albedo secondary electrons and nuclei. It consists of segmented plastic scintillator tiles, read out by wave-shifting fibers and photo-multiplier tubes.
Table 1.2 shows the GLAST LAT performance.

The large field of view and good angular resolution of the LAT will improve our understanding of the gamma-ray sky and the higher sensitivity of the GLAST observatory with respect EGRET will allow to discover a large number of undetected sources (GLAST web-site).

1.6 Thesis overview

I start by focussing on developing models of the inverse-Compton gamma rays produced near most luminous stars and OB associations. This emission is clumpy at some level, an effect which could be detectable by GLAST.
In the third Chapter, I develop the model of the same process for the Sun, taking into account the solar modulation of the cosmic-ray electrons and a more precise formalism. The emission is predicted to be extended and also contributes to the diffuse Galactic background. I analyse and detect this extended emission from the Sun in the EGRET data, with a flux in agreement with my estimates. Finally I investigate the diffuse Galactic gamma-ray emission and

the propagation of cosmic-ray electrons in the Galaxy using gamma-ray and radio data, and the GALPROP code. The aim is to exploit gamma-ray emission and synchrotron radiation in order to constrain the cosmic-ray electron spectrum and the Galactic magnetic field.

Chapter 2

Inverse Compton emission from single stars and OB associations: theory and perspectives for GLAST

2.1 Introduction

Inverse Compton (IC) scattering by relativistic cosmic-ray (CR) electrons produces a major component of the diffuse emission from the Galaxy. The photon fields involved are the cosmic microwave background and the interstellar radiation field (ISRF) from stars and dust. Calculations of the inverse Compton distribution have usually assumed a smooth ISRF, but in fact a large part of the Galactic luminosity comes from the most luminous stars, which are rare. Therefore we expect the ISRF, and hence the inverse Compton emission, to be clumpy at some level, which could be detectable by instruments such as GLAST. Even individual nearby luminous stars could be detectable assuming just the normal cosmic-ray electron spectrum. We present the basic formalism required and give possible candidate stars to be detected and make predictions for GLAST. Then we apply the formalism to the OB associations, showing that the IC emission produced is not negligible compared to the sensitivity of current or coming detectors. I include examples of the intensity distribution around stars, and the predicted spectrum of Cygnus OB2.

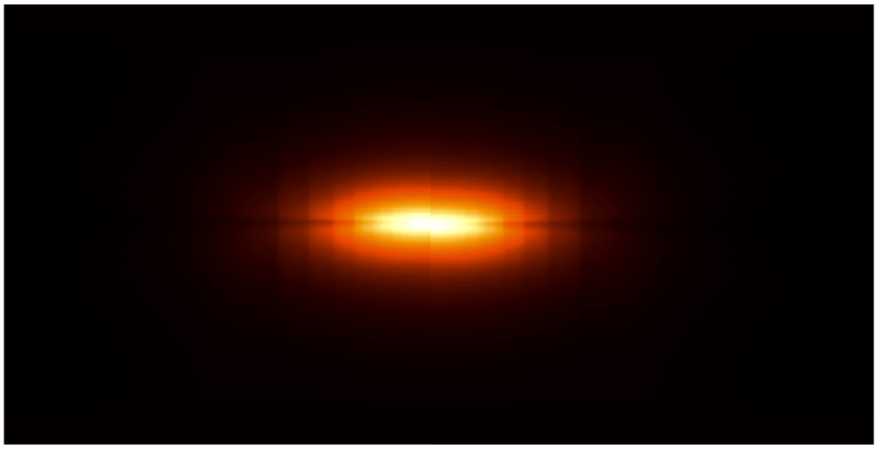

Figure 2.1: Inverse Compton emission from the Galaxy as calculated by GALPROP (Strong et al. 2004a) at 150 MeV in Galactic coordinates with the Galactic center in the middle. Note the assumption of the smoothness, usual for updated galactic models of CR propagation.

2.2 Some rough estimates

In the early 1990s there was already the idea to consider the IC gamma-ray emission generated by electrons accelerated by shocks in winds around hot stars (Chen& White 1991). Models of the inverse Compton distribution, such as in GALPROP (Strong et al. 2004a) have usually assumed a smooth ISRF as shown in Fig 2.1, but a large part of the Galactic luminosity comes from the most luminous stars, which are rare. Thus we expect the ISRF to be clumpy around massive stars. In the present work, already published in Orlando & Strong (2007a) and Orlando & Strong (2007b) we show that even the clumpiness of gamma-ray emission by the ambient cosmic-ray electrons via IC scattering of the stellar radiation field could be detected by GLAST. We begin with the simplest possible rough estimate to show that the IC emission from luminous stars could be visible. The optical luminosity of the Galaxy is about 3×10^{10} $L_\odot$, and a typical O star has 10^5 $L_\odot$ i.e. about 10^{-5} of the Galaxy. Consider such a star at a distance of 100 pc: compared to the entire Galaxy (distance to centre = 8.5 kpc) this inverse Compton source is on average about a factor 100 closer and hence the IC is $10^{-5} \times 100^2$ of the Galactic IC, suggesting it is significant. The IC luminosity L_{IC} within a volume surrounding a star is proportional to the radius r around the star times the optical lumi-

nosity of the star: $L_{IC} \propto r\ L_{STAR}$. The flux depends on the star's distance d: $flux_{IC} \propto L_{IC}/d^2$ and for an angle $\alpha \propto\ r/d$, we obtain $flux_{IC} \propto L_{STAR}\ \alpha/d$. A more precise formulation is given in the next section.

2.3 Inverse Compton from single stars

2.3.1 Basic theory

The gamma ray intensity as a function of the gamma-ray energy of the scattered photon along the line-of-sight s is:

$$I(E_\gamma) = \frac{1}{4\pi} \int \epsilon(E_\gamma)\ ds \tag{2.1}$$

where the emissivity ϵ is given by:

$$\epsilon(E_\gamma) = \int dE_e \int \sigma(\gamma, E_{ph}, E_\gamma) n_{ph}(E_{ph}) c N(E_e) dE_{ph} \tag{2.2}$$

where $N(E_e)$ is the electron spectrum and σ is the Klein-Nishina cross section for isotropic scattering [1]. E_{ph} is the stellar photon energy and n_{ph} the photon density. If the energy of the photon to be scattered is much less than $m_e c^2$, with m_e electron mass, the Thompson cross section can be used to compute the inverse Compton scattering. The average energy of photons scattered by ultrarelativistic electrons is

$$E_\gamma \sim \frac{4}{3}\gamma^2 E_0 \tag{2.3}$$

where E_0 is the energy of the photon field. Using eq. (2.3) and the power-law $N(E_e) = AE_e^{-p}$ for the electron spectrum, where N is the number of electrons per unit energy, the previous formula becomes:

$$\epsilon(E_\gamma) = \frac{A}{2}(\frac{3m_e^2}{4E_0})^{-(p-1)/2} \sigma_\tau n_{ph} c\ E_\gamma^{-(p+1)/2} \tag{2.4}$$

E_0 is the mean value of the photon energy in the case of optical, IR and CMB background and n_{ph} is the mean photon density.

If the electrons are ultrarelativistic, the Thompson approximation is not correct. This is because the center of momentum frame moves with a velocity close to that of the electron and in this frame the energy of the photon is $\gamma h\nu$,

[1] We have also computed the anisotropic case but the difference is less than 10%, see next paragraph.

with $\gamma \gg 1$. When $\gamma h\nu \sim m_e c^2$, the quantum relativistic cross section given by the following Klein-Nishina formula has to be used.

The isotropic IC cross section based on Klein-Nishina cross section is given by (Moskalenko & Strong 2000):

$$\sigma(\gamma, E_{ph}, E_\gamma) = \frac{2\pi r_e^2}{E_{ph}\ \gamma^2}$$
$$\left[2\ q\ ln\ q + (1+2\ q)(1-q) + \frac{(4E_{ph}\gamma\ q)^2}{2\ (1+4E_{ph}\gamma\ q)}(1-q)\right] \tag{2.5}$$

where

$$q = \frac{E_\gamma}{(4E_{ph}\gamma^2(1-\frac{E_\gamma}{\gamma}))}, \quad \frac{1}{4\gamma^2} < q \leq 1 \tag{2.6}$$

E_{ph} is the photon energy, n_{ph} the photon density and γ=E_e/m_e.

Figure 2.3.1 shows the ratio between the inverse Compton intensities generated by Thompson approximation and the Klein Nishina formula for IR, CMB, the optical component and the total. Klein-Nishina starts play an important role above 100 MeV.

We assumed the stellar radiation to have a black body spectrum where the energy density is characterised by the effective temperature following the Stefan-Boltzmann equation. The photon density at distance $r \gg R$ from the star is:

$$n_{ph}(r) = (1/4)\ n_{ph}(R)R^2/r^2 \tag{2.7}$$

since the energy density at r is

$$(\sigma/c)T_{eff}^4(R^2/r^2) = (a/4)\ T_{eff}^4\ (R^2/r^2) \tag{2.8}$$

where R is the radius of the star, $n_{ph}(R)$ is the black body density at the effective temperature and a is the radiation constant. We assumed this relation for all distances. The value of the photon energy density obtained for bright stars (Fig 2.3) is above the mean interstellar value of about 1 eV cm^{-3} even at 10 pc distance from the star, suggesting it contributes to clumpiness in the ISRF and hence in the IC emission. In order to obtain the inverse Compton radiation over a line-of-sight at an angle α from the star, the density variation over the line has to be known. As presented in Fig 2.4, for a given point x on the line-of-sight, the surface photon density is proportional to $1/r^2$, where $r^2 = x^2 + d^2 - 2\ d\ x\ cos\alpha$, with d distance from the star. Integrating the photon density over the line of sight from $x = 0$ to $x = \infty$ the intensity along the line-of sight for a given $\alpha > 0$ is:

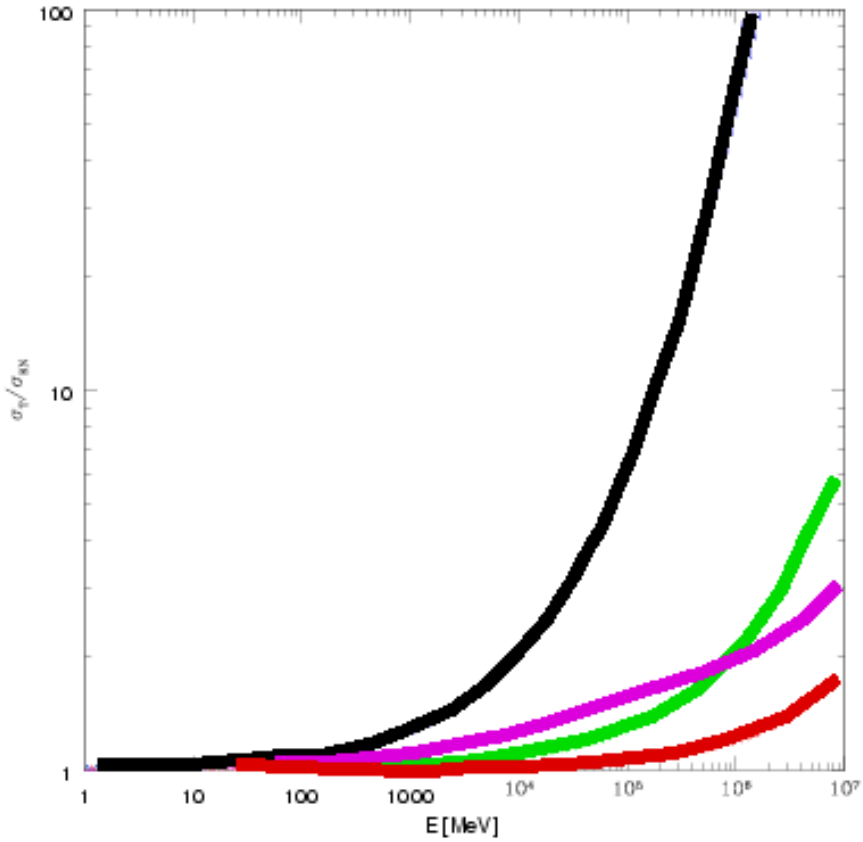

Figure 2.2: Ratio between the inverse Compton intensities generated by Thompson approximation and the Klein Nishina formula. The Green line shows the IR component, the red line the CMB, the pink line the optical and the black line the total. Values of the photon energy are around 1×10^{-6} MeV, 1×10^{-8} MeV and 6×10^{-10} MeV for optical, infrared and CMB components respectively.

$$I(E_\gamma, \alpha) = \frac{1}{4\pi} \int dE_{ph} \times \int \sigma_{KN}(\gamma, E_{ph}, E_\gamma) c\, N(E_e) dE_e \frac{n_{ph}(R)}{4}\, R^2 \times \int_0^\infty \frac{dx}{x^2 + d^2 - 2\, x\, d\, cos\alpha} = \frac{R^2}{16\, \pi\, d\, sin\alpha} [\pi/2 + arctan(cot\, \alpha)] \times \int dE_{ph} \int \sigma_{K-N} c\, N(E_e) dE_e n_{ph}(R) \quad (2.9)$$

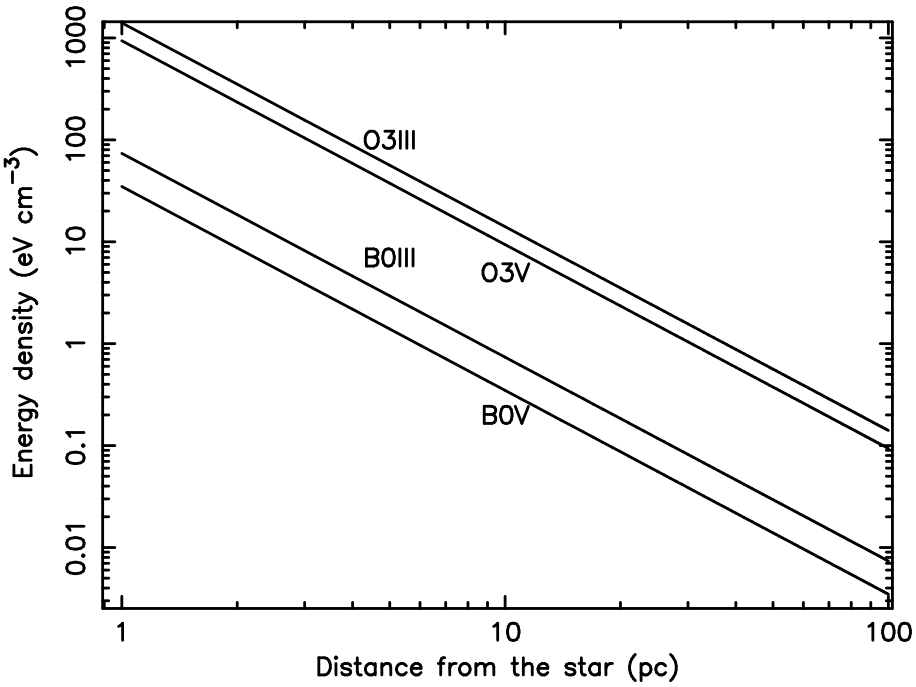

Figure 2.3: Photon energy density around different main sequence and giant stars from 1 pc to 100 pc.

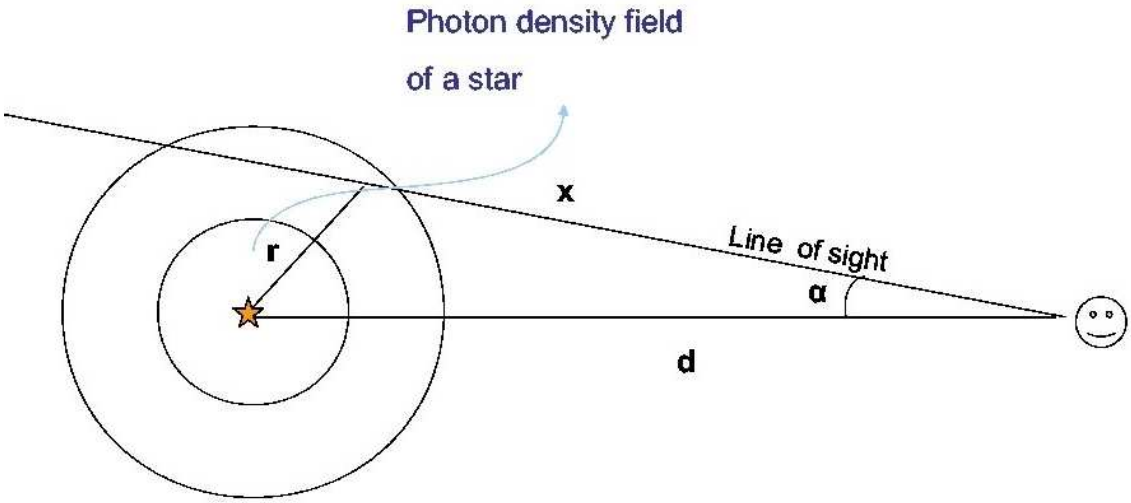

Figure 2.4: Definition of variables for eq (3).

After integrating the intensity over the solid angle, the total photon flux produced by inverse Compton becomes:

$$f(E_\gamma) = \int_0^{2\pi} d\varphi \int_0^{\alpha} I(E_\gamma, \alpha)\, sin\alpha\, d\alpha =$$
$$= \frac{R^2}{16d}(\pi\alpha + (\frac{\pi}{2})^2 - arctan^2(cot\alpha))$$

$$\times \int dE_{ph} \int \sigma_{KN}\ c\ N(E_e)\ n_{ph}(R)\ dE_e \tag{2.10}$$

which for small α is proportional to α/d and the intensity I (per solid angle) is proportional to 1/(αd).

2.3.2 Comparison of isotropic/anisotropic formulations

In Orlando & Strong (2007a) the isotropic formulation for the Klein-Nishina cross section given in Moskalenko & Strong (2000) was used in the analytical formulation for estimating the IC gamma-ray emission. The anisotropic formulation is given by:

$$\frac{d\sigma_{KN}}{d\Omega} = \frac{{r_e}^2}{2}(\frac{E'_\gamma}{E'_{ph}})^2[\frac{E'_\gamma}{E'_{ph}} + \frac{E'_{ph}}{E'_\gamma} - \sin^2\eta']$$

with E'_{ph} target photon energy in electron system, E'_γ gamma-ray energy in electron system and ζ = π -η = scatter angle of photon in lab. r_e is the classical electron radius, E'_{ph} and E'_γ are electron reference system (ERS) energies of the incoming and scattered photons, respectively, and η' is the scattering angle in the ERS.

$$E'_\gamma = \frac{E'_{ph}}{1 + \frac{E'_{ph}}{m_e}(1 - \cos\eta')}$$

$$d\Omega = 2\pi \sin\eta' d\eta' = 2\pi d\cos\eta'$$

After some calculations the resulting anisotropic cross section used in Orlando & Strong (2008) is:

$$\sigma_{KN}(\gamma, E_{ph}, E_\gamma) = \frac{\pi r_e^2 m_e^2}{E_{ph} E_e^2} \times$$
$$\left[\left(\frac{m_e}{E'_{ph}}\right)^2 (\frac{v}{1-v})^2 - 2\frac{m_e}{E'_{ph}}\frac{v}{(1-v)} + (1-v) + \frac{1}{1-v}\right] \tag{2.11}$$

where $v = E_\gamma/E_e$.

$$E'_{ph} = \gamma E_{ph}(1 - cos\ \eta) \tag{2.12}$$

where η is the scattering angle for the relativistic case, with $\eta = \pi$ for a head-on collision. Figure (2.5) shows the isotropic and anisotropic Klein-Nishina cross-sections as a function of the scattering angle.

In Fig.(2.6) is shown the contribution to the flux as a function of distance along the line-of-sight for the isotropic and anisotropic cross-sections.

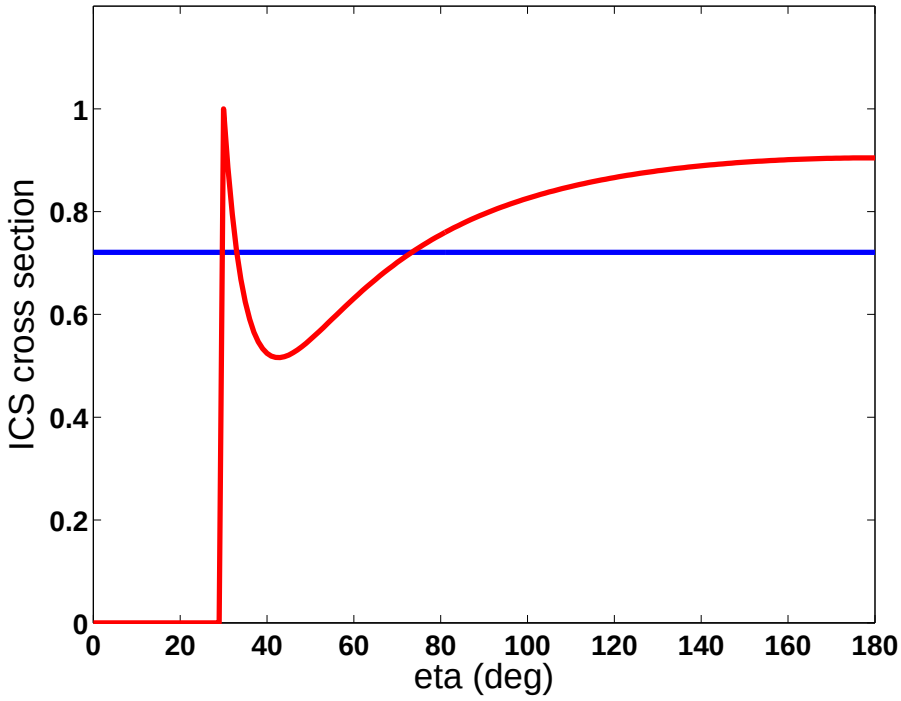

Figure 2.5: Isotropic (blue line) and anisotropic (pink line) Klein-Nishina cross-sections as a function of the scattering angle normalised to 1.

2.4 IC for stellar types and distances

The IC emission for stars has been computed using the electron spectrum shown in Fig. 2.7.
The electron spectrum is calculated by GALPROP developed by Strong and Moskalenko (see Strong & Moskalenko (1998)). This model of CR propagation in the Galaxy reproduces observational data related to cosmic-ray origin and propagation: directly via measurements of nuclei, electrons and positrons, indirectly via gamma rays and synchrotron radiation.

The spectrum used, shown in Fig. 2.7 in red, approximates the local interstellar electron spectrum based on direct measurements. Explaining the diffuse Galactic emission including the 'GeV excess' requires about a factor 4 higher electron spectrum described by the optimized model (Strong et al. 2004b).

The gamma-ray flux depends on the star distance and on the angle from the star: in fact, integrated up to some angle, it scales as the linear inverse of the distance and to first approximation is proportional to the angular distance from the star. Fig 2.8 shows, as an example, the spectrum of the gamma-ray

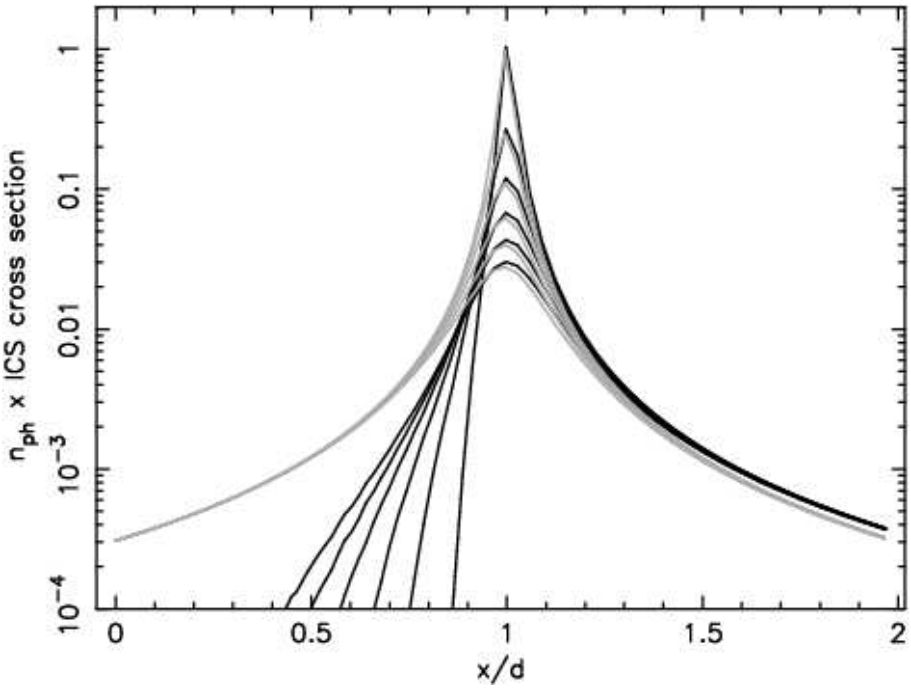

Figure 2.6: Relative contribution (arbitrary units) of the isotropic (grey lines) and anisotropic (black lines) cross sections, multiplied by the photon density along the line of sight for E_e=10^4 MeV and E_γ=100 MeV. x and d are defined in Fig 1. The lines represent different angles from the Sun, from 1° to 6° (right to left).

.

emission of stars of different spectral types and Fig 2.9 the gamma-ray flux as function of the angle of integration [2].

2.5 Candidates for detection and predictions for GLAST

The most luminous and nearby stars are candidates for giving a significant flux contributing to the total Galactic emission. Since the IC sources are extended, the angular radius to which the flux is taken is arbitrary, but we choose a value of 5° which is a compromise between angular resolution and sensitivity of gamma-ray telescopes. The value of this angle could be further optimized for specific cases.

[2]Note that the main contribution to the emission comes from more than about a pc from the star and hence is mostly beyond the influence of stellar winds (Torres et al. 2004).

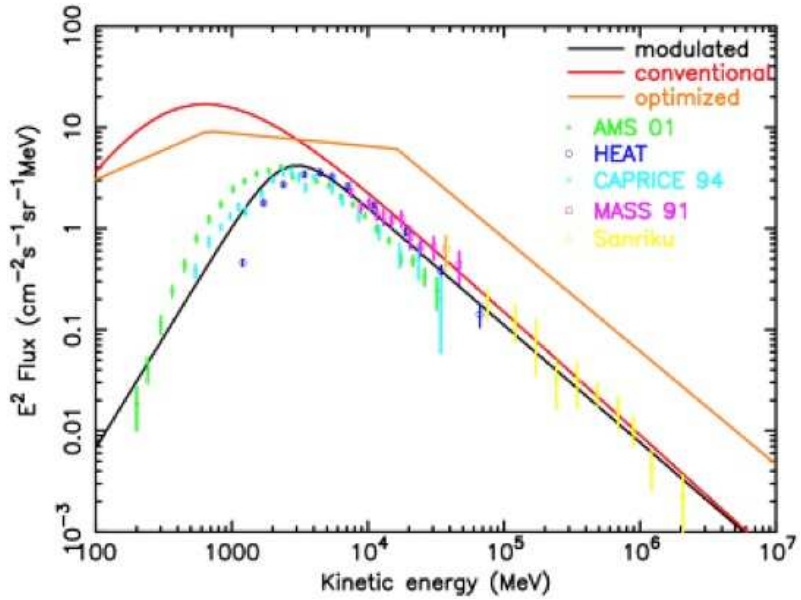

Figure 2.7: Solar modulated electron spectrum (black line), adopted interstellar model (red line) and optimized model (yellow line) compared with selected data. Data: AMS 01 (Alcaraz et al. 2000), HEAT 94-95 (DuVernois 2001), CAPRICE 94 (Boezio et al. 2004), MASS 91 (Grimani et al. 2002) and Sanriku (Kobayashi 1999)

2.5.1 Possible stellar candidates

In order to simulate the gamma-ray flux from halos around stars, the possible candidates have been taken from the Hipparcos nearby star catalogue (Hipparcos catalog and Tycho Catalogues 1997), choosing only the first 70 most luminous stars. This list includes stars up to 600 pc distance. The results are compared in Fig 2.10 with the GLAST point source sensitivity (GLAST web-site) above 100 MeV of about 3×10^{-9}cm^{-2}s^{-1} for one year observation and about 1.5×10^{-9}cm^{-2}s^{-1} for 5 years observation. Up to now the sensitivity of GLAST for extended sources is not known, depending strongly on the knowledge of the background that varies over the sky. Hence the point source sensitivity used here is an optimistic assumption for the estimate of the detectability. However the exact knowledge of the model give a much higher possibility of detection.

According to our prediction, the most gamma-ray bright stars are κ Ori (B0Iab, distance 221 pc), ζ Pup (O5Ia, distance 429 pc, parameters from Lamers & Leitherer (1993)) and ζ Ori (O9.5Ib, distance 250 pc) with a flux respectively of 1.2, 1.1 and 1×10^{-9}cm^{-2}s^{-1} for energy$>$ 100 MeV and within

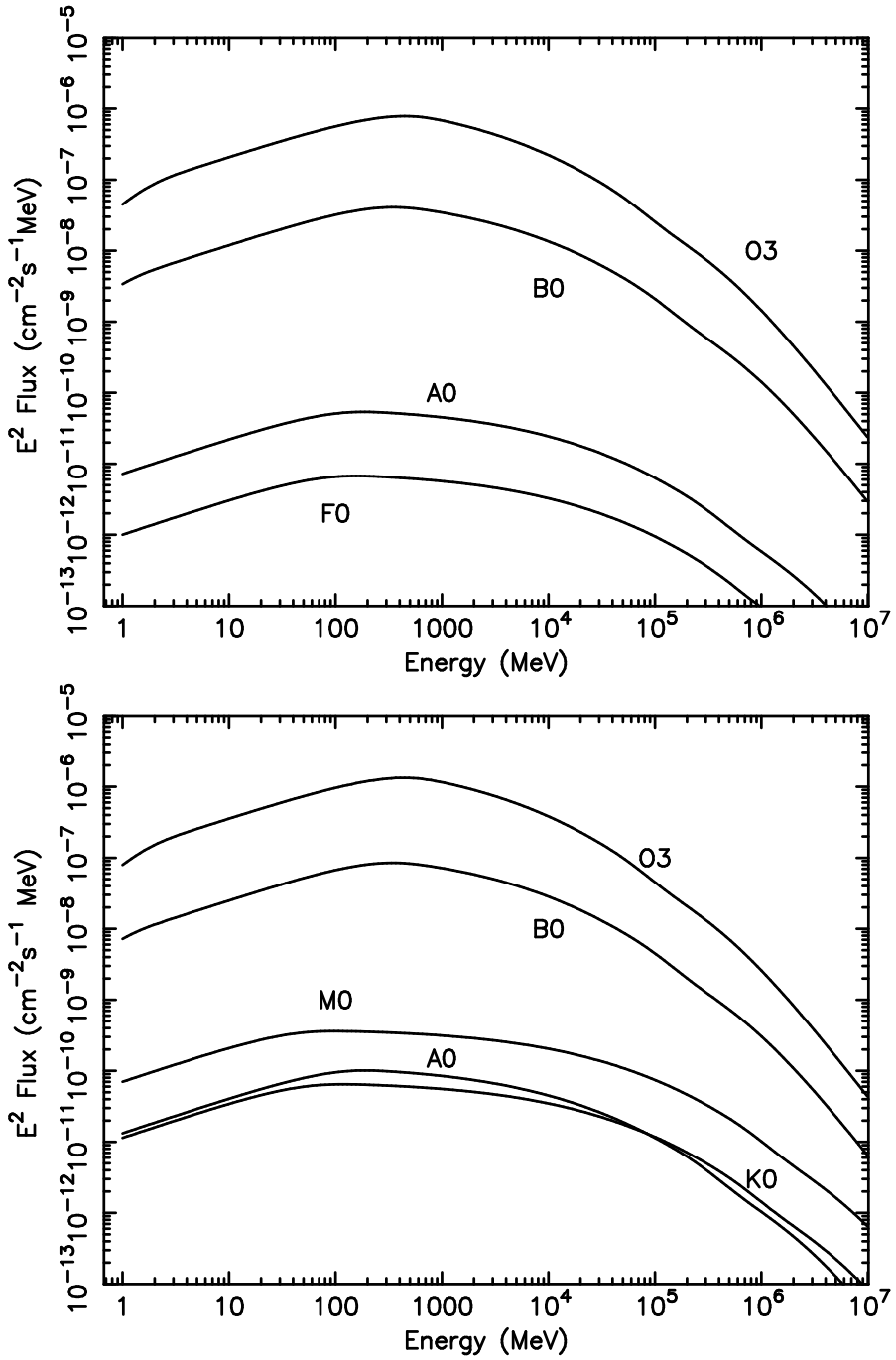

Figure 2.8: Gamma-ray spectrum generated by IC scattering on the photon field of main sequence stars (upper) and giant stars (lower) at 100 pc distance. Flux is integrated over 5° radius.

.

5° angle. Further stars with a flux above 10^{-10} cm^{-2}s^{-1} are Betelgeuse, δ Ori, β Ori or Rigel, ζ Per, λ Ori, ϵ cMa. Another important candidate is η Carinae

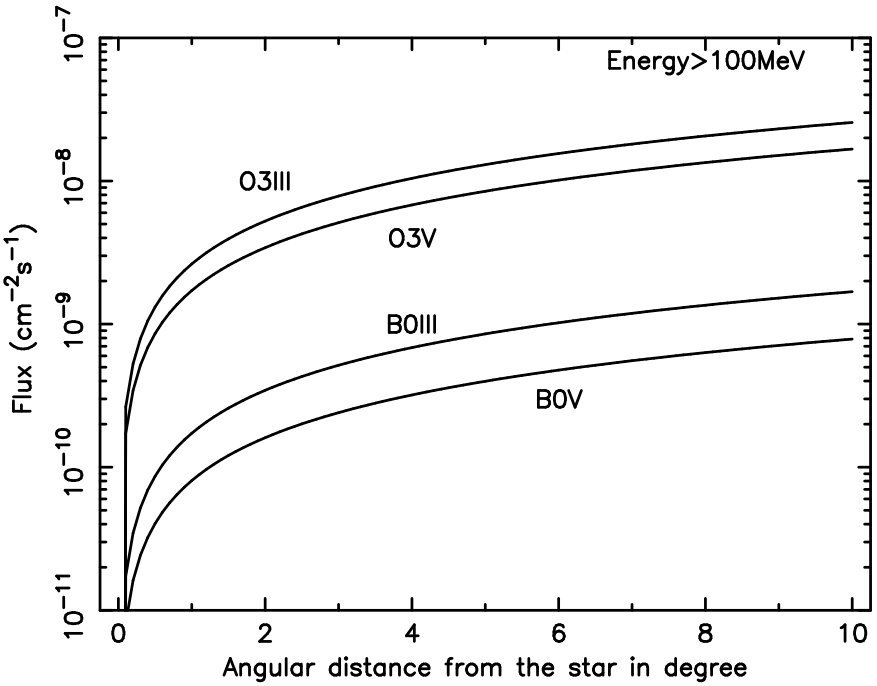

Figure 2.9: Cumulative flux integrated over solid angle from stars at 100 pc distance as a function of angle for $E_\gamma > 100$ MeV.

with T_E = 30000 K, 2.3 kpc distance and luminosity of 7×10^6 solar luminosity (Davidson & Humphereys 1997). The estimated IC flux within 5° angle is 2.2, 0.1, 0.005 $\times 10^{-9}$ cm^{-2}s^{-1} respectively for energy $>$ 100 MeV, $>$ 1 GeV and $>$ 10 GeV. The fluxes obtained are affected by errors due to the big uncertainty of the parameters of the stars which could mean that some can be brighter γ-ray sources than these estimates and hence more likely to be detected.

Figure 2.11 shows the inverse Compton intensity profile of zeta Ori from 200 stellar radii to 30 pc distance from the star compared with the intensity of the average inverse Compton emission as calculated with GALPROP in the region around the star. Both emission from the single star and total IC emission from the interstellar radiation field along the line-of-sight are plotted for three energy ranges: 100-150 MeV, 500-1000 MeV and 1000-2000 MeV. We can see here an example of the contribution of a single O star to the total IC emission as a function of the distance from the star.

Figure 2.12 shows, as an example, the intensity distribution of zeta Ori (l = 290 and b = -30) above 100 MeV with two different estimates of the distance. Along the line of sight, the minimum distance from the star is taken as 2 pc, to avoid the modulation of the electron spectrum due to stellar winds. This also means that the IC emission could be greater than we estimate, due to

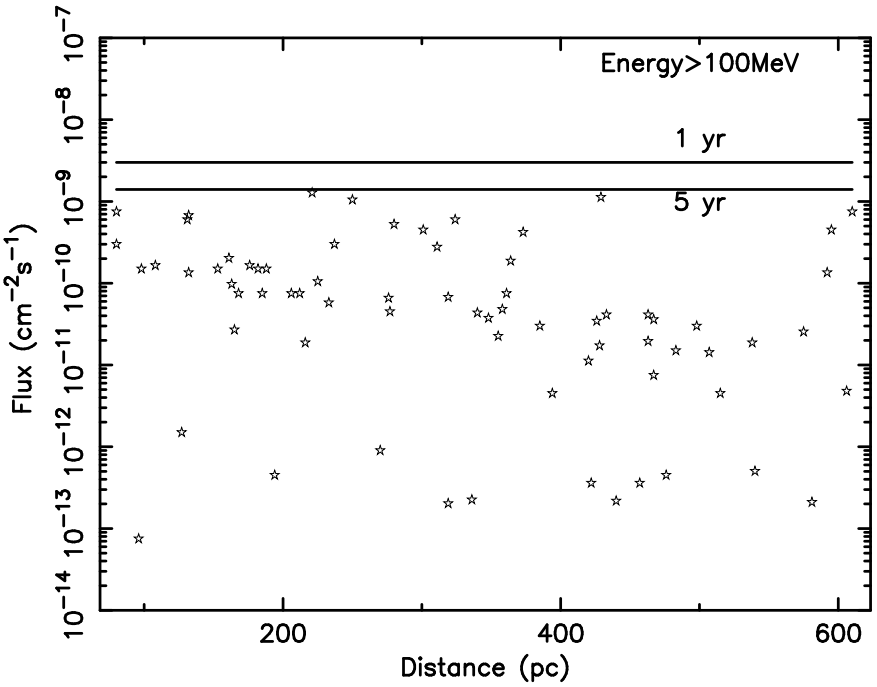

Figure 2.10: Gamma flux integrated over 5° angle from the 70 most luminous stars from Hipparcos catalogue up to 600 pc distance for $E_\gamma > 100$ MeV compared with the GLAST point source sensitivity for 1 year and 5 years observation (horizontal lines)

electrons accelerated in stellar winds. In the Hipparcos Catalogue (Hipparcos catalog and Tycho Catalogues 1997) the parallax of zeta Ori is 3.99 mas corresponding to 250 pc distance, while in Fullerton et al. (2006) the distance is 400 pc. The estimates obtained are affected by the big uncertainty of the parameters of the stars, which could mean that some might be brighter gamma ray sources than these estimates.

Table 2.1 is a list of Galactic O stars with a flux above few 10^{-10} cm^{-2} s^{-1} above 100 MeV and for 5°. All are below the GLAST sensitivity. Stellar parameters are taken from Fullerton et al. (2006). They take some of them from the literature (es. Lamers & Leitherer (1993) or Scuderi et al. (1998)), and revised some parameters which estimates are determined from stellar winds profiles fitted with mass-loss rates determined from radio and H_α emission Fullerton et al. (2006) .

Table 2.1: List of Galactic O stars with a flux above between few 10^{-10} cm^{-2} s^{-1} and 10^{-9} cm^{-2} s^{-1}, below the GLAST sensitivity for one year of 4×10^{-9} cm^{-2} s^{-1}. Stellar parameters are taken from Fullerton et al. (2006).

Star	Spectral type	Distance (kpc)	T_{eff} (kK)	R/R_0
14947	O5 If+	2	37.5	16.8
15558	O5 III(f)	2.2	41.0	18.2
24912	O7.5 III(n)((f))	0.4	35.0	14.0
30614	O9.5 Ia	1.2	29.0	32.5
36861A	O8 III((f))	0.7	33.6	15.1
37043A	O9 III	0.6	31.4	21.6
47839	O7 V((f))	0.7	37.5	9.9
66811	O4 I(n)f	0.5	39.0	19.4
93129A	O2 If*	3.5	42.5	22.5
149757	O9.5 Vnn	0.2	32.0	8.9
190429A	O4 If+	2.2	39.2	20.8
190864	O6.5 III(f)	2.3	37.0	12.3
192639	O7 Ib(f)	1.3	35.0	18.7
210809	O9 Iab	0.9	31.5	21.2
36486A	O9.5 II	0.4	30.6	17.7
37742	O9.7 Ib	0.4	30.5	22.1
46150	O5 V((f))	1.5	40.9	11.2
46223	O4 V((f+))	1.5	42.9	12.4
57061	O9 II	0.9	30.6	17.7
149038	O9.7 Iab	1	30.5	22.1
149404	O9 Ia	0.9	31.4	21.8
151804	O8 Iaf	1.2	33.2	21.1
152408	O8: Iafpe	1.4	33.2	21.1
152424	OC9.7 Ia	1.4	30.5	22.1
164794	O4 V((f))	1.6	42.9	12.4

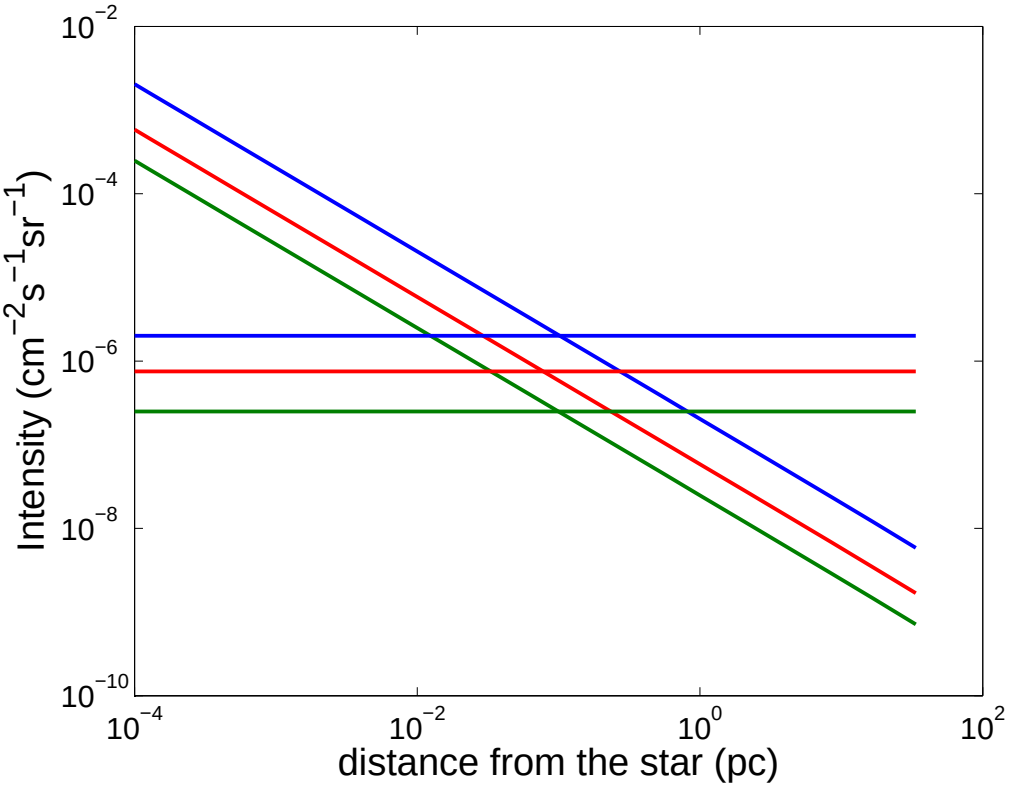

Figure 2.11: Expected profile of zeta Ori (l = 290 and b = -30) from 200 stellar radii to 30 pc distance from the star compared with the intensity of the average inverse Compton emission (horizontal lines) as calculated with GALPROP in the region around the star for three energy ranges: 100-150 MeV (blue lines), 500-1000 MeV (red lines) and 1000-2000 MeV (green lines). Distance around 10^{-4} pc corresponds to 3×10^{-5} deg, 10^{-1} pc to 0.03 deg, 1 pc to 0.2 deg, 10 pc to 2.5 deg and 30 pc to 7 deg.

2.5.2 OB associations: Cygnus OB2

Apart from individual stars, the full stellar population will exhibit features due to their clustering e.g. in OB associations. As an example, Fig. 2.13 shows the spectrum of Cygnus OB2 centred on the cluster. 120 O stars and 2489 B stars and 6000 F stars have been distributed in a region of 2° diameter (60 pc) at 1.7 kpc distance. Data for the Cygnus association and the number of stellar components are taken from Knödlseder et al. (2000). Using 2MASS infrared observations in the J, H, and K bands, Knödlseder et al. (2000) determined the morphology and stellar content of the Cygnus OB2 association. Their study demonstrated a spherically symmetric association of 2 deg in diameter with a

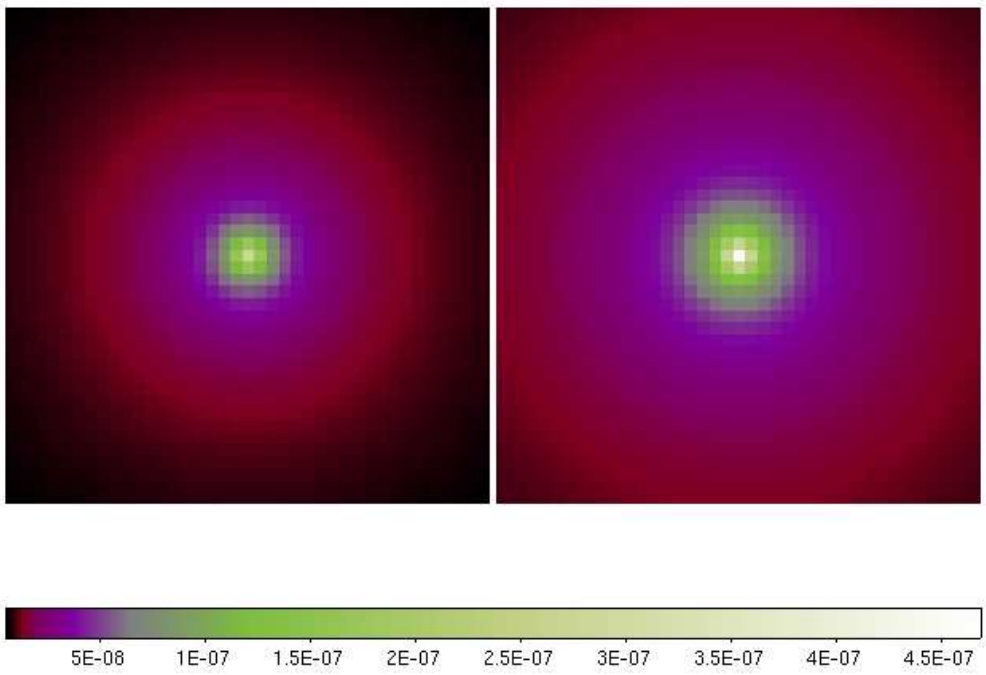

Figure 2.12: Expected profile of zeta Ori (T_E =30500 K, Radius = 22.1 R_{SUN}) above 100 MeV. On the left the distance is 400 pc taken from Fullerton et al. (2006) on the right the distance is 250 pc Hipparcos catalog and Tycho Catalogues (1997). The scale shows the intensity (cm^{-2} s^{-1} sr^{-1}) above 100 MeV. The region shown is 20 deg wide.

half light radius of 13' at an assumed distance of 1.7 kpc.

For my simulation the stars have been supposed to be O5V with T_E = 42000 K and R = 12 R_{SUN}, B5V with T_E = 15200 K and R = 3.9 R_{SUN} and F5V with T_E = 8180 K and R = 1.7 R_{SUN}. The estimated IC emission is comparable to the total IC emission from the Cygnus region and the extragalactic background Strong et al. (2004b). The emission extends to more than of 1° radius, due to the size and the extension of the IC emission. The IC flux calculated from our model within 5° is 18, 1.9, 0.05 $\times$ 10^{-9} $cm^{-2}s^{-1}$ respectively for energy $>$100 MeV, $>$1 GeV and $>$10 GeV, while within 1° is 3.7, 0.3 and 0.008 $\times$ 10^{-9} $cm^{-2}s^{-1}$ for the previous energy ranges. This will clearly be of interest for GLAST. Furthermore we note that cosmic rays may also be accelerated in colliding winds in OB associations (eg. Reimer (2007) and Torres (2006)) which would further increase the fluxes.

2.6 Discussion and perspectives for GLAST

We have estimated the gamma-ray emission by IC scattering of cosmic-ray electrons with the radiation field around stars. We find that the contribution of the most luminous stars is non-negligible and even individual luminous stars could be detectable by GLAST. Moreover OB associations can contribute to the clumpiness of the emission. A model of the Cygnus OB2 association has been computed, showing that the estimated IC emission is comparable to the total diffuse IC emission from the Cygnus region and the extragalactic background.

Moreover, O, B, and WR massive stars lose a significant fraction of their masses in their winds. Hence, the winds of a association of massive stars may be a target for cosmic rays (e.g., Torres et al. (2004), although only high energy photons might be detected, because of the wind modulation of the cosmic-ray flux. This scenario may explain sources of the new of ground-based Cherenkov telescopes, like MAGIC or HESS (Torres 2006). In view of the several unidentified sources already detected by HESS in the hundred of GeV - TeV energy range (Aharonian et al. 2005), a comprehensive study of regions of star formation in the Galaxy is promising in the future and for the GLAST data. In addition open clusters are concentrations of young stars surrounded by high density clouds. They contain many early-type stars (OB and Wolf-Rayet type) which produce strong radiation fields and winds (Bednarek 2007). Some open clusters are found in the error boxes of the EGRET catalogue, e.g. 3EG J2021+4716 and 3EG J2016+3657 Berk 87, 3EG J2033+4118 Cyg OB2, or 3EG J1027-5817 Westerlund 2. TeV sources have been also reported inside the Cyg OB2 by the HEGRA group (Aharonian et al. 2002), Westerlund 2 by the HESS group (Aharonian et al. 2006) and Berk 87 by the Milagro group (Abdo et al. 2007). Bednarek (2007) calculates the expected broad-band photon emission from the open cluster Berkeley 87 and its surroundings. He considered the radiation processes due to both electrons and hadrons accelerated inside the open cluster. He applied the acceleration process at the shocks arising in the winds of Wolf-Rayet (WR) type stars. Particles diffuse through the medium and interact with the matter and radiation, at first inside the open cluster and, later in the dense surrounding clouds. In future a detailed study of these sources and models of these mechanism of emission have to be implemented.

With GLAST it will be important to search for gamma-ray excesses at the positions of OB associations and evaluate the positional coincidences with multi-wavelength observations and comparison with theoretical models. For cases of no detection or not significant detection, the upper limits can be used to constrain the theoretical models.

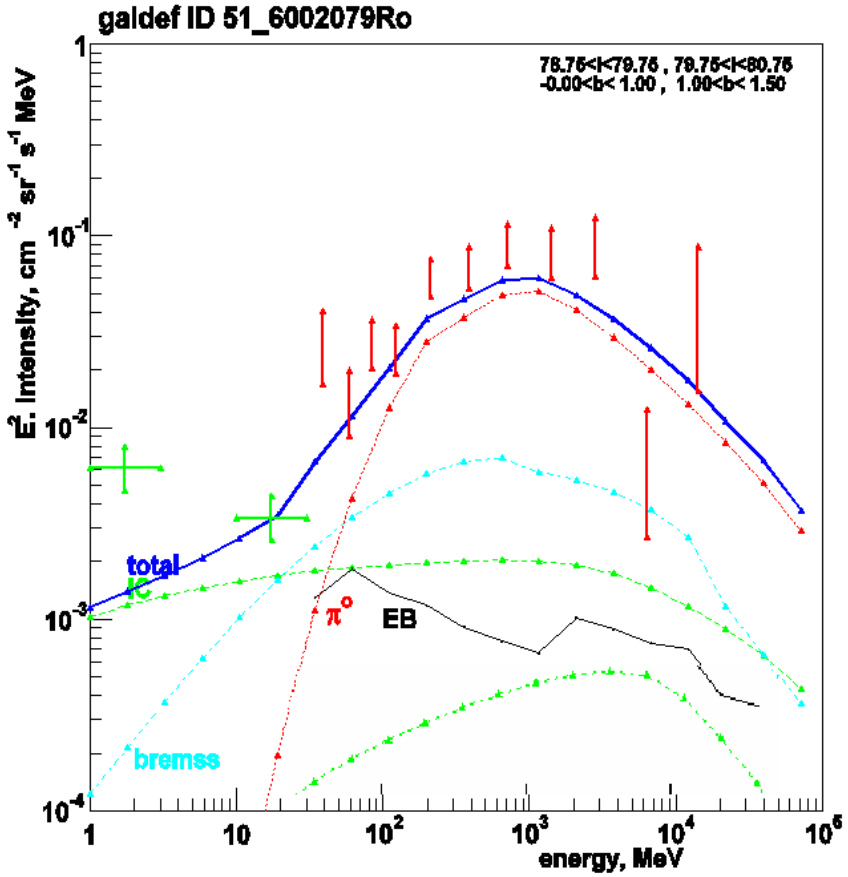

Figure 2.13: Gamma-ray spectrum of the Cygnus region. The lower green line represents the inverse-Compton emission predicted in my work from Cyg OB2, centred on the cluster, while the higher green one represents the total inverse-Compton emission from the Galaxy in this region as calculated by GALPROP Strong et al. (2004b). The red bars are the EGRET data, the thick black line the extragalactic back-ground, as in Strong et al. (2004b). The blue solid line represent the total galactic emission, the blue dashed line the bremsstrahlung and the red line the pion decay calculated with the optimized electron spectrum from GALPROP (Strong et al. 2004b).

Chapter 3

Gamma-ray emission from the Sun: theory, analysis with EGRET data and perspectives for GLAST

3.1 Introduction

Solar quiet gamma-ray astronomy started playing a significant role in the early 1990's thanks to the EGRET mission. Hudson (1989) pointed out the importance of gamma-ray emission from the quiet Sun as an interesting possibility for sensitive instruments such as EGRET. Seckel et al. (1991) estimated that the flux of gamma rays produced by cosmic-ray interactions on the solar surface would be detectable by EGRET. This emission is the result of particle cascades initiated in the solar atmosphere by Galactic cosmic rays. Meanwhile Thompson et al. (1997) detected in the EGRET data the gamma rays produced by cosmic ray interactions with the lunar surface. Although they expected similar interactions on the Sun, the EGRET data they analyzed did not show any excess of gamma rays consistent with the position of the Sun. They obtained an upper limit of the flux above 100 MeV of $2 \times 10^{-7}\mathrm{cm}^{-2}\mathrm{s}^{-1}$. Fairbairn et al. (2007), analyzing the EGRET data of the solar occultation of 3C279 in 1991, found a photon flux of about 6×10^{-7} $\mathrm{cm}^{-2}\mathrm{s}^{-1}$ above 100 MeV in the direction of the occulted source, which they used to put limits on axion models; however they did not consider the extended solar emission.

Inverse Compton scattering of cosmic-ray electrons on the solar photon

halo around the Sun has been estimated to be an important source of gamma-ray emission (Orlando & Strong 2007a; Moskalenko et al. 2007). In our previous work, we predicted this to be comparable to the diffuse background even at large angular distance from the Sun. The formalism in this thesis has been improved and more accurate estimates have been obtained. The anisotropic scattering formulation and the solar modulation have been implemented, in order to give a more precise model for the EGRET data. In this work we explain in detail our model of the extended emission produced via inverse Compton scattering of cosmic-ray electrons on the solar radiation field.

In this thesis I described the full analysis including the spectrum of disk and extended components. My result is very promising for the GLAST mission which certainly will be able to detect the emission even at larger angular separation from the Sun. Moreover, the extended emission from the Sun has to be taken into account since it can be strong enough to be a confusing background for Galactic and extragalactic diffuse emission studies.

3.2 Theoretical model

Inverse-Compton scattering of solar optical photons by $\sim$ GeV cosmic-ray electrons produces γ-radiation with energies of 100 MeV and above. Improving on the approximate estimates given in Orlando & Strong (2007a), in this chapter the anisotropic formulation of the Klein-Nishina cross section will be introduced, taking into account the radial distribution of the photons propagating outward from the Sun. My elegant analytical formulation used in Chapter 2 has been replaced by a numerical solution depending on the angle between the momenta of the cosmic ray electrons and the incoming photons. As pointed out in Chapter 2 this will affect the results at about the 10% level. Moreover, while in my previous work I used the modulated cosmic-ray electron spectrum as observed at earth, here a formulation of the solar modulation as a function of the distance from the Sun has been taking into account.

The gamma-ray intensity spectrum is given by eq.(2.3). The cosmic-ray electrons have been assumed isotropically distributed everywhere in the heliosphere. In Orlando & Strong (2007a), an elegant analytical formulation in eq (2.10) was obtained for the isotropic case, assuming a simple inverse square law for the photon density for all distances from the Sun and a cosmic ray electron spectrum considered constant for all distances and determined from experimental data (see Fig.(3.6)) for 1 AU. For the case of the anisotropic

formulation of the Klein-Nishina cross section and for the electron modulation along the line of sight, we have to use numerical computations.

3.2.1 Solar photon field

3.2.1.1 Basic relations

The Sun is treated as black body where the energy density is characterized by the effective temperature on the surface (T=5777 K) following the Stephan-Boltzmann equation. For the photon density close to the Sun, the simple inverse square law is inappropriate. In this Chapter the emission from an extended source has been evaluated. The distribution of photon density from the Sun, as extended source, is given by integrating over the solid angle with the variables shown in Fig.(3.1)

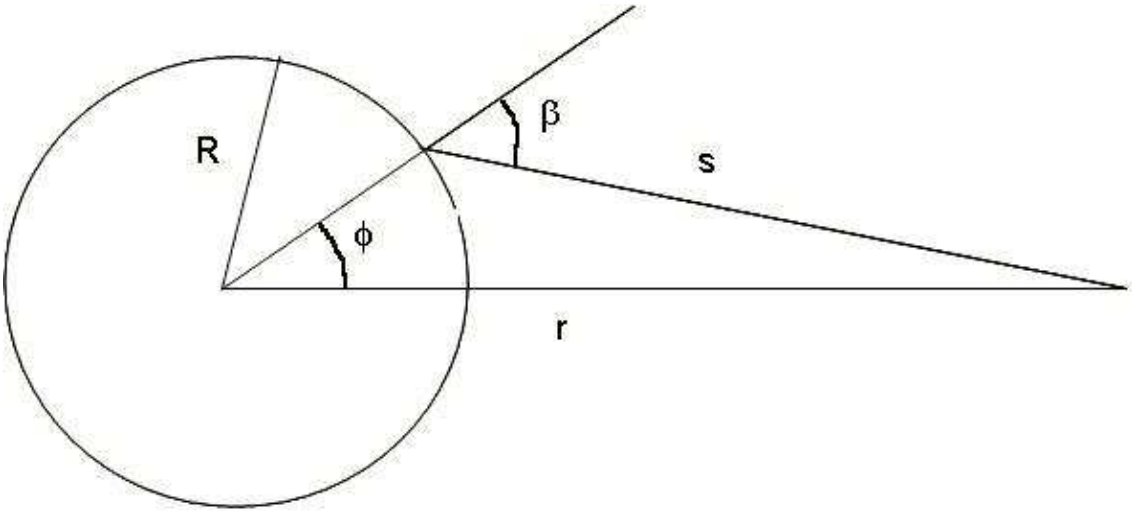

Figure 3.1: Variables involved in eq.(2.12) for the calculation of the photon density around the Sun, where R is the solar radius and r is the distance from the Sun to the line of integration (see Fig. 2.4).

$$n_{ph}(E_{ph}, r) = n_{BB}(E_{ph}) \int_0^{\phi_{MAX}} \frac{2\pi\ R^2\ sin\ \phi\ cos\ \beta\ d\phi}{4\pi\ s^2}$$
$$= 0.5\ n_{BB}(E_{ph}) \left[1 - \sqrt{1 - (R/r)^2}\right] \quad (3.1)$$

with $cos\ \beta$=$(r\ cos\ \phi\ -\ R)/s$ and $cos\ \phi_{MAX}\ =\ R/r$. For large distances from the Sun it reduces to the inverse square law. Fig.(3.2) shows the difference between the photon density close to the Sun with the more precise formulation

and the approximation for a point source. For large distances from the Sun it reduces to the well known inverse square law.

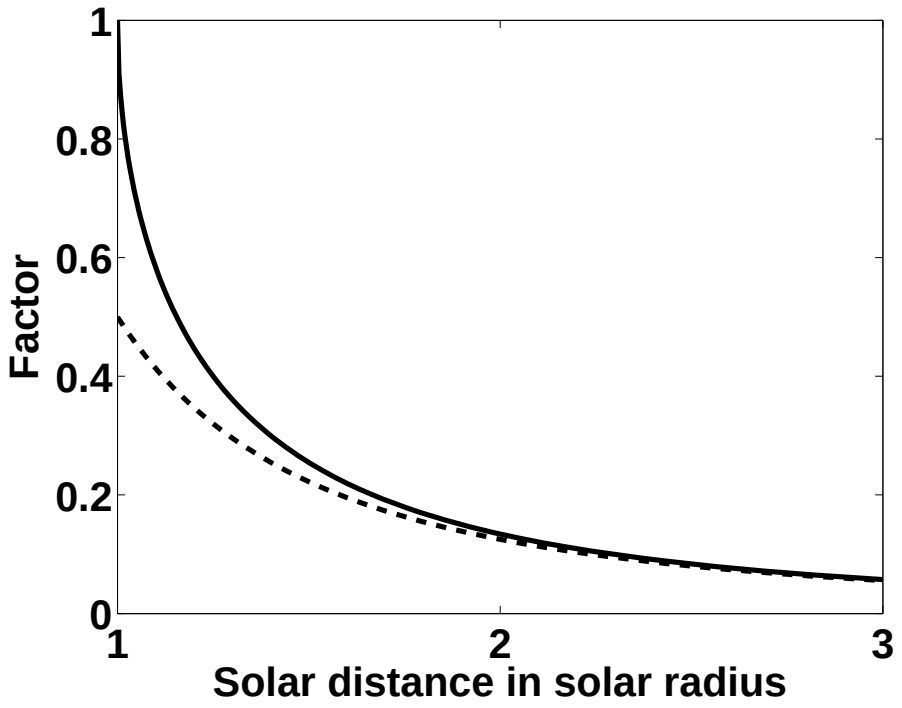

Figure 3.2: Difference between the photon density close to the Sun with the more precise formulation (solid line) given in eq.(2.12) and the inverse-square approximation for point source (dashed line) normalized to unit.

3.2.1.2 Deviations of solar spectrum from black body

We checked the effect of deviations of the solar spectrum from a black body. We used the black-body approximation with the AM0 solar spectrum [1], referring to 2007, period of solar minimum, extrapolated back to the Sun.

The energy density of a source irradiating as a black body in terms of the frequency of the light is:

$$u_\nu d\nu = \frac{2\pi h\nu^3/c^3}{e^{h\nu/kT}-1} d\nu \tag{3.2}$$

The total photon density, n_{BB} in units of cm^{-3}, is found by integrating over all frequencies the previous formula divided by the photon energy, i.e.:

$$n_{BB} = \int_0^\infty \frac{2\pi h\nu^3/(c^3 h\nu)}{e^{h\nu/kT}-1} d\nu \tag{3.3}$$

[1] taken from http://www.spacewx.com/

In Fig.(3.3) we compare the black body approximation with the AM0 Sun spectrum, extrapolated to the Sun. Irradiance variability for different solar condition is at a level of few percent, in this energy range and, in the first order, can be neglected. The estimated inverse Compton emission from the Sun is not affected significantly ($<0.5\%$) by the different spectra (Fig.(3.4)).

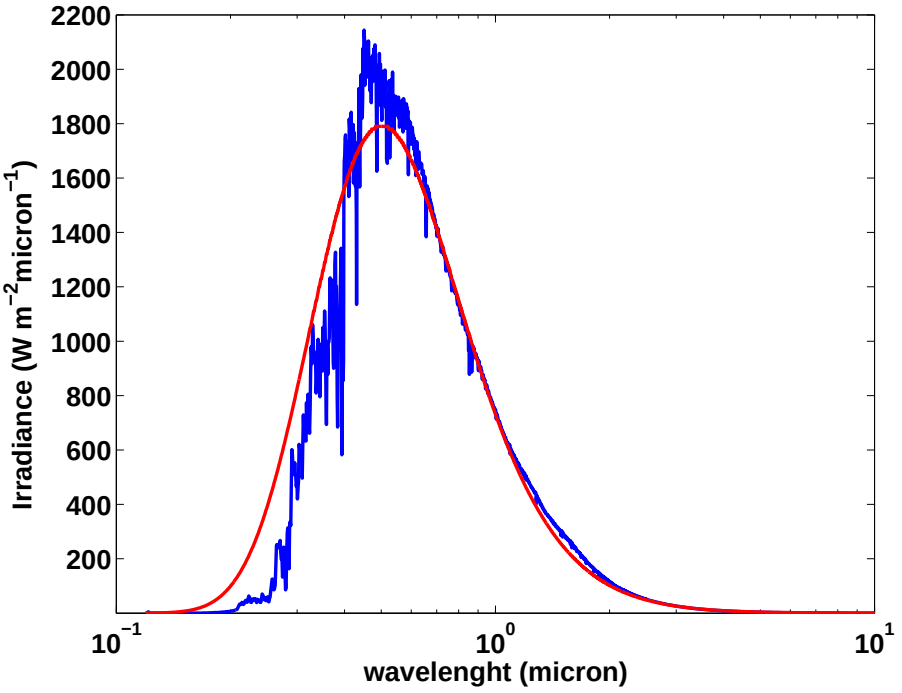

Figure 3.3: AM0 spectrum extrapolated to the Sun (blue line) and the black body spectrum distribution (red line) from 0.1 to 10 microns.

Hence I decided to keep the black body approximation for simplicity and even for GLAST the deviation form balk-body can be safely neglected.

We also verify that the EUV and XUV ranges of the solar spectrum do not affect the inverse-Compton emission. The irradiance at the shortest wavelengths varies significantly with solar conditions and the range of variability spans a few percent at the longest wavelengths, from 40% to more than 500% across the EUV and XUV , from solar minimum to solar maximum. Moreover, during solar flare, XUV increases, reaching factors of eight or more, and EUV increases on the order of 10-40% (Eparvier & Woods 2003). However, Oncica et al. (2002) found that the X-ray flares cannot contribute to the total solar irradiance fluctuations and even the most energetic X-ray flares cannot account for more than 1 mW/m^2. We found that the estimated inverse-Compton emission from the Sun is not affected significantly by the XUV/EUV flux and

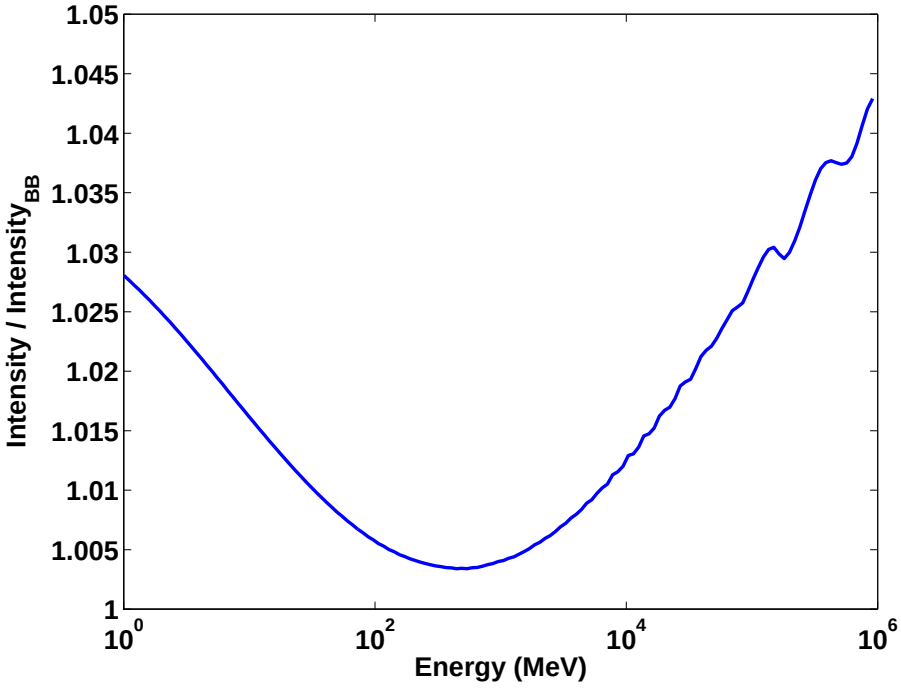

Figure 3.4: Ratio between estimated inverse Compton emission for the AM0 spectrum (0.1-10 microns) extrapolated to the Sun and the black body distribution, for the isotropic case. The estimated inverse Compton emission from the Sun has not been affected significantly ($<0.5\%$ in the MeV range).

its variability.

3.2.2 Comparison of isotropic/anisotropic formulations

Since for the case of the Sun a sensitivity around 10% would be required in order to distinguish between different models of solar modulation (see next paragraph), we need to use the anisotropic Klein-Nishina cross section which gives a more precise description of the mechanism of emission. The integrated inverse-Compton emission was compared for isotropic and anisotropic cross sections (Fig 3.5); the maximum difference of the intensity for the two Klein-Nishina cross sections is about 15% around 300 MeV.

3.2.3 Electron spectrum and solar modulation

The intensity of Galactic cosmic rays is inversely correlated to the solar activity. The solar modulation is very important since it changes the interstellar spectrum of cosmic ray particles below 20 GeV/nucleon during their propaga-

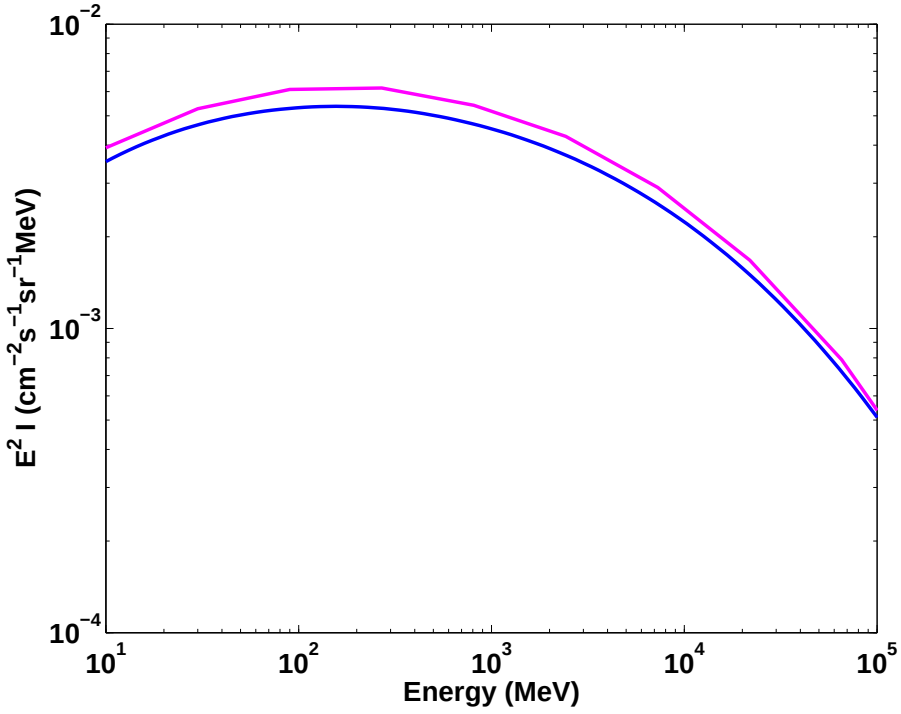

Figure 3.5: Estimated emission for the isotropic case (red line) and the anisotropic case (blue line), using the local interstellar electron spectrum. The maximum difference for the two Klien-Nishina cross sections is about 15% around 300 MeV. This plot is calculated for 0.5° angular distances from the Sun.

tion inside the heliosphere. It is established that sunspot number increases during periods of high solar activity, which is characterised by the switching of polarity of the Sun's magnetic field. The 22-year cycle can, in fact, be broken down into two 11-year cycles that include two pairs of minimum and maximum activity. During the first stage of the cycle, known as the A $>$ 0 phase, the Sun is relatively quiet; its magnetic field has positive polarity at the solar north pole and negative polarity at the south pole. A period of greater solar activity, known as solar maximum, follows as temperature gradients and sunspot numbers increase on the surface of the Sun. During this time, the structure of the solar magnetic fields becomes more complex and solar wind speeds increase. The next stage of minimum activity occurs at the A $<$ 0 phase when the magnetic field has reoriented itself, with positive polarity at the south pole and negative polarity at the north. A similar period of maximum activity occurs as the magnetic field returns to the A $>$ 0 phase.

Modulated spectra of CR are the actual ones measured by balloon-borne

and spacecraft instruments. The "solar modulation" is a combination of the effects of convection by the solar wind, diffusion, adiabatic cooling, drifts, and diffusive acceleration. The solar modulation of cosmic ray electrons has been widely studied, but is still not completely understood. Müller-Mellin et al. (1977) analyzed the data of Helios-1 from 1974 to 1975, a period that corresponds to the approach to solar minimum, and reported measurements of proton and helium cosmic ray intensities for the 20-50 MeV/n energy interval between 0.3 and 1 AU. The proton gradients they obtained were small and generally consistent with zero, while the helium gradients were positive but small. On the basis of Helios-1 data, (Kunow et al. 1975) stated: 'The radial variation seems to be very small for all particles and all energy ranges'. The study of (Seckel et al. 1991) was based on this hypothesis. Since that time, the modulation theories have been developed including effects like drifts and current sheet tilt variations (Jokipii & Thomas 1981) and short time variations. In this work we care only about long period modulations for solar maximum and minimum and we assume that the longitude gradient is negligible. McDonald et al. (2003), analyzing cycle 20 and 22 of solar minimum between 15 and 72 AU, found that most of the modulation in this period occurs near the termination shock (assumed to be at 100 AU). On the other hand, from solar minimum to solar maximum the modulation increases mainly inside the termination shock. Recently Morales-Olivaresi & Caballero-Lopez (2007), investigating the radial intensity gradients of cosmic rays from 1 AU to the distant heliosphere and interpreting the data from IMP8, Voyagers 1 and 2, Pioneer 10 and BESS for Cycles 21, 22 and 23, found different radial gradients in the inner heliosphere compared to McDonald et al. (2003). In this region they obtained an average radial gradient of $\simeq$ 3% /AU for 175 MeV H and $\simeq$ 2.2% /AU for 265MeV/n He, that, at 1AU, give an intensity smaller than McDonald et al. (2003) for H and higher for He. Gieseler et al. (2007) analyzed the data from Ulysses from 1997 to 2006 at 5AU. They found a radial gradient of 4.5%/AU for α particles with energies from 125 to 200 MeV/n, which is consistent with previous measurements.

In this work, our model of the modulation of cosmic rays uses the formulation given in Gleeson & Axford (1968), using the studies regarding the radial distribution of cosmic rays in the heliosphere at solar minimum and maximum. The cosmic ray electron spectrum is given by the well known force field approximation of cosmic ray nuclei used to obtain the modulated differential intensity J(r,E) at energy E and distance r from the Sun (Gleeson & Axford

1968). As demonstrated by Caballero-Lopez & Moraal (2004) it is a good approximation for Galactic cosmic rays in the inner heliosphere. The differential intensity of the modulated spectrum is given by:

$$J(r,E) = J(\infty,\ E + \Phi(r))\ \frac{E(E+2E_0)}{(E+\Phi(r)+2E_0)(E+\Phi(r))} \tag{3.4}$$

where E is kinetic energy in MeV and E_0 is the electron rest mass. We use the local interstellar electron spectrum $J(\infty,\ E + \Phi(r))$. $\Phi(r) = (Ze/A)\phi$ where ϕ is the modulation potential, Z the charge number and A the mass number. In order to compute the modulation potential in the inner heliosphere, we used the parameterization found by Fujii & McDonald (2005) for Cycle 21 from 100 AU to 1 AU, neglecting the time dependence and normalizing at 1 AU for 500 MV (solar minimum) and 1000 MV (solar maximum). As in Moskalenko et al. (2007) we find:

$$\Phi(r) = \Phi_0(r^{-0.1} - r_b^{-0.1})/(1 - r_b^{0.1}) \tag{3.5}$$

where Φ_0 is the modulation potential at 1 AU, of 500 and 1000 MV for solar minimum and maximum respectively; $r_b = 100AU$ and r is the distance from the Sun in AU. Figure (3.6) shows the local interstellar electron spectrum (Strong et al. 2004a) and the modulated spectrum at 1 AU, compared with the data. The electron intensity as a function of distance from the Sun is given in Fig.(3.7) for different energies and for modulation potential 500 MV.

The major contribution to the energy range 100-500 MeV we are interested in comes from electrons with energy between 1 and 10 GeV, as shown in Fig. (3.8), obtained for the local interstellar electron spectrum, with no modulation. To compute the inverse-Compton extended emission from the heliosphere and compare it with the EGRET data, details of the solar atmosphere, the non-isotropic solar wind and the asymmetries of the magnetic field have been neglected, considering the limited sensitivity of EGRET. Since the biggest uncertainties in the gamma-ray emission come from the cosmic-ray electron spectrum close to the Sun, in our model we considered two possible configurations of the solar modulation within 1 AU. The "naive" approximation is to assume that the cosmic-ray flux towards the Sun equals the observed flux at Earth, since there is evidence (see discussion above) that modulation by the solar wind does not significantly alter the spectrum once cosmic rays have penetrated as far as Earth. Moreover, high energy electrons are less sensitive to the modulation. This approximation gives an upper limit on the modelled flux. The other approach is to assume that the electron spectrum

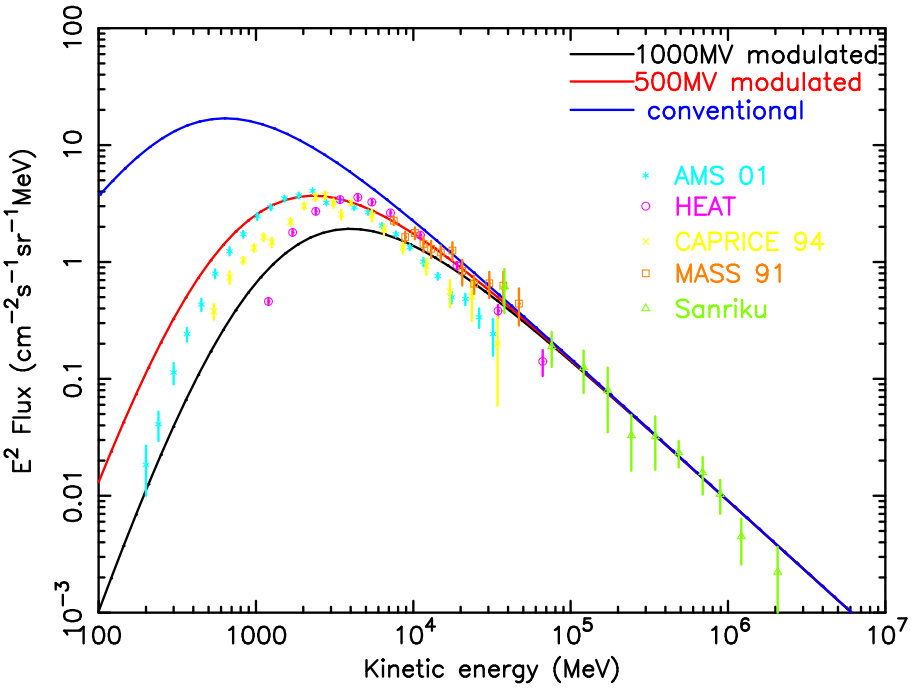

Figure 3.6: Local interstellar electron spectrum (blue line) as in Strong et al. (2004a) and the modulated at 1 AU of 500 MV (red line) and 1000 MV (black line) compared with the data. See Strong et al. (2004a) for data references.

varies due to solar wind effects within 1 AU. With this "nominal" approximation we assume that the formulation for solar modulation from 100 AU to 1AU can be extrapolated also below 1 AU, using eq. (3.4). This gives an approximate lower limit in our model.

3.2.4 Calculated extended solar emission

Figure (3.9) shows the spectrum of the emission for two different angular distances from the Sun, without modulation and for two levels of solar modulation (Φ=500, 1000 MV, respectively for solar minimum and solar maximum) and for the cases of upper and lower limits described above.

The angular profile of the emission is shown in Fig.(3.10) above 100 MeV without modulation, for two levels of solar modulation (Φ=500, 1000 MV) and for the cases naive and nominal. The emission is extended and is important compared to the extragalactic background (around 10^{-5}cm^{-2}s^{-1}sr^{-1}) even at very large angles from the Sun. Even around 10° it is still about 10% of the extragalactic background and with the sensitivity of GLAST should be included in the whole sky diffuse emission. An example of the intensity of the

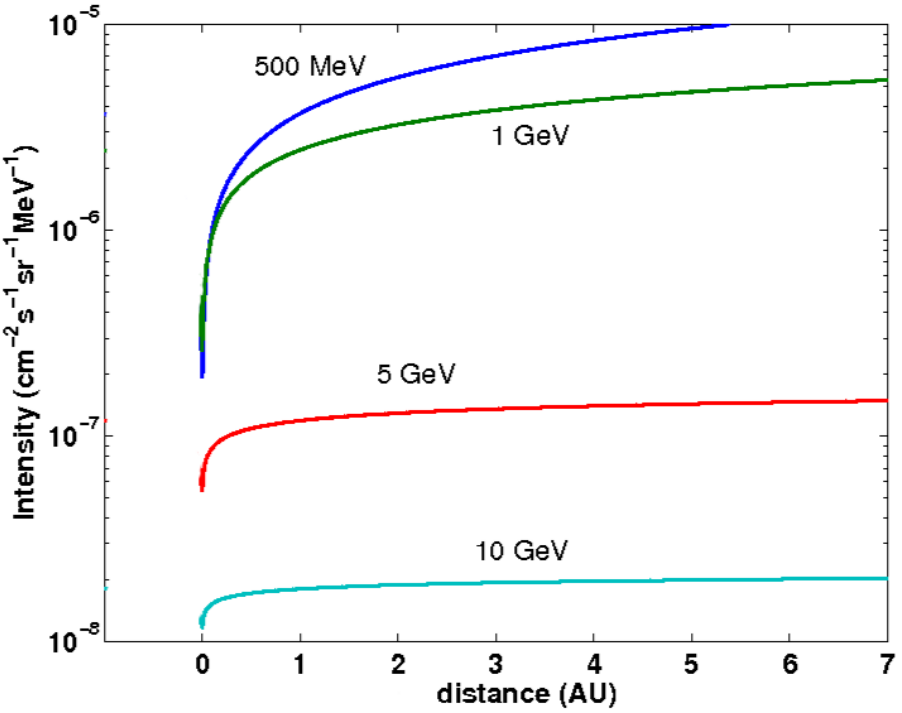

Figure 3.7: Electron intensity as a function of distance from the Sun in AU, where 0 corresponds to the Sun, for different energies and for modulation potential $\Phi_0 = 500MV$.

inverse-Compton emission predicted in a region of 10° from the Sun is shown in Fig.(3.11) for 300-500 MeV.

While the inverse Compton emission is expected to be readily detectable in future by GLAST, the situation for available EGRET data is more challenging. In the following section we present our study with the EGRET database.

3.3 EGRET data preparation and selection

We analyzed the EGRET data using data provided by D. Petry who developed a code for moving target such as the Earth (Petry 2005). This code permits to produce images centred on a moving source and traces of other sources around with respect to the centred source. To perform the analysis for the Sun, we analyzed the data in a Sun-centred system. In order to have a better sensitivity and hence detection of our emission component, the diffuse background was reduced by excluding the Galactic plane within 15° latitude. Otherwise all available exposure from October 1991 to June 1995 was used (viewing pe-

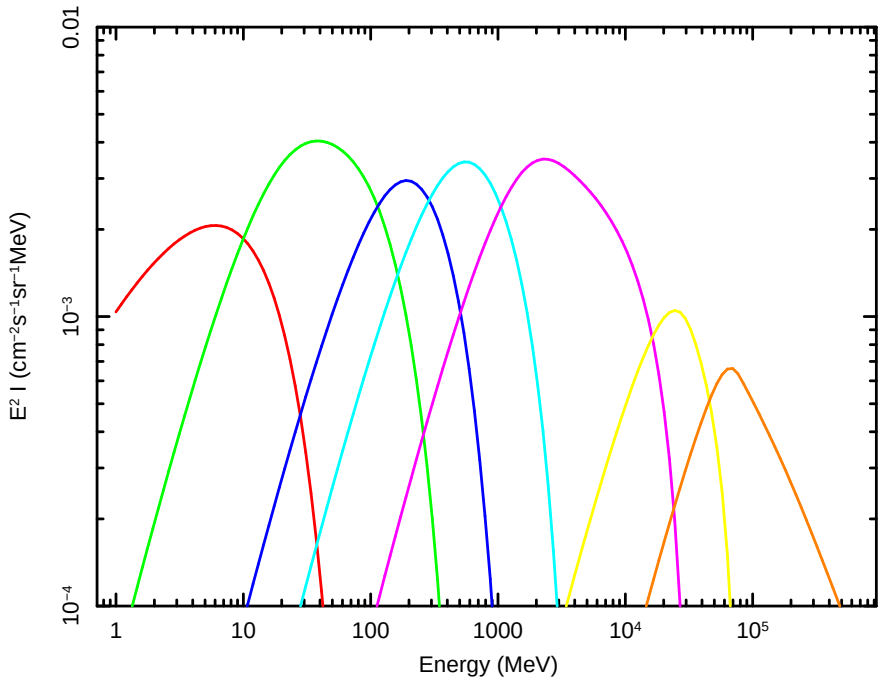

Figure 3.8: Contribution to the solar IC emission for different electron energy ranges, left to right: $100 - 10^3$ MeV, $(1 - 3) \times 10^3$ MeV, $(3 - 5) \times 10^3$ MeV, $(0.5 - 1) \times 10^4$ MeV,$(1 - 5) \times 10^4$ MeV, $(0.5 - 1) \times 10^5$ MeV, $1 \times 10^5 - 5 \times 10^7$ MeV.

riods 1, 11, 12, 19, 26, 209, 221, 320, 325, 410, 420), excluding the big solar flare in June 1991. When the Sun passed by other gamma-ray sources (moon, 3C 279 and several quasars), these sources were included in the analysis. In order to obtain the flux of the moon to be fitted, the same method performed for the Sun has been made with all data moon centred.

3.4 Statistical method

For each case analysed, we obtained the logarithm of the likelihood ratio log (L/L_0) where L is the likelihood of the data with the all components included, and L_0 is the null hypothesis. We used both frequentist and Bayesian approach to analyze the results. More details are given below.

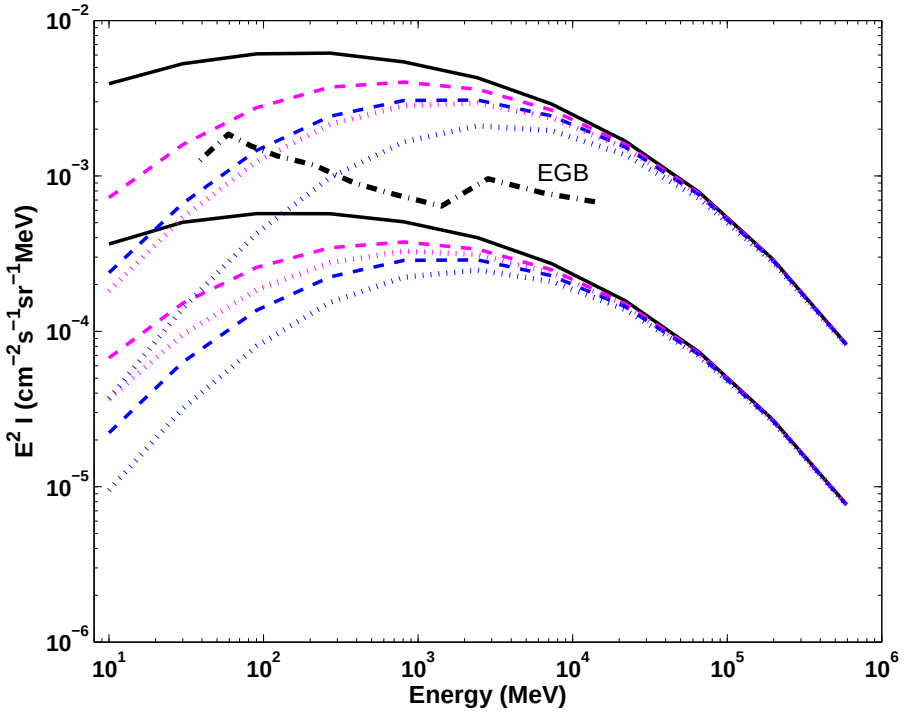

Figure 3.9: Spectrum of the gamma-ray emission for (top to bottom) 0.5° and 5° angular distances from the Sun and for different conditions of solar modulation. Solid lines: no modulation, pink lines: Φ_0=500MV, blue lines: Φ_0=1000MV, dashed lines: naive model, dotted lines: nominal model. EGB is the extragalactic background as in Strong et al. (2004b)

3.4.1 Maximum likelihood multiple fitting technique

The likelihood statistic of binned data is the product of the probability of each pixel:

$$L = \prod_{ij} p_{ij} \tag{3.6}$$

where

$$p_{ij} = \frac{\theta_{ij}^{n_{ij}}\ e^{-\theta_{ij}}}{n_{ij}!} \tag{3.7}$$

is the Poisson probability of observing n_{ij} counts in pixel (ij) where the number of counts predicted by the model is θ_{ij}. Using this Poisson distribution (which tends toward a Gaussian distribution as statistics increase), small number statistics do not pose a problem. The logarithm of the likelihood has a more convenient form:

$$log\ L = \sum_{ij} n_{ij}\ log(\theta_{ij} - \sum_{ij} \theta_{ij} - \sum_{ij} log(n_{ij}) \tag{3.8}$$

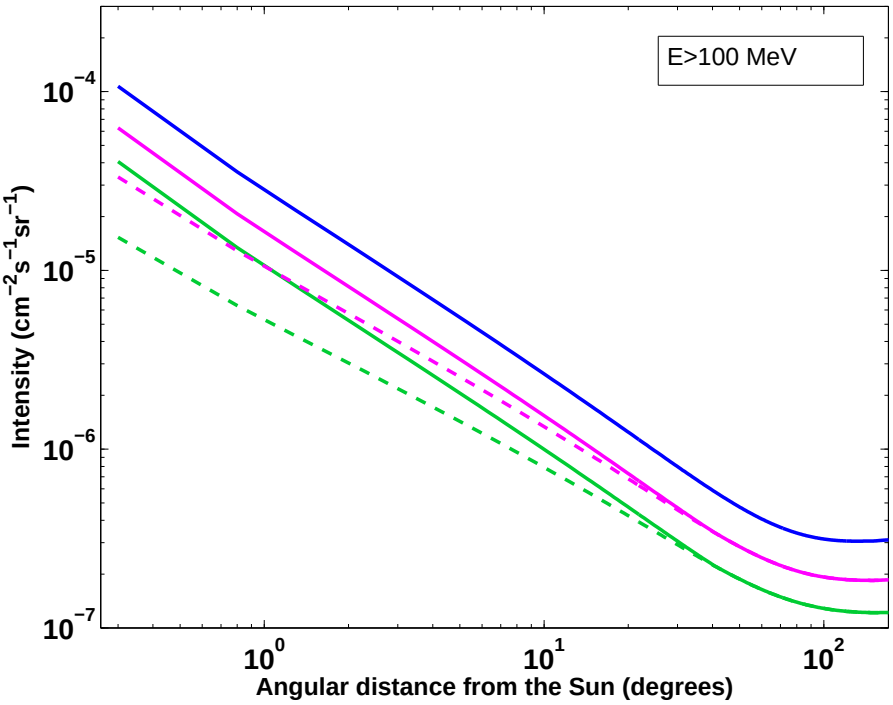

Figure 3.10: Angular profile of the emission as a function of the angular distance from the Sun above 100 MeV. Blue line: no modulation, pink lines: Φ_0=500MV, green lines: Φ_0=1000MV, solid lines: naive model, dashed lines: nominal model.

Last term is model independent and can be neglected. The first term causes log$L$ to increase as the model predict counts in pixels where they actually occur. In Mattox et al. (1996) the likelihood ratio test is used for the analysis of the EGRET data and determining the significance of the sources. The likelihood ratio is the likelihood of the null hypothesis for the data divided by the likelihood of the alternative hypothesis for the same data. In fact Wilks (1938) demonstrated that -2 log (L/L_0) is distributed as χ^2 in the null hypothesis with L the alternative hypothesis. Hence the significance of an EGRET detection of a source at a specific position is given by twice the square root of the likelihood ratio σ (Mattox et al. 1996). Thus for each parameter, a decrease in log$L$ of 1/2 from its maximum value corresponds to the 68% confidence (1 σ) region for one parameter. The quality of the fit is indicated by χ^2 and its associated probability, while generally the Gaussian statistics is assumed and the standard deviation σ determines the width of the distribution. (Strong 1985) uses -2 log (L/L_m) distributed as χ^2_n, where n is the number of parameters held fixed and L_m is the global maximum.

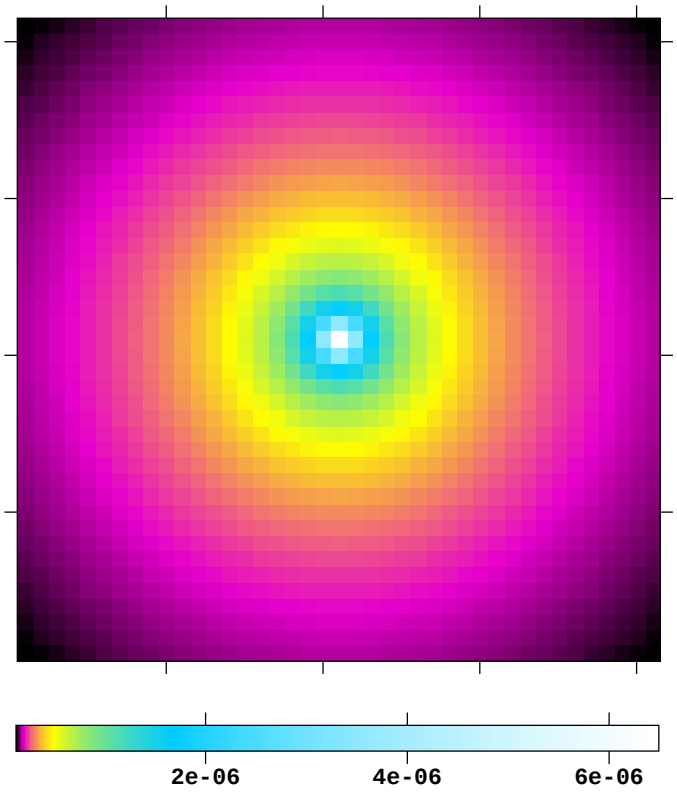

Figure 3.11: Inverse-Compton emission modelled for a region of 10° from the Sun for 300-500 MeV and for the naive model of 1000 MV modulation. Intensity is given in $cm^{-2}s^{-1}sr^{-1}$. In the figure, the minimum value of the intensity is 1.2×10^{-7} $cm^{-2}s^{-1}sr^{-1}$.

In order to calculate the confidence levels for one-parameter fit, for any distribution even if not symmetric around the best fit value, we consider the region on each side of the mean value separately and estimate two separate standard deviations. This is equivalent to find the two positions at which the logarithm of the likelihood ratio has decreased by 1/2 (Bevington et al. 1993). Clearly this result is somewhat subjective if either side of the curve does not follow the Gaussian form. Suppose we have 5 variables correlated like in a multi-parameter fit and we want to calculate the confidence intervals for the variables. By allowing the four parameters a a_1, a_2, a_3 and a_4 to find their optimum values for each chosen value of a_4 and varying a_4, we have 1 degree of freedom and the parameter variation separately must follow its appropriate χ^2 distribution for one degree of freedom, so that $\delta\chi^2$ <1 corresponds to 1 σ and $\delta\chi^2$ <4 to 2 σ with all other parameters optimized (Bevington et al. 1993). To find 1 σ region encompassed by the joint variation of two parameters, a_4

and a_5, with all other parameters optimized, we need the region where $\delta\chi^2$ <2.3, while for 2 σ we have $\delta\chi^2$ <2.3, corresponding to $\delta\chi^2$ for 2 degrees of freedom (Bevington et al. 1993).

3.4.2 Bayesian formulation

The frequentist approach to statistics, described above, and the Bayesian approach address the same question but with different methodology. The philosophical difference is that Bayesian methods is based on comparison among alternative hypothesis using the single data set, in contrast, frequentist methods average over hypothetical alternative data samples, and consider hypothesis to be irrelevant.
In order to have a better treatment of our results, we performed also a Bayesian analysis treating likelihood as probability with uniform prior distribution (see eg. Strong et al. 2005). This is independent of assumptions about distribution of the likelihood ratio. In fact, usually when the number of data is large, the Bayesian estimates agree with those from a Gaussian approximation. On the other hand when the number of data is small, the probability may be not symmetric around the best fit. Hence, the mean value of one parameter is given by:

$$x_{io} = \int x_i P(x_i)\ dx_i \tag{3.9}$$

where

$$P(x_i) = \int_{i \neq j} P(\underline{x}) d^{n-1}x \tag{3.10}$$

is the marginal probability of x_i with x_j any value with i≠j, n is the number of the parameters and P($\underline{x}$) is the normalized joint probability distribution of $\underline{x}$, such that

$$\int P(\underline{x}) d^n x = 1 \tag{3.11}$$

The mean square error is then given by:

$$\Delta x_i^2 = \int (x_i - x_{i0})^2 P(x_i) dx_i \tag{3.12}$$

When we are interested in the errors in the sum of the two components (i.e. disk and extended emission) we have to take into account their covariance, since they are correlated. Hence,

$$\begin{aligned} (\Delta(x_i + x_k))^2 &= (\Delta x_i)^2 + (\Delta x_k)^2 \\ &+ 2 \int (x_i - x_{i0})(x_k - x_{k0})\ P(\underline{x}) d^n x \end{aligned} \tag{3.13}$$

3.5 EGRET analysis

We fitted the EGRET data in the Sun-centred system using a multi-parameter likelihood fitting technique. The region used for fitting is a circle of radius 10° around the Sun. The total number of counts predicted includes inverse Compton and solar disk flux, the moon, QSO 3C279, other background sources and the background. We left as free parameters the solar extended inverse-Compton flux from the model, the solar disk flux (treated as point source since the solar disk is not resolvable by EGRET), a uniform background, and the flux of 3C279 - the dominant background point source. The moon flux was determined from moon-centred fits and the 3EG source fluxes were fixed at their catalogue values. All components were convolved with the energy-dependent EGRET PSF.

3.5.1 Model of extended solar emission

The solar extended inverse-Compton emission was modelled within 10° radius from the Sun and with a pixel size of 0.5°. The model was convolved with the energy-dependent EGRET PSF and implemented in the fit, with a scale factor as free parameter. We took into account the different approximations to the modulation described above, since the data we used cover a period from October 1991 when there was a solar maximum to June 1995 close to the solar minimum. Since the emission we are looking for is very close to the EGRET sensitivity limit, we had to take as much exposure as possible and it was not possible to perform an analysis splitting the data according to solar modulation.

3.5.2 3C279

Since 3C 279 is the brightest source that passes at angles close to the Sun, we decided to leave its flux as free parameter in the fit. We fixed the spectral index at 1.96, the value given in the EGRET catalogue. The flux obtained was then compared to that in the EGRET catalogue.

3.5.3 Other point-like background sources

Many sources passing within 10° from the Sun were included in the analysis. We decided to implement their fluxes as fixed parameters. With the code

Table 3.1: Parameters of the background sources used for the analysis.

Source	Flux (>100 MeV)[a]	spectral index
J0204+1458	2.36	2.23
J0215+123	1.80	2.03
J1230-0204	1.13	2.85
J1235+0233	1.24	2.39
J1246-0651	1.29	2.73
J1310-0517	1.04	2.34
J1409-0745	2.74	2.29
J2321-0328	3.82	- [b]

[a] Units 10^{-7} cm^{-2}s^{-1}

[b] The choice of the spectral index we used is explained in the text

(Petry 2005) it was possible to know the exact viewing period of any source and hence to determine its flux from the 3rd EGRET catalogue (Hartman et al. 1999). Hence, we took the flux value in the EGRET catalogue corresponding to the period we used, when this was listed. Since the catalogue does not contain the flux values corresponding to all the periods in which the sources were close to the Sun, in case of uncertainty we decided to use the first entry in the catalogue, which is the one from which the source position was derived. In almost all cases, this is the detection with the highest statistical significance, which in most cases corresponds to the maximum value of the flux. We also took the spectral index from the EGRET catalogue. The values adopted for the sources are listed in Table (3.1). Since the spectral index of J2321-0328 is not known, the fit was performed without this source above 300 MeV, since in the literature there is no evidence of its detection above this energy. In order to verify that this choice does not affect significantly the fit result, we tested also a typical spectral index of 2. Both fitting results will be reported in the following results section. The traces of the background quasars were added together in the same data file, re-scaled according to their fluxes.

3.5.4 Diffuse background

Since the count maps used for our analysis include only data above $|b| > 15^\circ$ latitude, and the Galactic plane is excluded, the Galactic emission can be well approximated by an isotropic term. We left its intensity as a free parameter in the fitting analysis.

Table 3.2: Fitting results for the moon

Energy (MeV)	Moon flux ($cm^{-2}s^{-1}$)	Background ($cm^{-2}s^{-1}sr^{-1}$)
> 100	$(5.55 \pm 0.65) \times 10^{-7}$	3.47×10^{-5}
> 300	$(5.76 \pm 1.66) \times 10^{-8}$	1.01×10^{-5}
$100 - 300$	$(4.98 \pm 0.57) \times 10^{-7}$	2.13×10^{-5}

3.5.5 Moon

The flux of the moon was determined from moon-centred data, fitting the flux and an isotropic background. Since the moon moves quickly across the sky, all other sources moving by are adequately taken into account as a constant component included in the isotropic background. The fit was performed for 2 energy ranges: 100-300 MeV and >300 MeV. The value of flux of the moon for the different energy ranges was obtained by maximum likelihood. The maximum likelihood ratio statistic used for this analysis is described in the appendix. The values of the best fit fluxes and 1σ errors are given in Table (3.2). Previous studies of the EGRET data (Thompson et al.) gave a flux of $(5.4 \pm 0.7) \times 10^{-7}$ cm^{-2}s^{-1} above 100 MeV in agreement with our analysis. The spectrum of the moon shown in Fig.(3.12) has been obtained imposing a constant spectral index γ, extrapolated up to 2 GeV.

The lunar spectral index was determined as $3.05^{+0.38}_{-0.29}$. Errors are calculated from the uncertainties on the integrated fluxes. Since the EGRET data we used to analyze the emission from the Sun extend from solar maximum to minimum, in this analysis we estimated an average lunar flux between the two periods of solar modulation. Comparing our spectrum with the model of Moskalenko & Porter (2007) for different solar conditions, we find a good agreement at 100 MeV, while at higher energies the model is about a factor of two higher.

3.6 Solar analysis results

The analysis was performed for 2 energy ranges : 100-300 MeV and above 300 MeV as well as the combination to improve the detection statistics. This choice was determined by the limitations of the EGRET data. Fig.3.13 shows the smoothed count maps, centred on the Sun, for those energy ranges and for a region of 20° side. The fitting region has a radius of 10° centred on the Sun. Since the interesting parameters are solar disk source and extended emission,

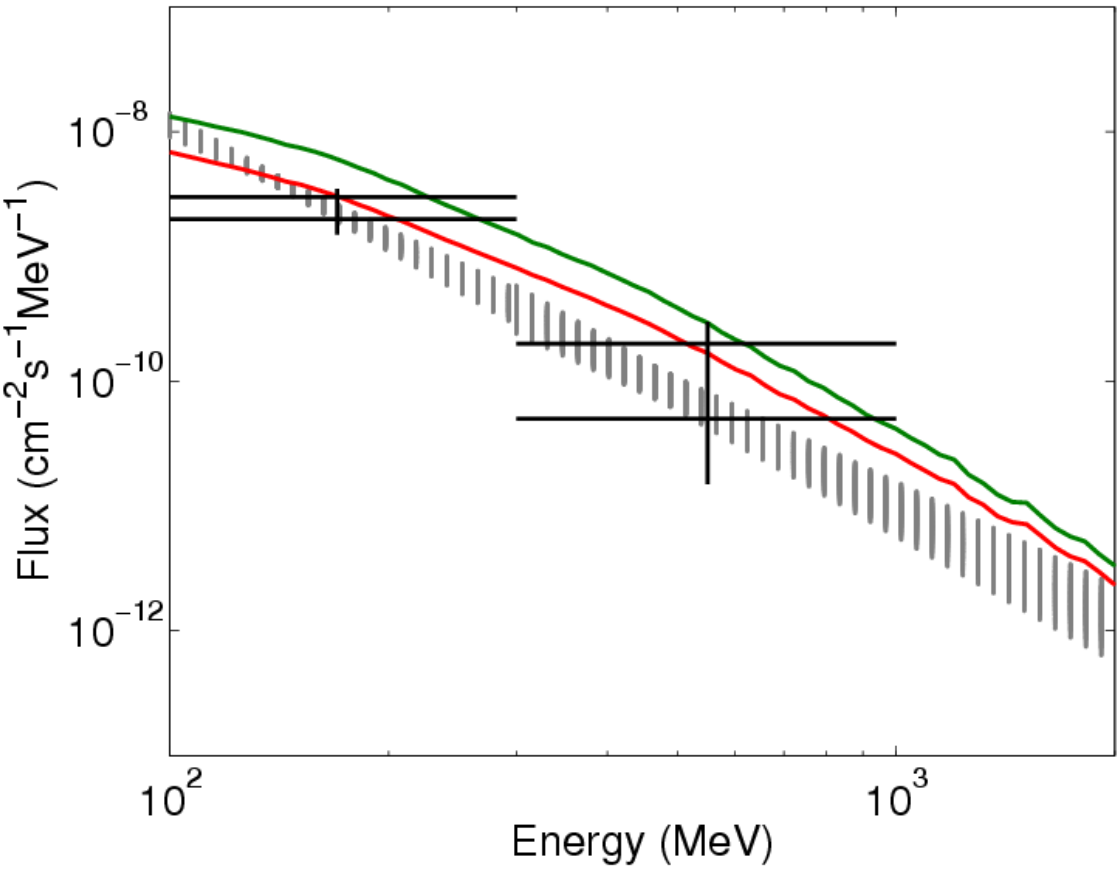

Figure 3.12: Spectrum of the moon obtained by the fitting analysis of the EGRET data between October '91 to June '95 (dashed region). Thickness of the line shows the error bars. Black bars are obtained by Thompson et al. (1997) for different solar conditions, while lines are the theoretical model of Moskalenko & Porter (2007), for solar maximum (red line) and solar minimum (green line).

the likelihood is maximized over the other components. The analysis was performed for four different estimates of the solar modulation.

For the different models of solar modulation, the expected values of inverse Compton emission are in agreement with the data within 1σ, with rather big errors bars. This also means that, because of the limited sensitivity of EGRET, it is not possible to say which model better describes the data. We found probabilities corresponding to 2.7, 3.6/4 and 1σ above 100 MeV, above 300 MeV (including/excluding J2321-0328) and for 100-300 MeV respectively for the significance of the detection. However, we chose the naive model of 1000 MV solar modulation in order to derive the spectra of the extended and

Table 3.3: Results for different energy ranges and for the naive model of 1000 MV solar modulation. Fluxes are given in $cm^{-2}s^{-1}$ and intensities in $cm^{-2}s^{-1}sr^{-1}$. For details see text.

Model		>100 MeV	>300 MeV with J2321-0328	>300 MeV no J2321-0328	100-300 MeV
Source flux	best fit	$4.68^{+4.17}_{-3.82} \times 10^{-8}$	$3.38^{+1.80}_{-1.81} \times 10^{-8}$	$3.38^{+1.88}_{-1.84} \times 10^{-8}$	14.04×10^{-8}
	mean	$(5.42 \pm 3.20) \times 10^{-8}$	$(3.03 \pm 1.10) \times 10^{-8}$	$(3.65 \pm 1.71) \times 10^{-8}$	$(14.2 \pm 9.1) \times 10^{-8}$
	counts	28	20	20	39
Extended flux	best fit	$3.83^{+2.78}_{-2.80} \times 10^{-7}$	$1.54^{+1.06}_{-1.18} \times 10^{-7}$	$1.75^{+1.08}_{-1.13} \times 10^{-7}$	1.15×10^{-7}
	mean	$(3.89 \pm 2.16) \times 10^{-7}$	$(1.49 \pm 0.67) \times 10^{-7}$	$(1.70 \pm 0.87) \times 10^{-7}$	$(2.07 \pm 1.34) \times 10^{-7}$
	counts	273	116	132	83
Extended solar model	flux	2.18×10^{-7}	0.90×10^{-7}	0.90×10^{-7}	1.28×10^{-7}
Background	intensity	3.50×10^{-5}	1.13×10^{-5}	1.12×10^{-5}	2.48×10^{-5}
	counts	2220	750	741	1603
3C279	flux	4.88×10^{-7}	1.30×10^{-7}	1.30×10^{-7}	5.85×10^{-7}
	counts	103	29	29	79
Prob. (flux=0)		6.4×10^{-3}	2.3×10^{-4}	9.7×10^{-5}	0.24
Strongest bkg source	flux	3.82×10^{-7}	1.28×10^{-7}	0.63×10^{-7}	2.54×10^{-7}
Total bkg sources	counts	113	27	21	66
Moon	flux	5.55×10^{-7}	0.57×10^{-7}	0.57×10^{-7}	4.98×10^{-7}
	counts	37	4	4	29

disk emission. This is for two reasons: first this model produces the highest value of the likelihood; second it should be the most realistic for the period '91-'95, since the data cover the total period of solar maximum and the upcoming solar minimum. *Hence, we report only the results for the naive case of 1000 MV solar modulation.* We used both frequentist and Bayesian approaches to analyze the results. The statistical methods are described in the appendix.

Values of the best fit fluxes, 1σ errors, counts and mean values with errors are given in Table 3.3. Best fit values are calculated from the log-likelihood ratio statistic, while mean values are from the Bayesian method. Counts are for the maximum likelihood values, as are the background, the 3C279 fluxes and the probability of the null hypothesis. Values in the first column were used to have more statistics for detection, while separate energies are best for the analysis. For 100-300 MeV range error bars cannot be determined by the frequentist method. We also give the probability of the null hypothesis (i.e. zero flux from disk and extended emission) using the likelihood ratio statistic. The table contains two cases above 300 MeV with different fluxes of the background sources. The first is obtained including the source J2321-0328 whose spectral index was fixed at a typical value of 2, since it is not given in the 3EG catalogue. The second case does not include that source, since it has not been detected at energy above 300 MeV. I took the second case for the following analysis. These two cases give also an estimate of the uncertainty of our results.

The log-likelihood ratio for the three energy ranges I analyzed are displayed in Fig.3.14 as a function of solar disk flux and extended flux. Colors show different values of the ratio, obtained by allowing the background and the QSO 3C279 component to vary to maximize the likelihood for each value of disk flux and extended component, while contour lines define 1, 2 and 3σ confidence intervals for the two separate parameters. Marginal probabilities of the two components calculated with the Bayesian method and cumulative probability as function of the disk and extended fluxes are shown in Fig. 3.15. The sum of the two components, disk and extended, is given in Table 3.4. Counts of the source components centred on the Sun resulting from the fitting technique above 300 MeV are shown in Fig.3.16. A summary of the main results is given in Table 3.5. The solar disk spectral index we found is $2.4^{+0.9}_{-0.8}$. Errors are calculated from the uncertainties on the integrated fluxes. Figure (3.17) shows the solar disk spectrum obtained imposing a constant spectral index of 2.4, its mean value, and following a simple power law up to 2 GeV.

Table 3.4: *Sum* of disk and extended components of solar emission for different energies. Values are from the Bayesian method.

Energy (MeV)	Total flux (10^{-7} cm^{-2}s^{-1})
> 100	(4.44±2.03)
> 300	(2.07±0.79)
$100 - 300$	(3.49±1.35)

Table 3.5: Fluxes used to produce the plotted solar spectra. Fluxes are in 10^{-7} cm^{-2}s^{-1}

Source	100-300 MeV	>300MeV
Extended	2.1±1.3	1.7±0.9
Model extended	1.3	0.9
Disk	1.4±0.9	0.4±0.2
Seckel's disk model	0-1.1	0.1-0.5

For the extended emission, we found a spectral index of $1.7^{+0.8}_{-0.5}$. The extended spectrum is shown in Fig. (3.18). As for the disk spectrum, the spectral index has been fixed at the mean value. The spectrum is compared with the modelled spectrum for "naive" cases of 500 MV and 1000 MV solar modulation.

3.7 Tests of analysis procedure

In order to perform a test of the solar detection, we divided the total exposure which we used for the analysis described above, into two periods with about the same exposure time. Then, we analyzed the data with the same fitting technique explained above. Both these time periods contain about 3.6×10^8 cm^{2}s of exposure on the Sun. Assuming equal periods and a constant flux from the Sun, the two periods should give compatible fit results. As an example, the analysis was performed above 300 MeV, where the detection was most significant and for the naive case and solar modulation 1000 MV. The first period contains only 3C279, J1409-0745 and the moon, while in the second one there are only the other background sources and the moon; 3C279 is not present. Figure (3.19) shows the count maps of the two different periods. The likelihoods are shown in Fig. (3.20).

The values obtained for the different emission components for first and second period are consistent within 1σ and are listed in Table 3.6. Moreover,

Table 3.6: Results for two observation periods (see text) above 300 MeV and for the naive case of 1000 MV modulation. For explanation see Table 3.3

		First period	Second period
Source flux	best fit	$2.02^{+2.92}_{-2.02} \times 10^{-8}$	$3.97^{+2.82}_{-2.28} \times 10^{-8}$
	mean	$(3.42 \pm 2.13) \times 10^{-8}$	$(4.37 \pm 2.03) \times 10^{-8}$
	counts	6	11
Extended flux	best fit	$2.92^{+1.64}_{-2.08} \times 10^{-7}$	$1.06^{+1.32}_{-1.06} \times 10^{-7}$
	mean	$(2.46 \pm 1.13) \times 10^{-7}$	$(1.21 \pm 0.71) \times 10^{-7}$
	counts	107	38
Model flux		0.90×10^{-7}	0.90×10^{-7}
Total flux		$(2.80 \pm 1.07) \times 10^{-7}$	$(1.64 \pm 0.66) \times 10^{-7}$
Background	intensity	1.24×10^{-5}	0.94×10^{-5}
	counts	408	297
3C279	flux	1.78×10^{-7}	-
	counts	40	-
Prob. (flux=0)		10^{-2}	6.6×10^{-4}

they are also in agreement with those obtained for the total period. This confirms the validity of our method and the solar detection.

In order to exclude possible contamination of some faint solar flares detected by CGRO/COMPTEL during the same period, we performed the fitting method also with solar flares times excluded. Values will not be reported since, as expected, I did not find any change in the results.

3.8 Discussion

For the extended solar emission, Fig. (3.18) shows that my model is fully consistent with the measured spectrum. The main uncertainty in the model is the electron spectrum (the solar radiation field and the physics of the inverse Compton are precisely known). The electron spectrum at the relevant energies has about a factor 2 experimental uncertainty. In fact the measured extended fluxes are higher by a factor $\sim$2 (although not very significant) which suggests our electron spectrum could be too low.

Regarding the solar disk flux, the flux in all cases is in agreement with the theoretical value for pion-decay obtained by Seckel et al. (1991). The Galactic background obtained with the fitting technique is compatible with

the expected Galactic emission (GALPROP) (Strong et al. 2004b). The flux of 3C 279 of 7.2 $\times 10^{-7} cm^{-2} s^{-1}$, sum of the flux for 100-300 MeV and above 300 MeV, is in agreement with the EGRET catalogue. In the catalogue for period 11 used for this analysis the flux is $(7.94 \pm 0.75) \times 10^{-7} cm^{-2} s^{-1}$ above 100 MeV, while for period 12 (the other viewing period used in the analysis) there is hardly any contribution.

With respect to the analysis of EGRET data performed by Thompson et al. (1997), our study has some improvements which explain why we succeeded in detection, while they did not. Instead of excluding data near the sources 3C279 and the moon, they are included in our analysis. This leads to more exposure using contributions from all observing periods. The special dedicated analysis software for moving targets and the inclusion of the extended emission from the Sun produced a more realistic prediction of the total data and hence a more sensitive analysis.

3.9 Conclusions

The theory of gamma-ray emission from IC scattering of the solar radiation field by Galactic CR electrons has been given in detail. Analyzing the EGRET database, we find evidence for emission from the Sun and its vicinity. For all models the expected values are in good agreement with the data, with rather big errors bars. This also means that, because of the limited sensitivity of EGRET, it is not possible to prove which model better describes the data. The spectrum of the moon has also been derived.

Since the inverse Compton emission from the heliosphere is extended, it contributes to the whole sky foreground and has to be taken into account for diffuse background studies. Moreover, since the emission depends on the electron spectrum and its modulation in the heliosphere, observations in different directions from the Sun can be used to determine the electron spectrum at different position, even very close to the Sun. To distinguish the modulation models (eg. with GLAST) an accuracy of $\sim$10% would be required. With the point source sensitivity of GLAST around $10^{-7}\mathrm{cm}^{-2}\mathrm{s}^{-1}$ per day above 100 MeV, it will be possible to detect daily this emission, when the Sun is not close to the Galactic plane. In addition a precise model of the extended emission, such as that presented here, would be required in for dark matter searches.

3.10 Perspectives for GLAST

Some estimates for GLAST perspectives to detect the extended solar emission were made. In the most optimistic case, that is for Sun-pointing mode and for solar minimum when the extended emission is maximum, in 10 deg^2 centred on the Sun and above 100 MeV, we expect around 70 counts for this emission and background around 200 counts per day. This means that every day we can have 4σ detection. For scanning mode, to have 4σ detection we have to wait about two weeks. Better detections are at higher energies, since, far away from the Galactic plane the EGB dominates, the Galactic emission drop off and the effective area of the telescope increases. To distinguish between different models of solar modulation, we have to reach an accuracy of 10%, and thus integrate for at least 25 days for Sun-pointing mode or 5 months for scanning mode. Resolving the angular profile with steps of 1° above 1 GeV at 5° we need 8 months data for 3σ taking all events, while to resolve it up to 10° around 3 year for 3σ (all events). The analysis with GLAST will be performed considering the emission from decay of pion produced by of cosmic-ray protons on the solar surface and from the extended inverse-Compton emission by scattering of cosmic-ray electrons on the solar photon field.
This study of the solar emission with GLAST is the only way to probe the modulation of cosmic-ray electrons in the near proximity of the Sun. Since the solar inverse-Compton emission depends on the electron spectrum and its modulation within the heliosphere, observations in different directions from the Sun can be used to determine the electron spectrum of cosmic rays at different position, even very close to the Sun. The determination of the cosmic-ray spectrum is important also for models of the gamma-ray diffuse emission, again helping to test models of the Galactic diffuse emission. Moreover above 100 MeV the all sky average solar emission is about 10% of the extragalactic emission, and hence is also important for studies on Dark Matter. In contrast to the EGRET analysis, with the GLAST sensitivity it will be possible to perform this in Galactic coordinates and including time resolution to follow the time variation of other sources coming close to the Sun, avoiding the Galactic plane and modelling the diffuse Galactic emission with GALPROP (Strong & Moskalenko 1998).

———————————————-

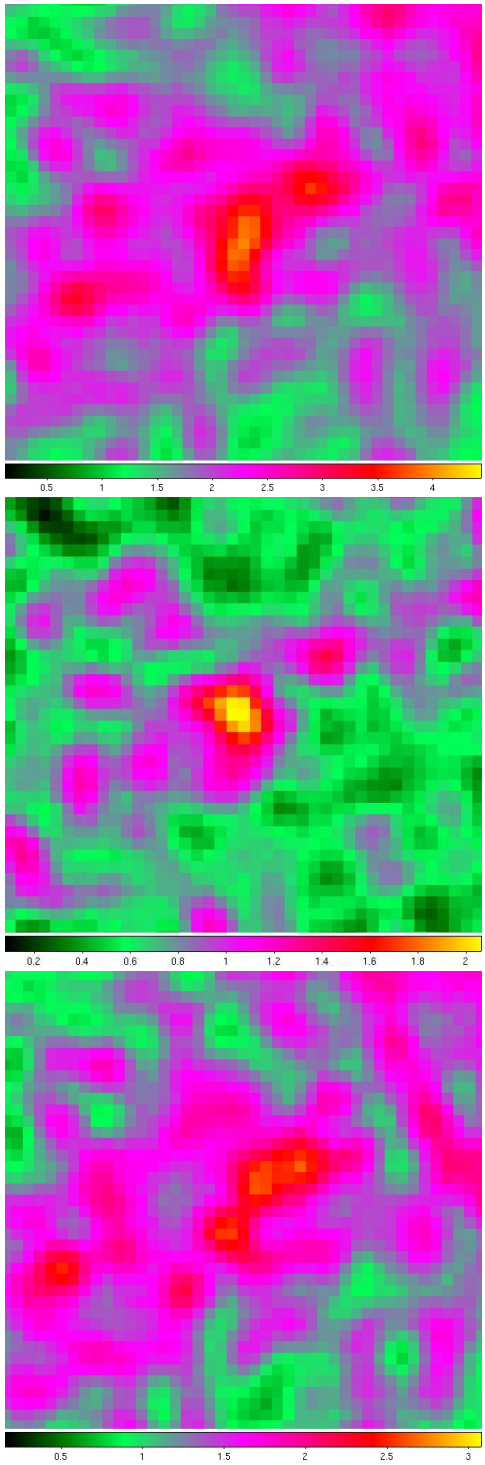

Figure 3.13: EGRET Sun-centred counts maps (top to bottom)>100 MeV, >300 MeV and 100-300 MeV. The colorbar shows the counts per pixel. The area is 20° on a side and the maps are Gaussian smoothed to 3° (Orlando & Strong 2008).

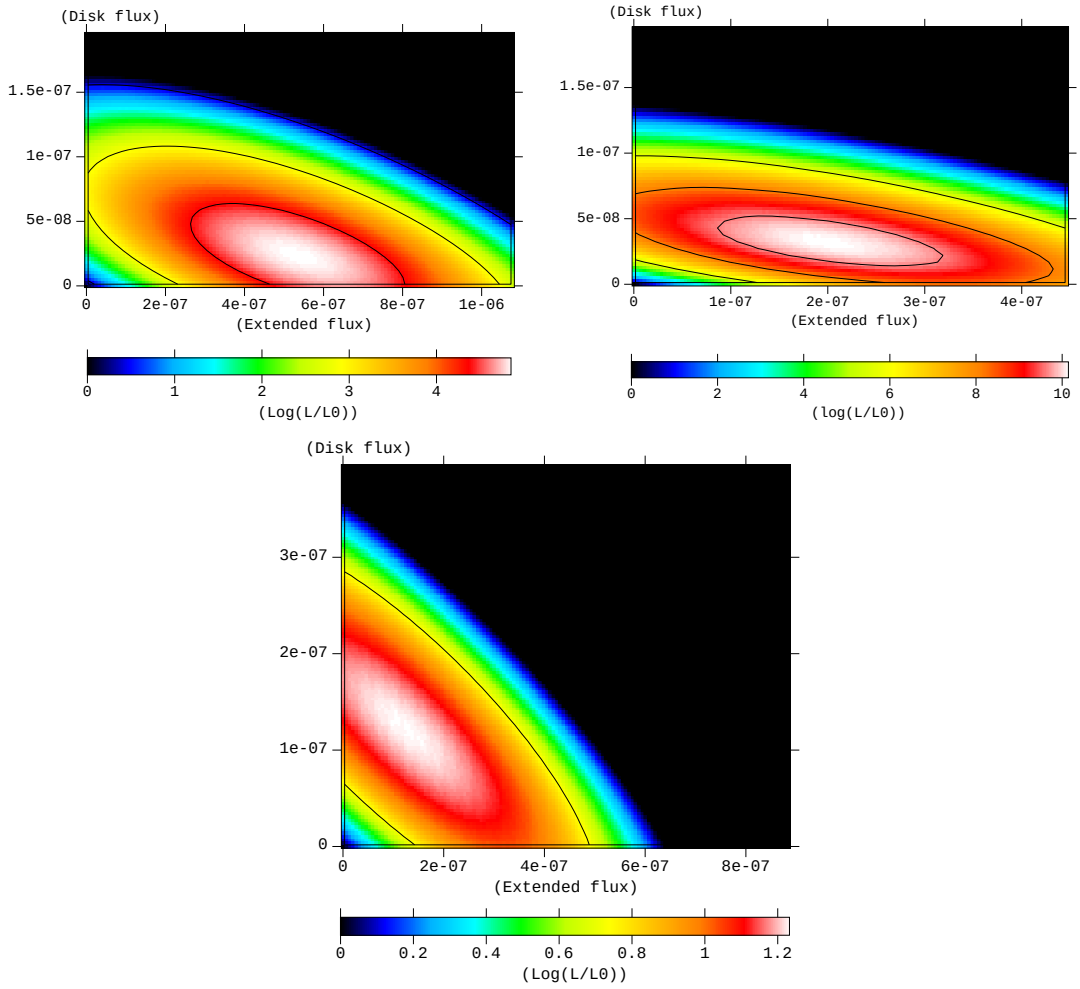

Figure 3.14: Logarithm of the likelihood ratio (ln (L/L_0)) as a function of the solar disk flux and an extended component for (top to bottom) >100 MeV, >300 MeV and 100-300 MeV . Color contours are different values of the ratio, as explained in the colorbar. Contours are obtained by allowing the background and the QSO 3C279 component to vary to maximize the likelihood for each value of disk flux and extended component. Contour lines define 1, 2 and 3σ intervals for the 2 separate parameters (Orlando & Strong 2008).

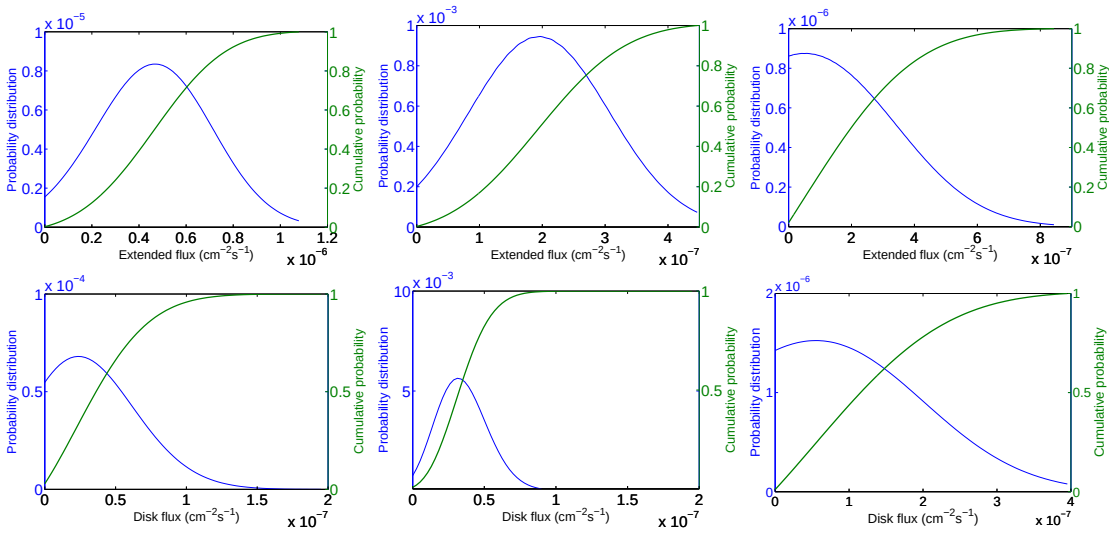

Figure 3.15: Marginal probability of the two components calculated from eq.3.10 and cumulative probability as function of the extended (upper panel) and disk (lower panel) fluxes for different energy ranges, (left to right) above 100 MeV, above 300 MeV and for 100-300 MeV

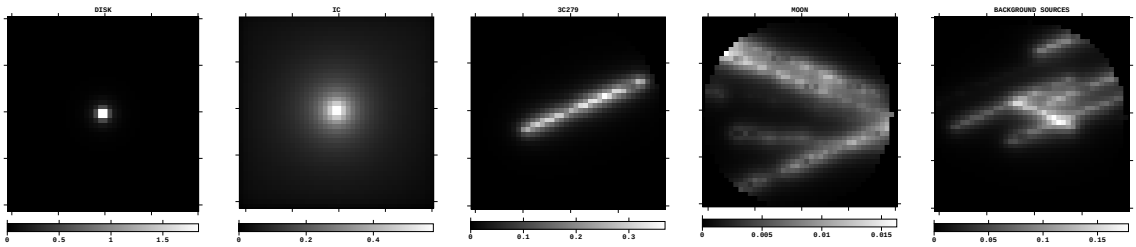

Figure 3.16: Counts of the source components resulting from the fitting technique above 300 MeV. Left to right: solar disk, inverse Compton, QSO 3C279, moon and background sources. Colorbars show counts per pixel.

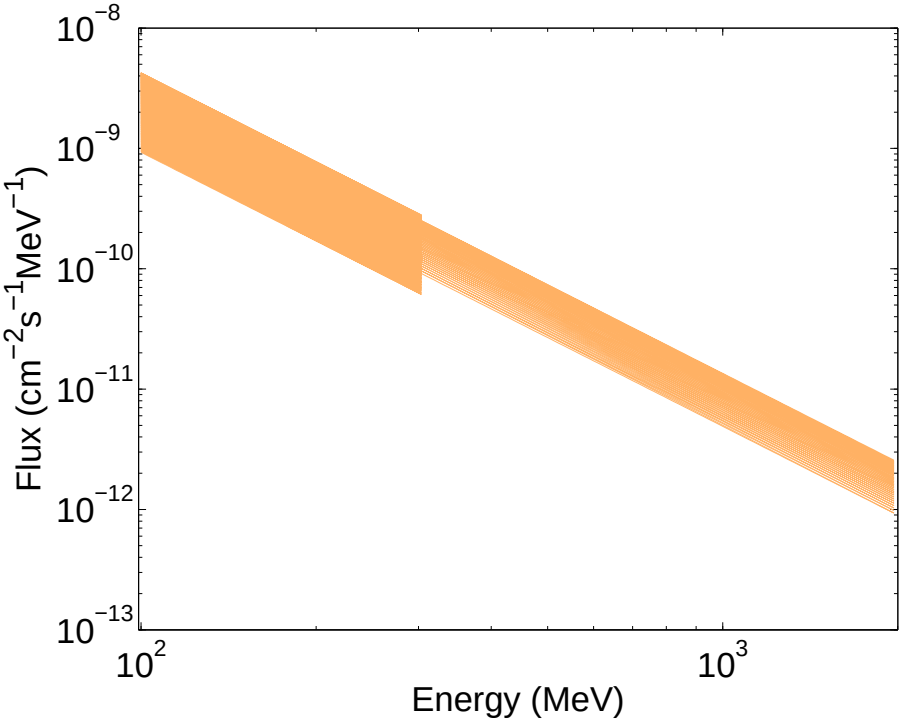

Figure 3.17: Solar disk spectrum. The orange regions defines the possible values obtained by varying the mean flux within 1σ errors and for γ=2.4, the mean value of the spectral index.

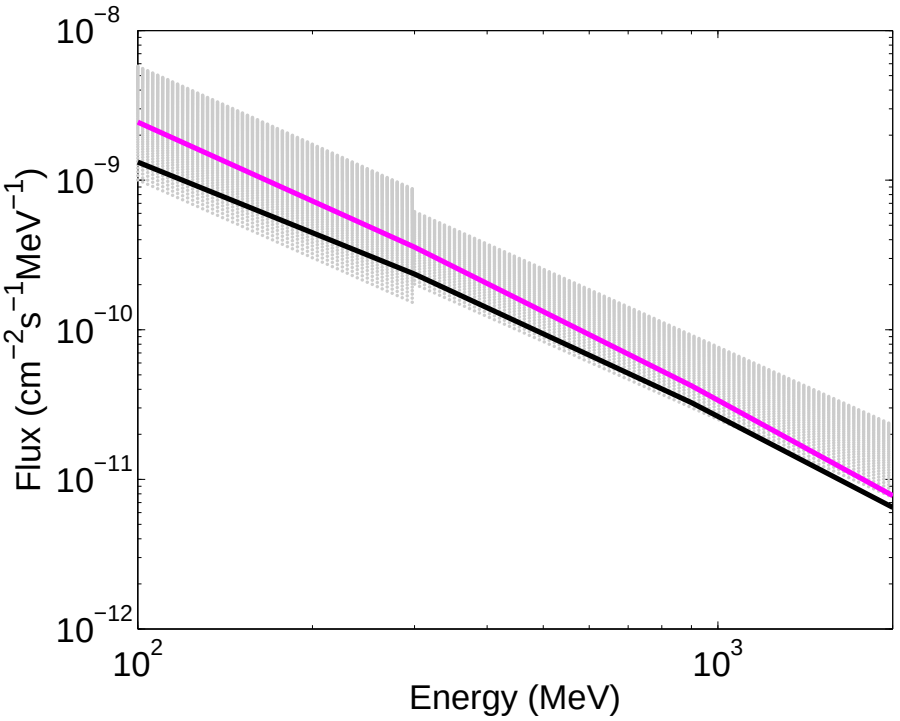

Figure 3.18: Solar extended spectrum. Gray regions define the possible values obtained by varying the mean flux within 1σ errors and for γ=1.7, the mean value of the spectral index. Black line is the model for the naive case of 1000 MV modulation. For comparison, the pink line shows the model for the naive case of 500 MV modulation.

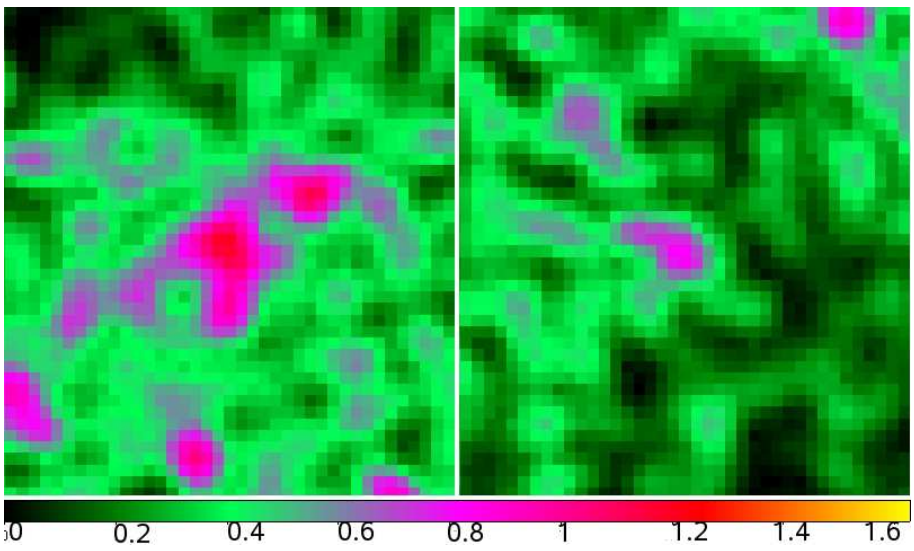

Figure 3.19: Counts maps Sun centred for period 1 (left) and period 2 (right). The colorbar shows the counts per pixel. The area is 20 degrees side.

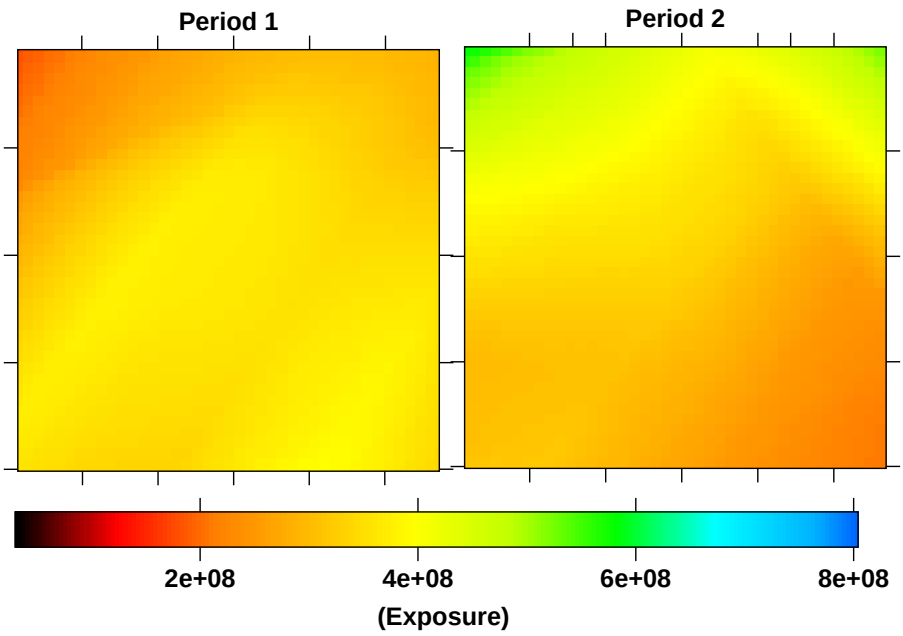

Figure 3.20: Exposure maps Sun centred for period 1 (left) and period 2 (right). The colorbar shows the exposure ($cm^{-2}s^{-1}$). The area is 20 degrees side.

Chapter 4

Gamma-ray and synchrotron emission from the Galaxy: a multi-wavelength approach to constrain CR electrons

4.1 Introduction

Since Galactic cosmic ray electrons, gamma rays and synchrotron radiation are closely related topics, a parallel study of both synchrotron and gamma-rays, and the tuning of the parameters to match these spectra can help in understanding the distribution of cosmic-ray electrons in the Galaxy and the Galactic magnetic field. After a brief introduction of the GALPROP code (Strong & Moskalenko 1998) used to perform this study, this chapter is divided in these two related topics: the last results of soft gamma-ray and synchrotron emission from the Galaxy.

4.2 GALPROP code overview

The GALPROP code (Strong & Moskalenko 1998) was created in order to have simultaneous predictions of CR nuclei, electrons and positrons, γ-rays and synchrotron radiation. For details we refer the reader to the relevant papers (Strong et al. 2000, 2004b; Moskalenko & Strong 1998, 2000; Moskalenko et

al. 2002; Strong & Moskalenko 1998; Ptuskin et al. 2006) and the website[1]; below an overview of the code is given. The GALPROP code solves the CR transport equation with a given source distribution and boundary conditions for all CR species. The formulation includes galactic wind (convection), diffusive reacceleration in the interstellar medium, energy losses, nuclear fragmentation, radioactive decay, and production of secondary particles and isotopes as illustrated n the Introduction. The spatial boundary conditions are that free particle escape. The grid involves a 3D (R, z, p) or 4D (x, y, z, p) problem, i.e. spatial variables plus momentum. For a given halo size the diffusion coefficient, as a function of momentum and the reacceleration or convection parameters, is determined by the boron-to-carbon ratio data. If reacceleration is included, the momentum-space diffusion coefficient D_{pp} is related to the spatial coefficient D_{xx} ($D_{pp}D_{xx}$ = p^2) γ-ray emission is calculated using the propagated CR distributions, including secondary particles such as positrons and electrons from inelastic processes in the interstellar medium. γ-rays related to the gas distribution are computed as a function of (R, z, E_γ) using the column densities of H I and H_2 for galactocentric annuli based on 21-cm and CO surveys included in the GALPROP model.

GALPROP starts solving the propagation equation first from the heaviest primary nucleus (e.g. ^{64}Ni) finding the spallation products, which are then propagated in turn, down to protons, secondary electrons and positrons, and antiprotons. Normalisation of protons, alphas, and electrons to experimental data is provided and all other isotopes are determined by the source composition and propagation. Gamma rays are estimated using interstellar gas data for π^0-decay and bremsstrahlung and the interstellar radiation field (ISRF) model for inverse Compton emission. The synchrotron emission is determined using the Galactic magnetic field model. Spectra of all species and the γ-ray and synchrotron skymaps are compared with data. The CR source distribution is based on the Galactic pulsar distribution (Lorimer 2004), while the factor $X_{\rm CO} = N({\rm H}_2)/W_{\rm CO}$, is variable, increasing towards the outer Galaxy, and fully compatible with the expected variations based on the metallicity gradient and COBE data (Strong et al. 2004c). The GALPROP code reproduces the diffuse Galactic γ-ray emission for the whole sky as well as the radial gradient of diffuse Galactic γ-ray emissivity. The ISRF is the result of emission by stars, and the scattering, absorption, and re-emission of absorbed starlight by dust in the interstellar medium (ISM). The Strong et al. (2000) ISRF

[1] `http://galprop.stanford.edu`

model includes spatial and wavelength dependence over the whole Galaxy, using emissivities based on stellar populations based on COBE/DIRBE fits by Freudenreich (1998) and the SKY model of Wainscoat et al. (1992) together with COBE/DIRBE derived infrared emissivities (Sodroski et al. 1997; Dwek et al. 1997). Subsequent to this work new relevant astronomical information on stellar populations, Galactic structure, and interstellar dust has become available, motivating a re-evaluation of the ISRF. The fundamental factors influencing the ISRF are the luminosity distribution from the stellar populations of the Galaxy and the radiative transport of the star light through the ISM. The interstellar dust absorbs and scatters the star light in the ultraviolet (UV) and optical, and re-emits the absorbed radiation in the infrared. The calculations of the ISRF is explained in detail in Porter et al. (2008).

Figure 4.1 shows the spectral energy distributions (SEDs) in the Galactic plane for different galactocentric radii for the case of maximal metallicity gradient and for no metallicity gradient. Increasing metallicity gradient reduces the UV in the inner Galaxy by up to a factor of 3 for $\lambda \leq 0.3$ μm – which is redistributed into the infrared. The infrared emission for the inner Galaxy for the maximum metallicity gradient is a factor of ~ 2 higher than for the case of no metallicity gradient. For the outer Galaxy the ISRFs calculated for the two cases differ less dramatically. For the case of the maximal metallicity gradient the UV emission is higher than the no gradient case because there is less dust in the outer Galaxy. In turn, this results in less emission in the infrared than for the maximal gradient case (Porter et al. 2008).

4.3 Gamma-ray emission from the Galactic center

In this Section the diffuse Galactic gamma-ray emission and the propagation of cosmic rays in the Galaxy are investigated using the INTEGRAL data and the GALPROP code described above. The soft gamma ray emission from the Galactic ridge seen by INTEGRAL is shown to be well reproduced by inverse Compton emission by scattering of GeV cosmic-ray electrons on the interstellar radiation field. Both cosmic-ray primary electrons and secondary electrons and positrons contribute to the emission. The prediction uses the GALPROP model and includes a new calculation of the interstellar radiation field (Porter et al. 2008). This may solve a long-standing mystery of the origin of this emis-

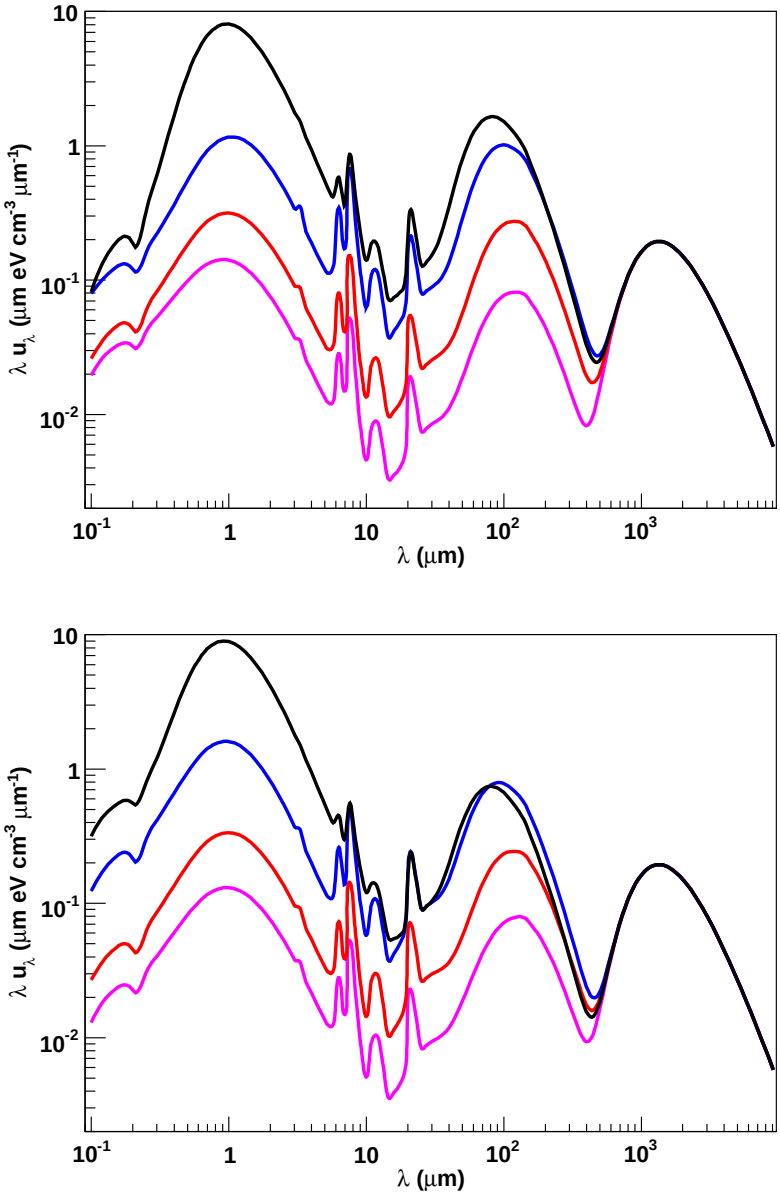

Figure 4.1: Spectral energy distribution of the MW ISRF in the Galactic plane. Line colouring: black, $R = 0$ kpc; blue, $R = 4$ kpc; red, $R = 8$ kpc; magenta, $R = 12$ kpc. *Top:* maximum metallicity gradient; *Bottom:*, minimum metallicity gradient. The cosmic microwave background (CMB) is included in both figures and dominates the SED for wavelengths $\lambda > 600$ μm.

sion, and potentially opens a new window on Galactic cosmic rays. The predictions have also been extended to lower energy and compared with the present hard X-ray data of the extra-galactic background.

4.3.1 Some history

The Galactic ridge is a source of continuum hard X- and γ-ray emission. In 1972 the hard X-ray emission was discovered (Bleach et al. 1972), and interstellar emission has been then observed by HEAO-1, Tenma (ASTRO-B), ASCA, Ginga, RXTE, OSSE (Worrall et al. 1982; Koyama et al. 1986; Purcell et al. 1996; Kinzer et al. 1999, 2001), and by Chandra and XMM-Newton. The γ-ray observations started with the OSO-III satellite in 1968, followed by SAS-2 in 1972, COS-B (1975–1982) and COMPTEL and EGRET on the CGRO (1991–2000). The Galactic diffuse emission is an important study for INTEGRAL (in orbit since 2002) and the GLAST LAT (launched in June 2008) (Michelson 2007; Ritz 2007).

Diffuse continuum emission is expected in the hard X-ray and γ-ray range from the positron annihilation, through intermediate formation of positronium, by inverse-Compton scattering and bremsstrahlung from cosmic-ray (CR) electrons and positrons, and via decay of neutral pions produced by interactions of CR nuclei with the interstellar gas. Positron annihilation in flight (continuum) may contribute in the few MeV range (Beacom & Yüksel 2006). For the non-positronium continuum, hard X-rays from bremsstrahlung emission imply a luminosity in CR electrons much large (see e.g. Dogiel et al. 2002a). At MeV energies the origin of the emission is also unknown (Strong et al. 2000).

The origin of the emission form the Galactic ridge could be attributed to a population of sources too weak to be detected. In general, γ-ray telescopes have inadequate spatial resolution to clarify this issue. In X-rays (2–10 keV), high-resolution imaging with Chandra (Ebisawa et al. 2001, 2006) has claimed to prove the existence of a truly diffuse component. Similarly, it has been claimed from an analysis of XMM-Newton data (Hands et al. 2004) that 80% of the Galactic-ridge X-ray emission is probably diffuse, and only 9% can be accounted for by Galactic sources, the rest being extragalactic in nature. More recently Revnivtsev et al. (2006), with RXTE PCA data, and Krivonos et al. (2007), using INTEGRAL/IBIS and RXTE data, argue that below 50 keV all the diffuse emission can be accounted for by a Galactic popu-

lation of sources, mainly magnetic cataclysmic variables; see also Revnivtsev & Sazonov (2007) and Revnivtsev et al. (2007).

Above MeV energies, a detailed study of the diffuse Galactic γ-ray emission has been made by Strong et al. (2004b, 2000). This study confirmed that models based on locally measured electron and nuclei spectra and synchrotron constraints are consistent with γ-ray measurements in the (30 - 500) MeV range; outside this range deviations from the data are significant.

Above 1 GeV there is an excess in the EGRET diffuse emission data with respect to that expected (Strong et al. 2000; Hunter et al. 1997) form models tuned to be consistent with the locally measured CR nuclei and electron spectra (Moskalenko et al. 2004; Strong et al. 2004b). The GeV excess is present in all directions

Hence, assuming that the GeV excess is not instrumental, the optimised model was proposed in Strong et al. (2004b) to explain it in terms of CR intensity variations in the Galaxy. This CR spectrum reproduces the diffuse γ-rays in *all directions*, as well as the latitude and longitude profiles for the whole EGRET energy range 30 MeV - 50 GeV

The high spectral resolution of INTEGRAL combined with its imaging capabilities promises new view into the nature of this emission. Previous work based on initial, smaller sets of INTEGRAL/SPI observations have reported the detection of diffuse emission (Strong et al. 2003; Strong 2003). However, statistical and systematic errors were large, due in part to the uncertainty in the point-source contribution.

Lebrun et al. (2004); Terrier et al. (2004) performed a new analysis of INTEGRAL/IBIS data and showed that, up to 100 keV, a large fraction of the total emission from the inner Galaxy is produced by sources. Strong et al. (2004b) used the source catalogue from this work containing 91 sources as input to SPI model fitting, giving a more solid basis for the contribution of point sources in such an analysis. The SPI analysis by Bouchet et al. (2005) gave a rather lower 50-1000 keV power-law continuum than Strong et al. (2005), but the errors were large in the early datasets. Recently, a new analysis by Bouchet et al. (2008) with 3 times as much SPI exposure gives better statistics, background handling, and point-source subtraction.

In this Section we focus on energies above 50 keV where sources are not important because of the rapid cut-off in the spectra of the most, and the relatively small number of hard-spectrum sources. We use the GALPROP model and the model for the Galactic interstellar radiation field (ISRF) by

Porter et al. (2008) to explain the origin of the hard X-ray emission and to build a model of the Galactic diffuse emission (GALPROP) in the energy range from keV to TeV energies.

4.3.2 Diffuse emission with GALPROP

Primary CR electrons are directly accelerated in CR sources like supernova remnants or pulsars. Secondary electrons and positrons are produced via interactions of energetic nuclei with interstellar gas, and are usually considered a minor component of CRs. This happens in the heliosphere where the positron to electron ratio is small at all energies, $e^+/(e^+ + e^-)_{tot} \sim 0.1$. However, the combined secondary electron/positron flux in the interstellar medium is more than half of the primary CR electron flux at $\sim$1 GeV energies and below. This gives an important contribution of secondary positrons and electrons to the diffuse γ-ray flux via IC scattering and bremsstrahlung and increases the flux of diffuse Galactic emission below $\sim$100 MeV up to a factor of $\sim$2. Hence, econdary positrons and electrons are directly seen in hard X-rays and γ-rays. The primary electron and secondary positron and electron spectra from the GALPROP propagation calculations are shown in Figure 4.2. For energies ≤ 1 GeV, the secondary positron and electron flux in the ISM is higher than the primary electron flux. The addition of the secondary electrons and positrons increases by ~ 2.5 the total number capable of producing γ-rays via IC scattering relative to the pure primary electrons.

We compare our results for the diffuse emission in the Galactic ridge with the new SPI data from Bouchet et al. (2008), and COMPTEL and EGRET data. The spectrum for each instrument is obtained by integrating over deconvolved skymaps. The procedure used to obtain the diffuse emission is briefly described below (for details see Bouchet et al. (2008)). In the method of Bouchet et al. (2008), a source catalogue is constructed using an iterative algorithm taking into account variable source flux contributions using templates for the spatial morphologies of the interstellar emission: 8° degree Gaussian for the positron annihilation emission, DIRBE 4.9 μm and CO maps for the continuum below and above 120 keV, respectively. The normalisation factor for each of these maps is adjusted during the fitting procedure. The source position information is used in the next step of the analysis where the region $|l| \leq 100^\circ$ and $|b| \leq 30^\circ$ is divided into cells with sizes that are chosen to optimise the signal-to-noise ratio per cell, while still being sufficiently small to

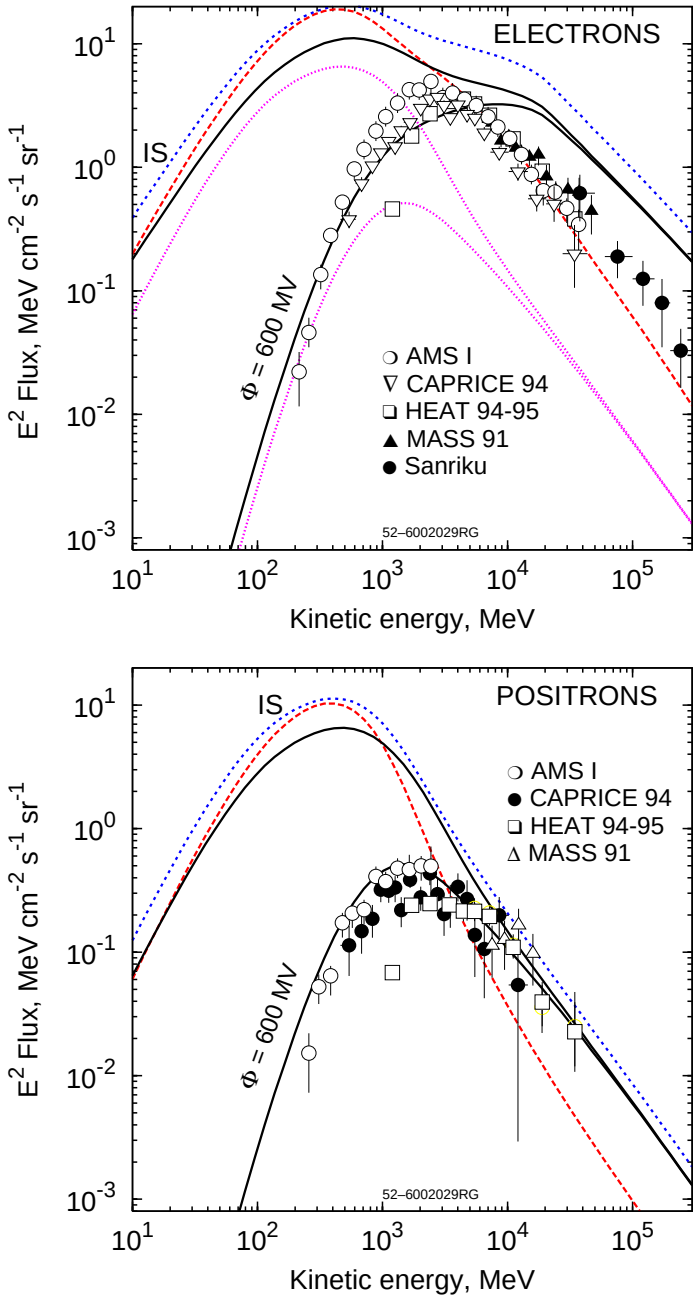

Figure 4.2: Spectra of CR electrons and positrons in the Galactic plane, as predicted by the adopted optimised GALPROP model. *Top:* Total (primary + secondary) and secondary electrons; *Bottom:* Secondary positrons. Interstellar spectra (IS): $R = 0$ kpc (red long dashes), $R = 4$ kpc (blue short dashes), $R = 8.5$ kpc (black solid), also shown modulated to 600 MV. Secondary electrons are shown separately as magenta lines (IS and modulated) on the left panel at $R = 8.5$ kpc. See Porter et al. (2008) for reference on the data from various experiments

follow the observed spatial variations (around 5 $\circ$). A likelihood fit is done using the a-priori source position information to obtain the source fluxes and diffuse emission for each 'pixel' cell over the energy ranges 25-50, 50-100, 100-200, 200-600, 600-1800, and 1800-7800 keV, respectively. This model independent "image-based" method establishes the extent of the diffuse emission. To extract the diffuse spectrum with better signal-to-noise, the background templates (DIRBE 4.9 μm, CO) are also fit for each energy range. The power-law continuum is based on this model-dependent method but there is some error associated. To estimate the errors the integrated latitude profiles obtained using the image-based method described above and the fit results for the background template maps were compared in Porter et al. (2008). Based on this comparison the diffuse intensities could be up to 40% higher than those in Bouchet et al. (2008).

Figure 4.3 shows the individual contributions by primary electrons to the diffuse Galactic emission, while Fig. 4.4 the contribution of secondary electrons and positrons For primary electrons, the agreement with the SPI data is excellent while there is still some deficit when compared with COMPTEL. For secondary electrons and positrons, the spectrum of γ-rays is steeper below ~ 10 MeV compared to the primary electrons, which is a reflection of the different source spectra: the primary electron source spectrum is found from adjusting to the γ-ray spectrum at higher energies, while the secondary electron/positron source spectrum follows from the CR nucleon spectrum in the ISM.

Figure 4.3 and Figure 4.4 plot also the components of the IC emission. For primary electrons, the scattering of optical photons is the major contribution in the energy range ~ 50 MeV–100 GeV, and the infrared the major component below ~ 50 MeV and above 100 GeV, and the Cosmic Microwave Background (CMB) comparable to the infrared below $\sim$ 500 keV. For the secondary electrons/positrons the scattering of the optical component dominates above ~ 500 keV, while the infrared is the major component for energies below this. Thus, the primary and secondary populations IC scatter the components of the ISRF to different hard X-ray/γ-ray ranges. Interestingly, for secondary electrons/positrons the bremsstrahlung contribution is a factor ~ 2 higher for 100 MeV to 1 GeV than the primary electron case.

In Figure 4.5 we show the diffuse emission calculated using the optimised model with an ISRF calculated with a maximal metallicity gradient. Inverse Compton scattering is a major component at all energies, with π^0-decay more

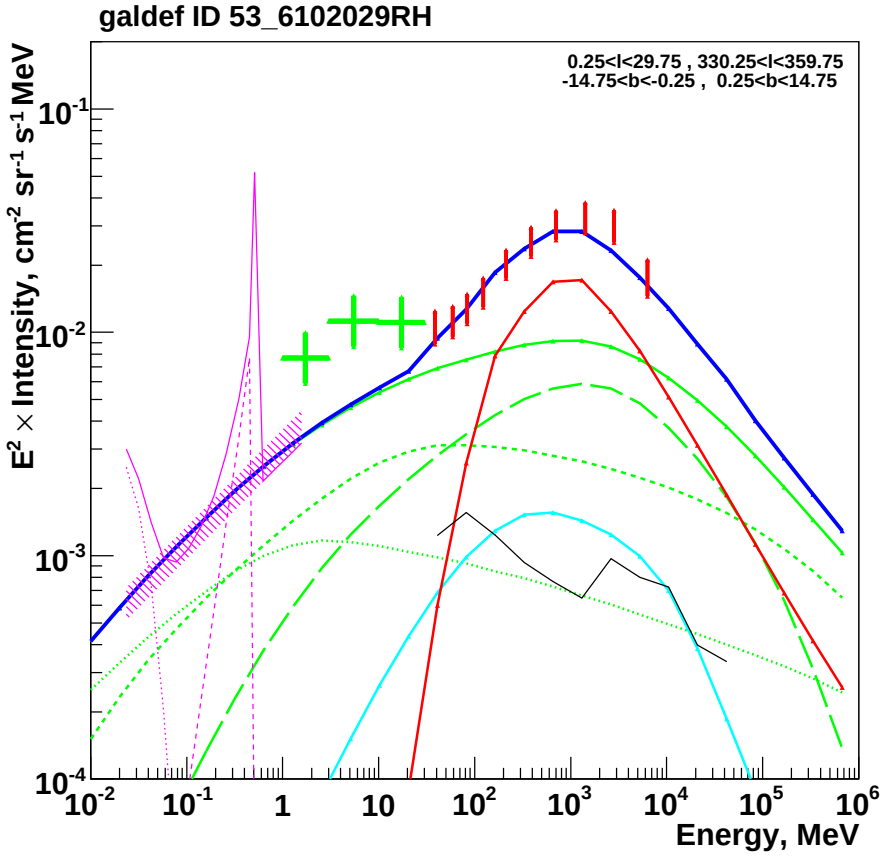

Figure 4.3: The spectrum of the diffuse emission for $330^\circ < l < 30^\circ, |b| < 15^\circ$ as calculated in the optimised GALPROP model for the ISRF with maximal metallicity gradient, with primary electrons only, Line-styles: red solid – π^0-decay, green broken – IC (optical [long dash], IR [short dash], CMB [dot]), green solid – total IC, cyan solid – bremsstrahlung, black solid – extragalactic γ-ray background (Strong et al. 2004a), blue solid – total. Data points: red – EGRET and green – COMPTEL, as in Strong et al. (2005); magenta – INTEGRAL/SPI (broken lines: components in fit to positronium + positron annihilation line + unresolved point sources; shaded region: power-law continuum) Bouchet et al. (2008). For the SPI power-law continuum the uncertainty is estimated as described in the text. In this and subsequent figures, the identifier (e.g., 53_6102029RH) corresponds to the GALPROP version and run used; all parameters of the model are contained in the "GALDEF" parameter file for future reference and are available from the GALPROP website at `http://galprop.stanford.edu`.

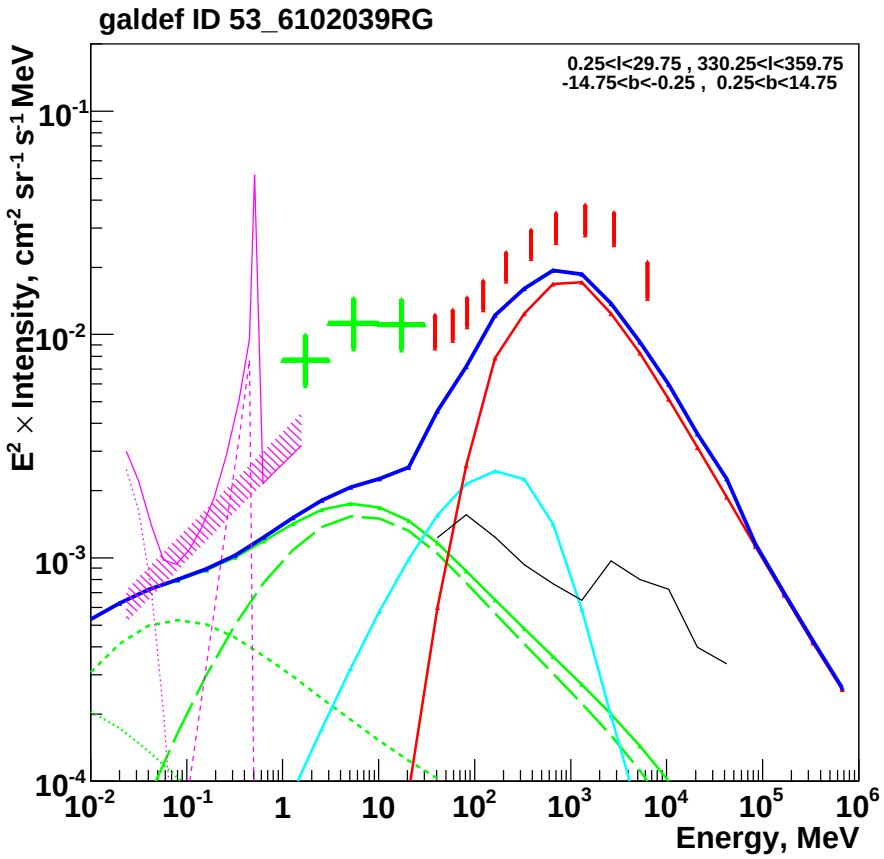

Figure 4.4: The spectrum of the diffuse emission for $330^\circ < l < 30^\circ, |b| < 15^\circ$ as calculated in the optimised GALPROP model for the ISRF with maximal metallicity gradient, with secondary electrons and positrons only, Line-styles: red solid – π^0-decay, green broken – IC (optical [long dash], IR [short dash], CMB [dot]), green solid – total IC, cyan solid – bremsstrahlung, black solid – extragalactic γ-ray background (Strong et al. 2004a), blue solid – total. Data points: red – EGRET and green – COMPTEL, as in Strong et al. (2005); magenta – INTEGRAL/SPI (broken lines: components in fit to positronium + positron annihilation line + unresolved point sources; shaded region: power-law continuum) Bouchet et al. (2008).

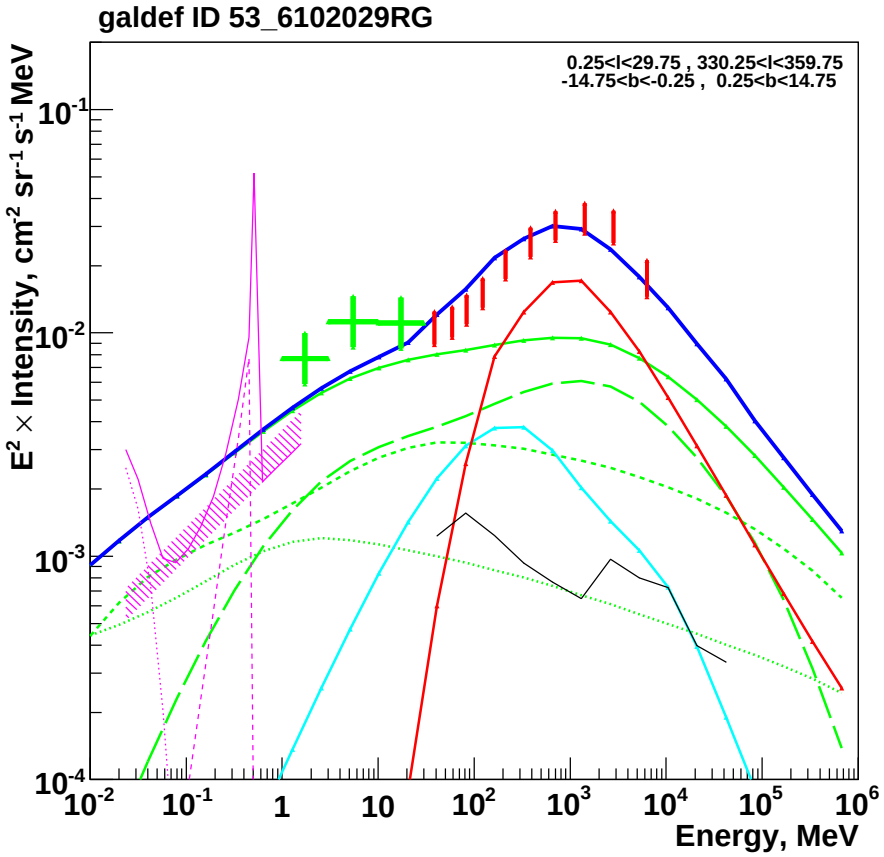

Figure 4.5: The total spectrum of the diffuse emission as calculated in the optimised model for $330^\circ < l < 30^\circ, |b| < 15^\circ$ with the maximum metallicity gradient. Line and data styles as for Fig. 4.3.

important between 100 MeV and 10 GeV, while the bremsstrahlung contribution is minor. The inclusion of secondary electrons and positrons increases the IC emission below ~ 100 MeV by up to a factor ~ 2, an effect that was pointed out by Strong et al. (2004b). Interestingly, the agreement with the COMPTEL data is improved by the inclusion of the secondary electrons/positrons, although the model still shows a deficit. Instead the SPI data are overpredicted, but the spectral slope is still consistent with the data below 1 MeV given the estimated uncertainties. A possible remedy to recover the model fit if the CR nuclei to primary electron ratio is reduced could be that we have simply underestimated the optical component of the ISRF. If the CR nuclei flux is reduced to improve the agreement with SPI the model emission in the EGRET energy range would also be reduced, because of the relation of primary CR and π^0-decay emission. The emission in the MeV energy range comes from secondary electrons/positrons IC scattering the optical component of the ISRF, and primary electrons IC scatter the same component to GeV energies.

To see the dependence of the sub-MeV emission on the assumed ISRF model, the diffuse emission for the case of no metallicity gradient was calculated. This case of no metallicity gradient is shown in Figure 4.6. The major change in the ISRF is a $\sim$30% reduction in the infrared emission which is due to the smaller amount of dust in the inner Galaxy when using this ISRF model. This results in a drop of $\sim$10–15% for the predicted intensity of the diffuse emission below $\sim$1 MeV than the maximal gradient case. The optical emission increases only slightly, while the CMB emission is the same. The total spectrum of the diffuse emission does not change significantly under this variation of the ISRF showing the robustness of the calculations.

The reduction in the infrared reduces the contribution by secondary electrons and positrons to the total emission below a few hundred keV. In this energy range the emission by primary electrons is also reduced, but by a smaller amount because there is still a contribution by IC scattering of the CMB (see Fig. 4.3 and Fig. 4.4). Since the CMB is known, and if the infrared component of the ISRF is low, the emission below a hundred keV traces the primary electron spectrum in the ISM.

We have made our principal comparison with the spectrum for $|b| < 15^\circ$ since this is the nominal range for the spectrum presented in Bouchet et al. (2008). To see the effect of different latitude ranges, the diffuse emission for $|b| < 10^\circ$ and $|b| < 5^\circ$ was calculated and compared with the data for these

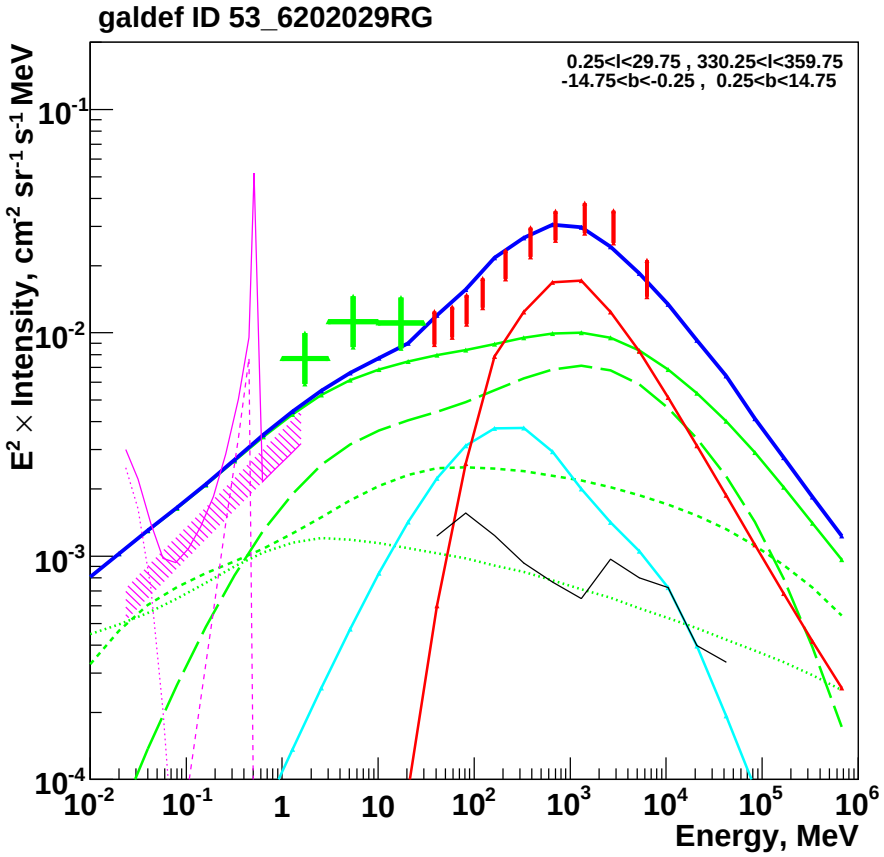

Figure 4.6: The spectrum of the diffuse emission as calculated in the optimised model with contribution of secondary electron and positrons and ISRF without the metallicity gradient. Region $330° < l < 30°, |b| < 15°$. Line and data styles as in Fig. 4.5.

ranges. Since the model emission is qualitatively similar to the data also for the reduced latitude ranges, I will not report it here.

4.3.3 Outer Galaxy: Inverse Compton as contribution to the X-ray background?

We have seen that EGRET data of the diffuse emission and recently also INTEGRAL data of the Galactic center are well described by the GALPROP code. In this paragraph the estimates are made also for lower energies, i.e. for 1 to 10 KeV, and for the outer Galaxy and compared with the X-ray data of the extra-galactic background (Gilli et al. 2007). The ISRF and the same electron spectrum used to fit INTEGRAL data have been adopted to reproduce the plotted emission in Figure 4.7. The lower blue line represents the Galactic emission form GALPROP from the pole region, while the upper one is for the region ($300<l<360$; $10<b<40$) (for most of the observations of CXB the contribution of Galactic emission should be between these lines). Below 10 MeV the emission is given only by IC. In the figure COMPTEL and EGRET EB are the extragalactic background. There is also plotted the unresolved CXB percentage (green arrows) obtained by Hickox & Markevitch (2007) in the Chandra deep fields after excluding all detected X-ray, optical and infrared sources that is (7 ± 3)% in 1-2 keV and (4 ± 9)% in 2-5 keV. Hickox & Markevitch (2007) concluded that "the remaining diffuse intensity includes emission from the Galaxy as well as from the hypothetical warm-hot intergalactic medium (WHIM), and provides a conservative upper limit on the WHIM signal that comes interestingly close to theoretical predictions." Solid lines under CXB refer to the contribution of different AGN classes according to (Gilli et al. 2007): unobscured AGN, obscured Compton-thin AGN, total AGN plus galaxy cluster are shown with a red, blue and magenta curve, respectively and the contribution of Compton-thick AGN (black line). To conclude, Figure 4.7 shows that this Galactic emission contributes at few $\%$ level and may become important for constraining the WHIM emission.

4.3.4 Discussion and Conclusions

The hard X-ray continuum is consistent with the predictions in both intensity and spectral index (Porter et al. 2008). However, the uncertainties in the model are still considerable: the distribution of CR sources and gas in the in-

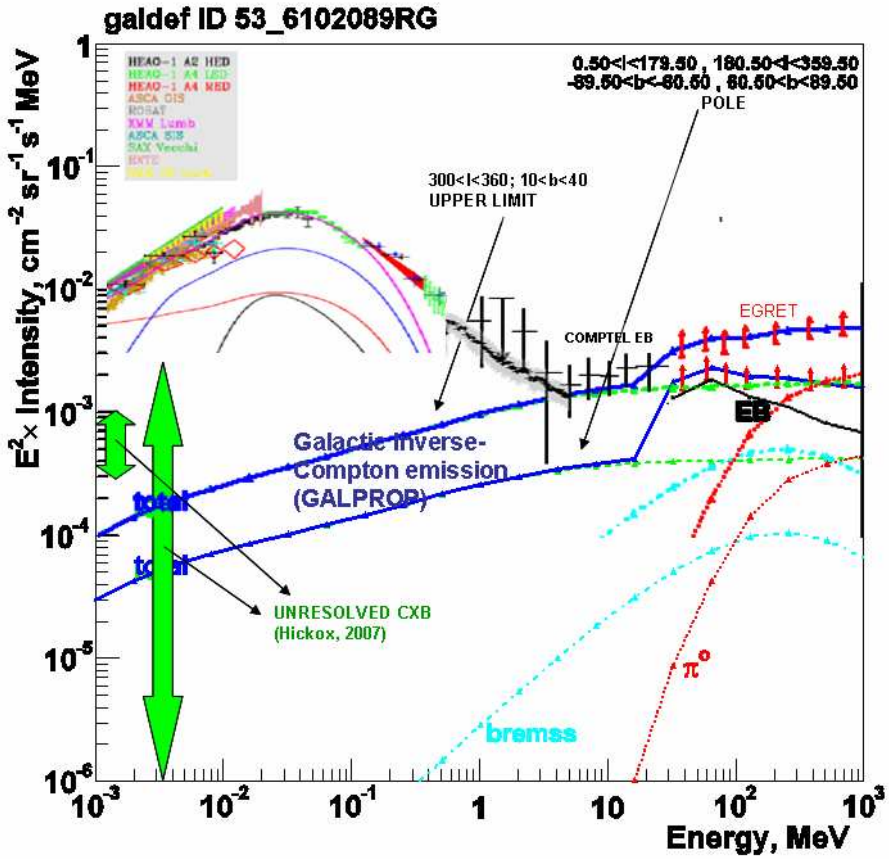

Figure 4.7: This plot shows the comparison between the data of the cosmic x-ray background (Gilli et al. 2007) and the modelled contribution of the inverse-Compton (IC) emission (GALPROP) from the Galaxy produced by cosmic-ray electrons on the interstellar radiation field (ISRF) and the CBM. Below 10 MeV the emission is given only by IC. The lower blue line represents the Galactic emission from the pole region, while the upper one is for the region (300<l<360; 10<b<40) (for most of the observations of CXB the contribution of Galactic emission should be between these lines). In the figure COMPTEL and EGRET EB are the extragalactic background. There is also plotted the unresolved CXB percentage (green arrows) obtained by Hickox & Markevitch (2007) in the Chandra deep fields. The different XRB measurements are explained on the top left. Solid lines under CXB refer to the contribution of different AGN classes according to (Gilli et al. 2007): unobscured AGN, obscured Compton-thin AGN, total AGN plus galaxy cluster are shown with a red, blue and magenta curve, respectively and the contribution of Compton-thick AGN (black line).

ner Galaxy which affect both the primary and secondary electrons/positrons, and the optical and infrared part of the ISRF (the CMB is known exactly). In fact, our optimised model overpredicts the SPI fluxes, which could simply reflect these uncertainties, but the agreement in the spectral shape gives confidence that the mechanism is correctly identified.

There is still an excess in the COMPTEL energy range between 1–30 MeV which is to be explained.

Hence, GALPROP model predicts too much emission below 1 MeV but seem to reproduce the spectral slope. Reducing the CR nuclei source spectrum to improve the sub-MeV agreement is a possibility. However it cannot be reduced too much since the local CR antiproton measurements must still be reproduced by the model.Moreover, increasing the optical component of the ISRF could improve the agreement at MeV. Variation of the primary electron injection index below a few GeV is another possible remedy to the over-production of diffuse emission below 1 MeV. But for example when the conventional model of CR electrons (Strong et al. 2004b) is used the situation is not improved: the sub-MeV emission will be lower, but in general the agreement with the COMPTEL and EGRET data will be worse.

A small contribution from populations of unresolved compact sources, particularly anomalous X-ray pulsars and radio pulsars, which may have very hard spectra extending to a few hundred keV (Kuiper et al. 2006) is still possible.

In addition the estimates are made also for lower energies, i.e. for 1 to 10 keV, and compared with the X-ray data of the extra-galactic background, showing that it can contribute at a few $\%$ level. This work illustrates the intrinsic connection between the diffuse Galactic γ-ray emission in different energy ranges. Moreover, this Galactic emission could be important and significant for future missions, such as Simbol-X, and for constraining the WHIM emission.

To conclude, inverse Compton emission by CR electrons and positrons on starlight and infrared radiation are the most important components of the hard X-ray and γ-ray emission in the 100 keV to few MeV range. An important part of this emission is produced by secondary electrons and positrons, the spectrum of which depends on the CR nuclei spectrum at energies $\sim$ few GeV and higher. These CRs also produce π^0-decay γ-rays that dominate the emission in the GLAST range from 100 MeV to $\sim$10 GeV. Hence, GLAST observations of the π^0-decay diffuse emission will also constrain in the future the

contribution by secondary electrons/positrons to the diffuse γ-ray emission in the SPI energy range. With the secondary electrons/positrons fixed, SPI observations probe the IC emission of primary CR electrons with energies $\leq$ 10 GeV scattering the infrared component of the ISRF and the CMB.

Moreover, since most of the diffuse γ-ray emission between $\sim$10 GeV - 10 TeV is produced via IC scattering of primary electrons on the same starlight and infrared photons, it provides a connection to observations of diffuse emission at TeV energies by HESS (Aharonian et al. 2006) and MILAGRO (Abdo et al. 2007).

4.4 Diffuse synchrotron emission from the Galaxy

The same electrons responsible for the diffuse gamma-ray emission produce also synchrotron emission by gyrating in the Galactic magnetic field. Hence, complementary to gamma-rays, knowing the Galactic synchrotron emission it is possible to obtain information on the relativistic electrons in the Galaxy and on the Galactic magnetic field.

I have implemented in GALPROP some 3D models of the Galactic magnetic field in order to calculate the synchrotron emission from the Galaxy. In this Chapter only two of those models will be reported. Details of the implemented model are given below. In Strong et al. (2000) only the random component of the magnetic field was present and was implemented in 2D with an exponential law for the component. Some changes have been made in order to have a more realistic and non symmetric model of the synchrotron emission; the Galactic magnetic field was modelled in 3D including its regular and irregular component, taking into account the spiral structure.

Skymaps, longitude and latitude profile, intensity maps and spectral index plots were produced as outputs where different models can be compared with data collected from different radio surveys. The intensity of synchrotron emission brings information about magnetic field intensity, while its spectrum brings information about the spectrum of cosmic-ray electrons. The synchrotron emission in the 10 MHz-10 GHz band constrains the electron spectrum in the 1-10 GeV range. In particular the synchrotron spectral index β provides information on the ambient electron spectral index p (approximately β=2+(p-1)/2 after propagation) (Strong et al. 2000). Both these quantities are adjusted in order to reproduced the synchrotron and gamma-ray data.

4.4.1 Galactic magnetic field models

The first evidence of the existence of a Galactic magnetic field was derived from the observation of linear polarization of starlight by Hiltner (1949). Since then many measurements have been done using the Zeeman spectral-line splitting (for example in central region of the Galaxy), optical polarization data (to study the large-scale structures of the magnetic field in the local spiral arm) and the Faraday rotation measurements in the radio continuum emission of pulsars and of the extra-galactic sources. These measurements showed two components of the Galactic magnetic field: regular and random (Rand & Kulkarni 1989).

Usually the regular magnetic field of the disk is obtained by measurements of pulsar and extra-galactic radio sources. Generally the large scale spiral structure of the Galactic magnetic field is disturbed locally by turbulent motions of the gas (the random component) that has the effect of decreasing the polarization fraction with respect to what would be observed with only the large scale magnetic field. This turbulent depolarization is stronger at low Galactic latitudes since lines of sight in the Galactic plane cross more fluctuation than at high latitudes (Miville-Deschenes et al. 2008). Random fields appear to have a length scale of 50 - 150 pc compared to the kiloparsec scale of the regular component. Since the Galactic magnetic field is composed of a regular and a turbulent or random component, the model we used includes both parts. The regular component is modelled as a vector field B_{REG}(x, y, z), the random field as a scalar field B_{RAN}(x, y, z), with the option also to represent it as a vector in case explicit modelling of random orientations is required.

For our model of the Galactic magnetic field the radius r corresponds to the Galacto-centric distance, with the azimuth angle, θ measured clockwise from the Galactic centre-Sun direction. Our reference system is left-handed, with the Sun in the x direction, as seen in Fig. 4.8 for a spiral magnetic field model. The disk field is classified according to its symmetry properties and sign reversals: antisymmetric and symmetric configurations with respect to the transformation of the azimuthal angle $\theta + \pi$ are called bisymmetrical (BSS) and axisymmetrical (ASS), respectively. With respect to a reflection at the disk plane, a further notation A or S means that the field reverses sign at z=0, or it does not respectively. Since in the literature there are many models of the Galactic magnetic field, we decided to start from the formulation of Miville-Deschenes et al. (2008) as used for WMAP analysis and adapted for

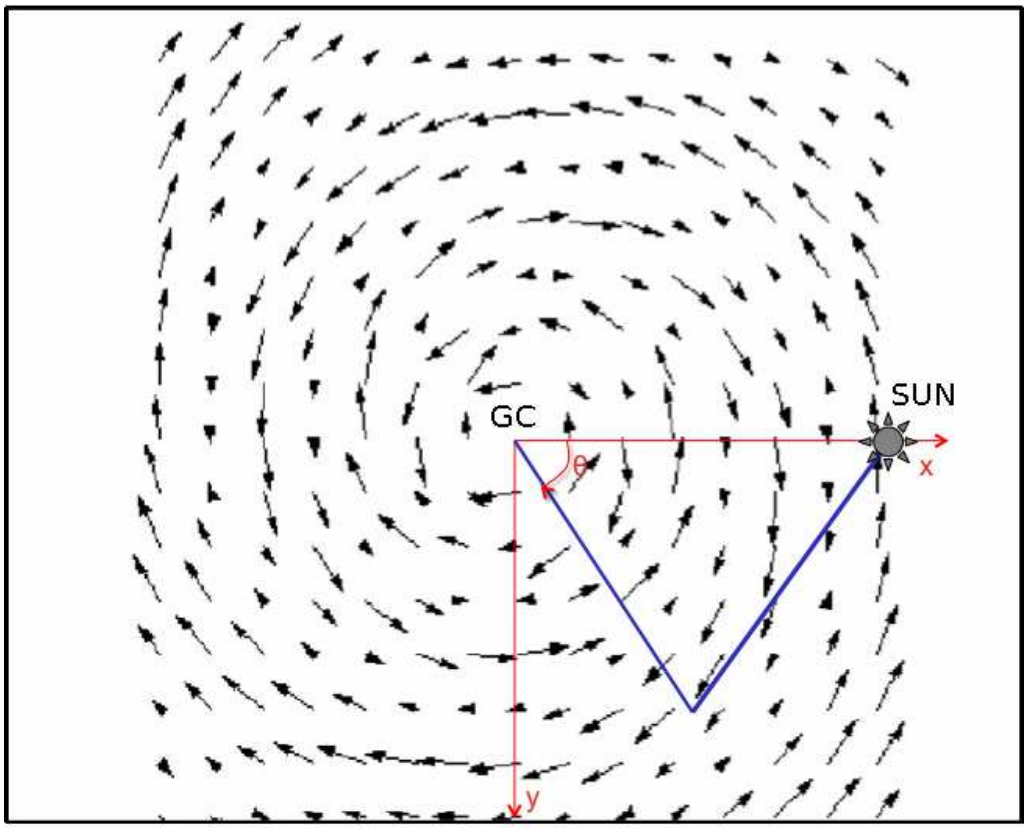

Figure 4.8: Bi-symmetric spiral model of the Galactic magnetic field for z=0 in the Galactic plane. The arrows and their size indicate the direction and the field strength. GC is the Galactic center and the Sun is at 8.5 kpc from it. The Sun is in the x direction and θ is measured clockwise from the Galactic centre-Sun direction. The image is 8.5 kpc $\times$ 10 kpc.

the 3D configuration and tune the values in order to have a good agreement with the synchrotron maps data. In the next sections I used also another model based on Tinyakov & Tkachev (2002), developed for ultra-high energy cosmic-ray propagation, as an alternative to test.

4.4.2 Galactic magnetic field: model 1

A recent study of synchrotron emission from the Galaxy via polarization analysis of the WMAP data performed by Miville-Deschenes et al. (2008) constrains the ratio of random over local regular component of the magnetic field to the value 0.57, but the absolute value is not determined by their polarisation study. Thus using this value we can look for the best fit to the data. I

start with the model adopted by Miville-Deschenes et al. (2008), that is the most recent used in the literature in particular for WMAP.

The random magnetic field is assumed constant in x, y falling off with z, while the regular part is inspired by Han & Qiao (1994) with the z dependence taken from Page et al. (2007).

The z component of the magnetic field is considered negligible, since Han & Qiao (1994) estimated it to be almost one magnitude smaller than the horizontal component. The same model is taken in the Miville-Deschenes et al. (2008) analysis. Our model is a BSS magnetic field and its three spatial components (x, y, z) are:

$$\begin{aligned} B_x(r,\theta,z) &= B_0\ cos(\theta - \psi\ ln\frac{r}{r_0})cos\ \chi\ sin\ (p-\theta); \\ B_y(r,\theta,z) &= B_0\ cos(\theta - \psi\ ln\frac{r}{r_0})cos\ \chi\ cos\ (p-\theta); \\ B_z(r,\theta,z) &= 0; \end{aligned} \tag{4.1}$$

where B_0 is the local field strength, taken constant with radial distances in Miville-Deschenes et al. (2008) and

$$\psi = 1/tan(p). \tag{4.2}$$

r is the radial distance and p=-8.5$\circ$ is the pitch angle, which describes how tightly wound the spiral arms are and determines the direction of the local field, i.e. the Galactic longitude l=90+p.

$$\chi(z) = \chi_0\ tanh(z/1kpc) \tag{4.3}$$

describes the vertical (z) component of the magnetic field, with χ_0=8$\circ$ (Miville-Deschenes et al. 2008) and r_0 = 11kpc, which depends on the distance to the closest magnetic fields reversal and represents the Galactocentric distance along the line between the Sun and the Galactic Centre to the field maximum (see Tinyakov & Tkachev (2002)). The intensity of the total regular field given by

$$B_{TOT} = \sqrt{(B_x^2 + B_y^2)} \tag{4.4}$$

is plotted in Fig. 4.9 for the case of z=0.

4.4.3 Synchrotron radiation theory

Synchrotron emission is produced by cosmic-ray electrons spiralling in the Galactic magnetic field. The intensity has been well measured at low frequencies (eg. 408 MHz by Haslam et al. (1982)) and can bring information

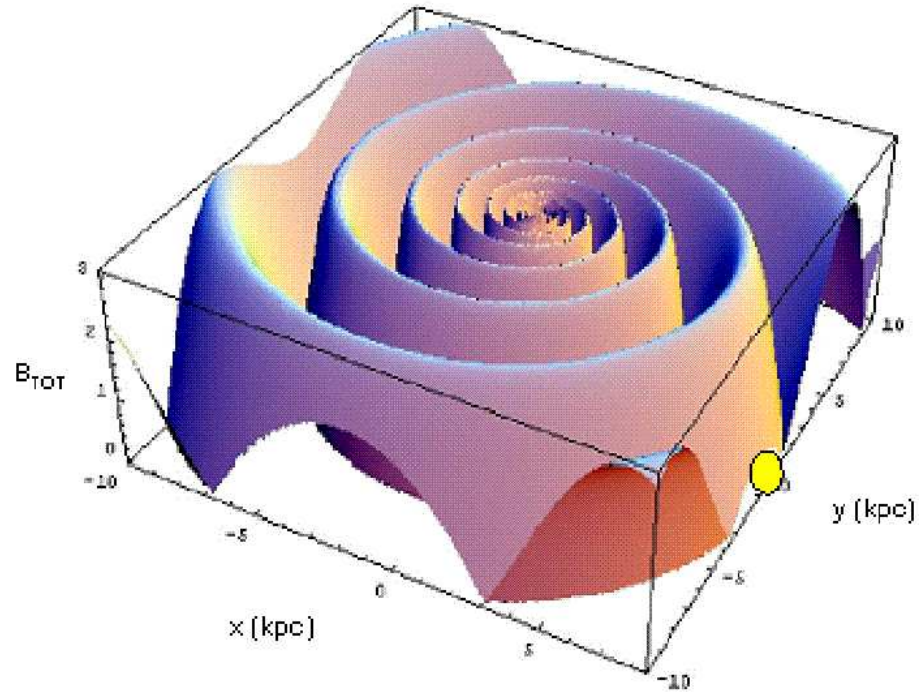

Figure 4.9: Total regular field of the magnetic field for model 1 and B_0 = 3 μ G, p= -8.5, χ_0= 8.0 and r_0 = 11 kpc. The position of the Sun is at 8.5 kpc in the x direction.

on models of the Galactic magnetic field. In particular, consideration is given to the spiral-arm structure of the regular field, including fitting the number and pitch of several logarithmic spiral-arm segments, and the role of the irregular field including its alignment with the regular component along these arms. However, there are practical difficulties with fitting such models to low frequency data, and moreover in the Galactic plane region there is also the contribution of free-free emission and the emission from supernova-remnants.

The synchrotron emissivity of an isotropic distribution of monoenergetic relativistic particles in a uniform magnetic field has polarized components parallel and perpendicular to the projection of the field on the line-of-sight to the observer (Longair 1994):

$$\epsilon_{par}(\nu,\gamma) = \frac{\sqrt{3}}{2}\, e^3 mc^2 B_{perp}\, [F(x) - G(x)] \tag{4.5}$$

$$\epsilon_{perp}(\nu,\gamma) = \frac{\sqrt{3}}{2}\, e^3 mc^2 B_{perp}\, [F(x) + G(x)] \tag{4.6}$$

where x = ν/ν_c, with ν_c= 3/4 $emcB_{perp}\gamma^2$ and with γ electron energy. The functions F(x) and G(x) are defined in terms of Bessel functions (Longair 1994), with:

$$F(x) = x \int_x^{\inf} K_{5/3}(x')\, dx'$$
$$G(x) = x\, K_{2/3}(x')\, dx' \tag{4.7}$$

where $K_{5/3}(x')$ and $K_{2/3}(x')$ are the modified Bessel function of order 5/3 and 2/3. $B_{perp} = B(x, y, z)\ sin\alpha$, with α pitch angle between the magnetic field and the line-of-side, that is the velocity of the electron. The resulting synchrotron spectrum has a broad maximum centred roughly at the frequency ν_c and the maximum has a value ν_{max}=0.29 ν_c (Longair 1994). The polarization formulation will be of interest for the future work, since it is not yet implemented in GALPROP. Hence, of our interest is the total polarization given by the sum of the two described above:

$$\epsilon(\nu, \gamma) = \frac{\sqrt{3}}{4}\, e^3 mc^2 B_{perp}\, F(x) \tag{4.8}$$

For a power law electron distribution with spectral index p, the synchrotron emissivity is given integrating over the electron energy, the emissivity for a single electron:

$$\epsilon(\nu) = \int_0^{inf} \epsilon(\nu, \gamma)\ k\ \gamma^{-p}\ d\gamma \tag{4.9}$$

The measured synchrotron emission is dependent on the density of the relativistic electrons along a given line-of-sight and on the perpendicular Galactic magnetic field. After some arrangement and calculations (Longair 1994) the emissivity can be writen as:

$$\epsilon(\nu) \propto B_{perp}^{(p+1)/2}\ \nu^{-(p-1)/2} \tag{4.10}$$

Hence, if the electron energy spectrum has a power-law with index p, the spectral index of the synchrotron intensity is (p-1)/2. However we perform the exact integration

$$\epsilon(\nu) = \int_0^{inf} \epsilon(\nu, \gamma)\ N(\gamma)\ d\gamma \tag{4.11}$$

The emissivity as seen by an observer at the solar position is output as a function of (x, y, z, ν). Synchrotron emissivity for regular and total components of our model of the magnetic field and for z=0 is shown in Fig. 4.10. The shape of the emissivity reflects the shapes of the spiral arms for the regular component of the magnetic field. The black circle where the emissivity is zero

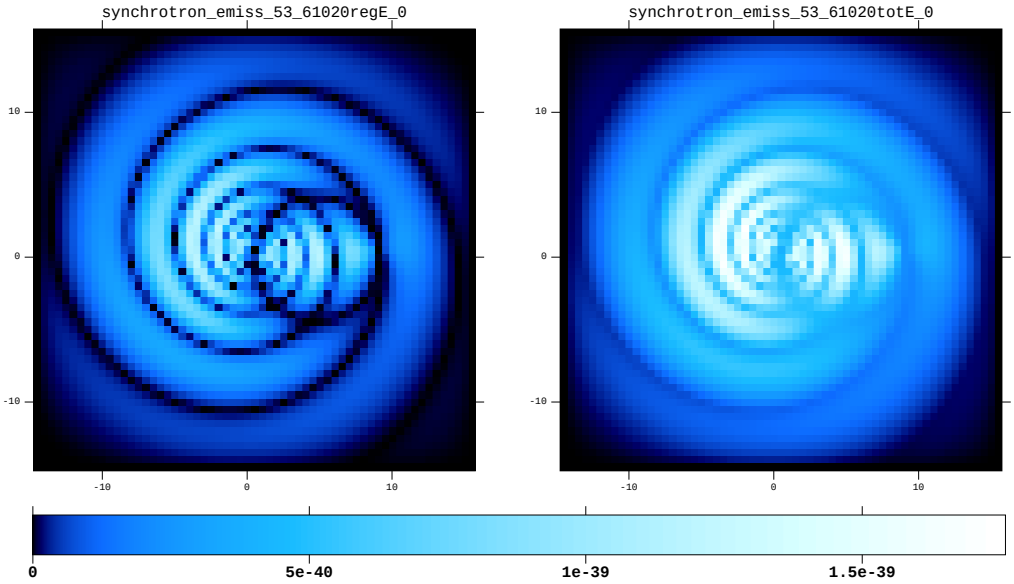

Figure 4.10: Synchrotron emissivity for regular (left) and total (right) components of our model of magnetic field integrated over electron energy. The shape of the emissivity reflects the shapes of the spiral arms for the regular component of the magnetic field. In both figures the Sun is at x=8.5 kpc and y=0. The black circle where the emissivity is zero on the right-center of the figures is where the magnetic field is parallel to the observer's line of sight from the observer point of view in the solar system. For details see text.

on the right-center of the figures has a simple geometrical explanation: from the observer point of view in the solar system the emissivity is null when the magnetic field is parallel to the observer's line of sight and hence the perpendicular component is null as well. In fact the emissivity is proportional to the perpendicular component of the magnetic field (see eq.4.10). This region is roughly a circle with the diameter equal to the Galactic center-Sun distance and is the locus of points subtending right angles at these positions.

With GALPROP calculation of the electron and positron spectrum at all points on the 3D grid, we then integrate on the line-of-sight to get the synchrotron intensity for the regular and random fields. The synchrotron intensity at frequency ν is then given by the integral along the line of sight of the emissivity:

$$I(\nu) = \int \epsilon(\nu)\, ds \tag{4.12}$$

The observed brightness of the radiation seen in a given direction is (Longair

1994):

$$T(\nu) \propto \frac{c^2 I(\nu)}{2\,\nu^2} \tag{4.13}$$

From this equation the spectral index of the synchrotron radiation β results to be:

$$\beta = 2 + (p-1)/2 \tag{4.14}$$

The resulting synchrotron skymaps for a frequency of 408 MHz as an example, in Galactic coordinates (l,b), is shown in Fig. 4.11 for regular and random components of the magnetic field. Note that after the integration of the emissivity along the line-of-sight the signature of spiral arms is no longer visible.

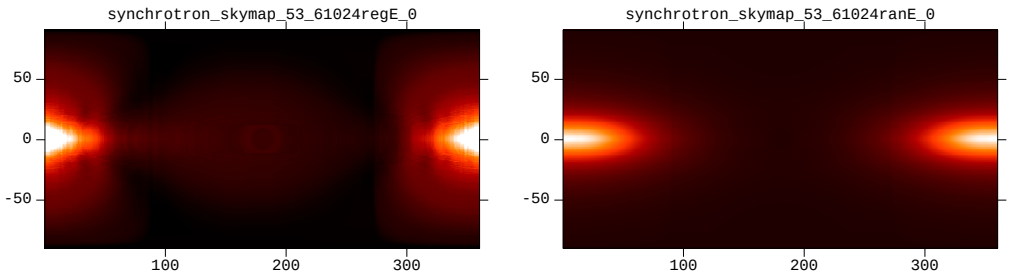

Figure 4.11: Synchrotron skymaps for a frequency of 408 MHz as example in Galactic coordinates (l,b) for regular (left) and random (right) components of the magnetic field. The Galactic centre is at (0,0) at the edge of the figures.

4.4.4 Testing the electron spectrum

Gamma-ray data were used to constrain the optimized model for CR electron spectrum with a break at 20 GeV, as we used in the previous paragraphs.

Figure 4.12 and Figure 4.13 show the longitude and latitude distributions of the gamma-ray emission respectively for optimized electron spectrum with the break at 20 GeV. These profiles show good agreement with the EGRET data in all energy ranges.

This optimized electron spectrum adopted by GALPROP model has an injection spectral index of 1.5 below 20 GeV and 2.4 above this energy, this before propagation effects. After propagation it becomes softer, around 2 and 2.9 below and above 20 GeV respectively. This means that the expected synchrotron spectrum is around 2.5 below 20 GeV and 2.9 above. The study here has been performed with only primary electrons . Hence, the following plots

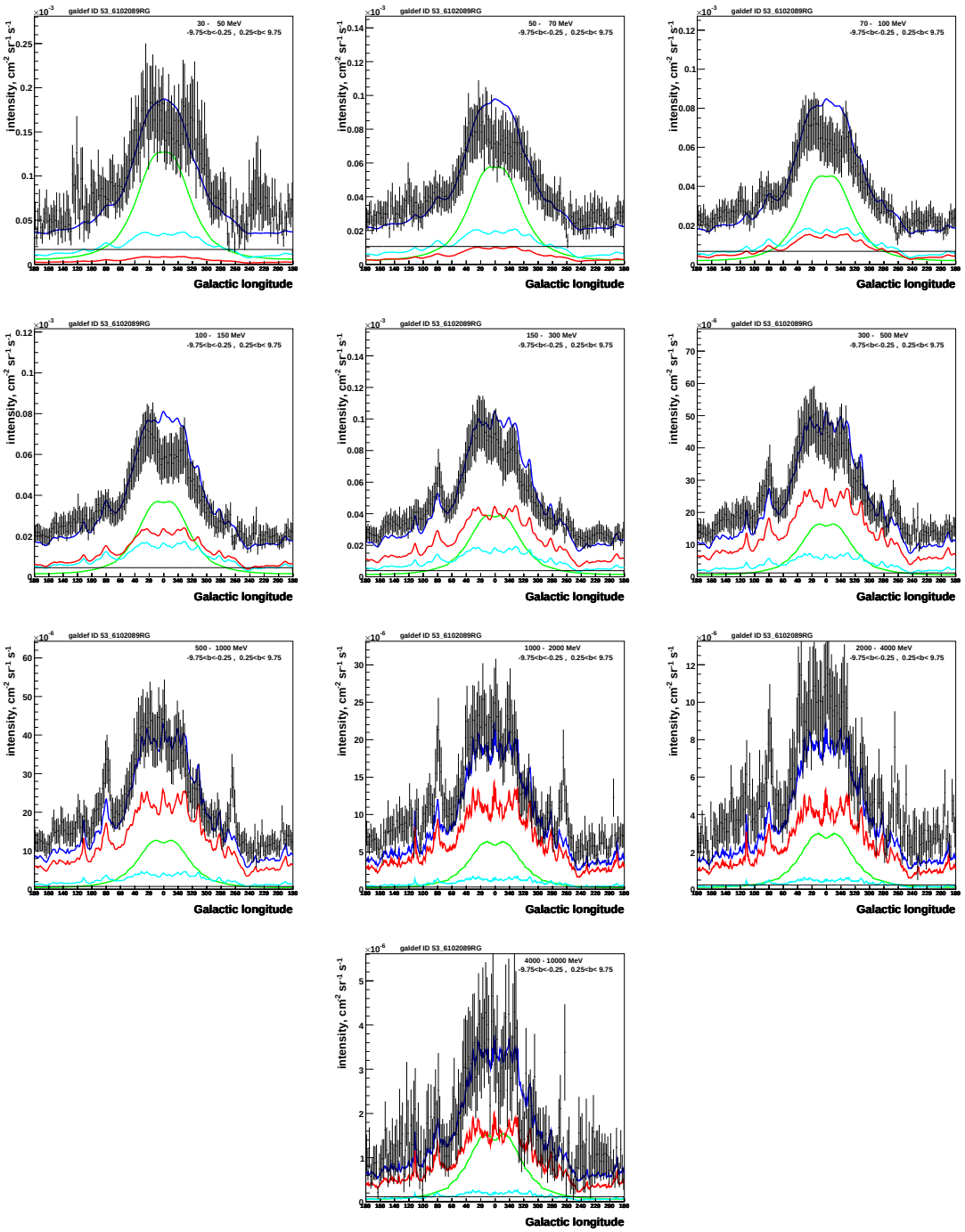

Figure 4.12: Longitude profiles ($|b| < 9$ deg) for the optimized model with the break at 20 GeV, compared with data: darker vertical bars: EGRET data. The extragalactic background is added to the total prediction shown as an horizontal black line. The model components are pion decay (red line), IC (green line), bremsstrahlung (cyan line) and total (blue line). The profiles are calculated including secondary positrons and electrons.

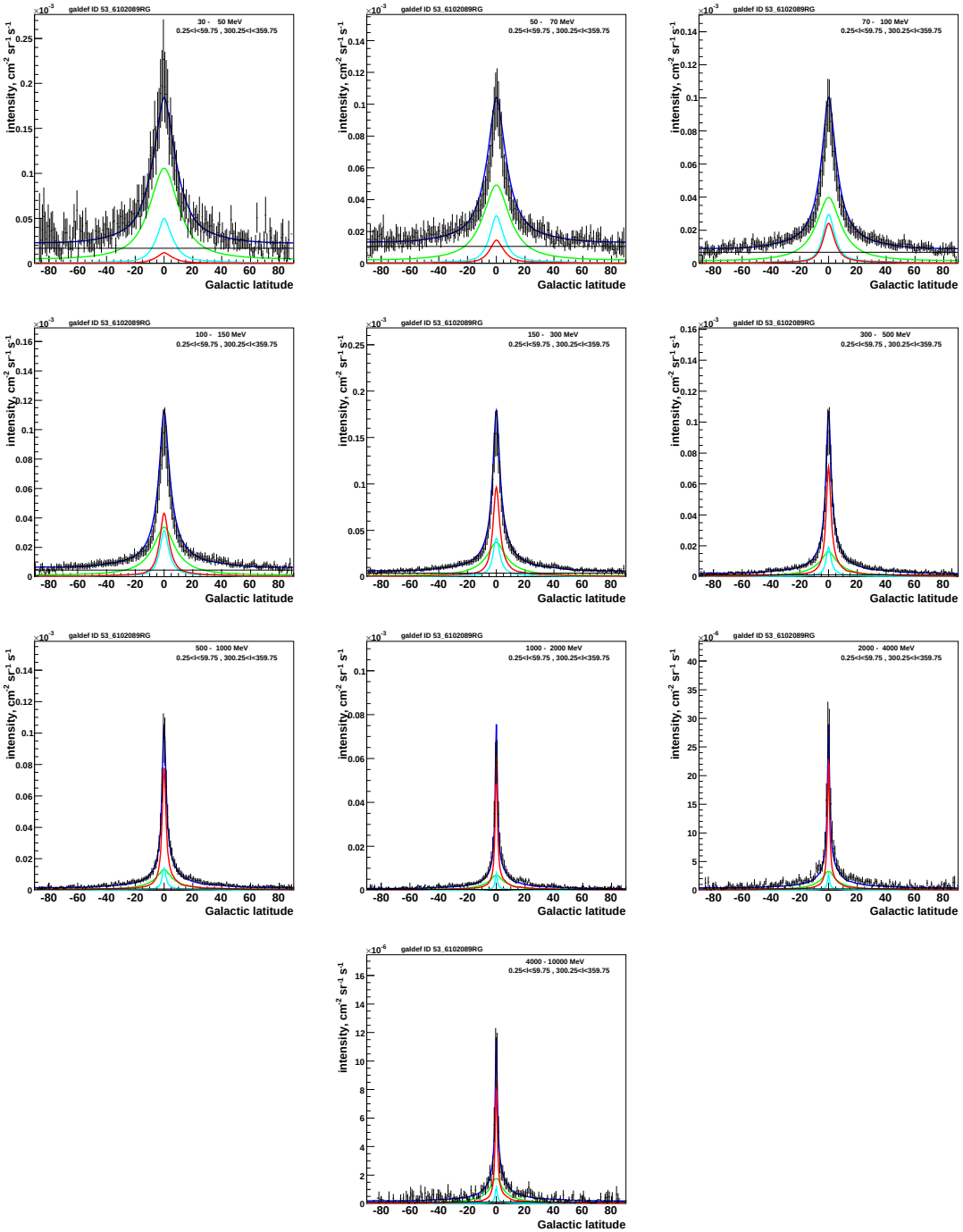

Figure 4.13: Latitude profiles (|l| <30 deg) for the optimized model with the break at 20 GeV, compared with data: darker vertical bars: EGRET data. The extragalactic background is added to the total prediction shown as an horizontal black line. The model components are pion decay (red line), IC (green line), bremsstrahlung (cyan line) and total (blue line). The profiles are calculated including secondary positrons and electrons.

were calculated without the contribution of secondary electrons and positrons, whose effect is notable only below 500 MHz, corresponding to electrons below 5 GeV. In fact around 400 MHz the contribution of secondaries is only about 20%. The effect of secondary electrons and positrons is shown in Fig. 4.16.

Recently a re-analysis of the WMAP synchrotron data (Miville-Deschenes et al. 2008) including spinning dust correction have resulted in a lower intensity than previous analysis. Spinning dust emission is produced by small grains rotating and produces unpolarized radio emission. **?**)nalyzed the combination of the WMAP polarization and intensity data finding strong evidence for the presence of unpolarized spinning dust emission in the 20-60 GHz range. They performed an analysis of the WMAP synchrotron emission at 23 GHz where the signal to noise ratio is the highest (Miville-Deschenes et al. 2008) and the polarised emission is only synchrotron. Their estimates of the intensity at this frequency are based on extrapolation of the Haslam 408 MHz data with a spatially varying spectral index constrained by the WMAP 23 GHz polarization data. Hence, supposing that the synchrotron spectral index does not vary with frequency over the WMAP range, they found an anomalous emission with a spectrum from 23 to 61 GHz in accordance with the models of spinning dust.

Figure 4.14 shows the synchrotron spectrum for the optimized model of the electron spectrum used up to now compared with the official WMAP data and with the corrected WMAP data (Miville-Deschenes et al. 2008). Calculations and data are for the northern Galaxy, where in general there are more complete data from radio surveys. The GALPROP optimized model does not give a good fit to synchrotron spectrum considering the new WMAP data points. Hence, decreasing the magnetic field intensity may give a reasonable fit. However the lower intensity of the WMAP data has effects not only on the magnetic field intensity, but also on the cosmic-ray electron spectrum previously obtained from GALPROP to fit both gamma-ray and radio data, since the slope of the synchrotron spectrum is changed (see Fig. 4.14).

After some tests on varying the electron spectrum, Figure 4.15 shows the synchrotron intensity spectrum for the conventional electron spectrum and a new electron spectrum which we call modified-optimized electron spectrum, which has the break at 10 GeV instead of 20 GeV. The conventional model would not fit the data even if the magnetic field would increase (see Fig. 4.16 on top). Moreover secondaries would make the fit even worse, increasing the intensity below 400 MHz (see Fig. 4.16 bottom), suggesting the conventional

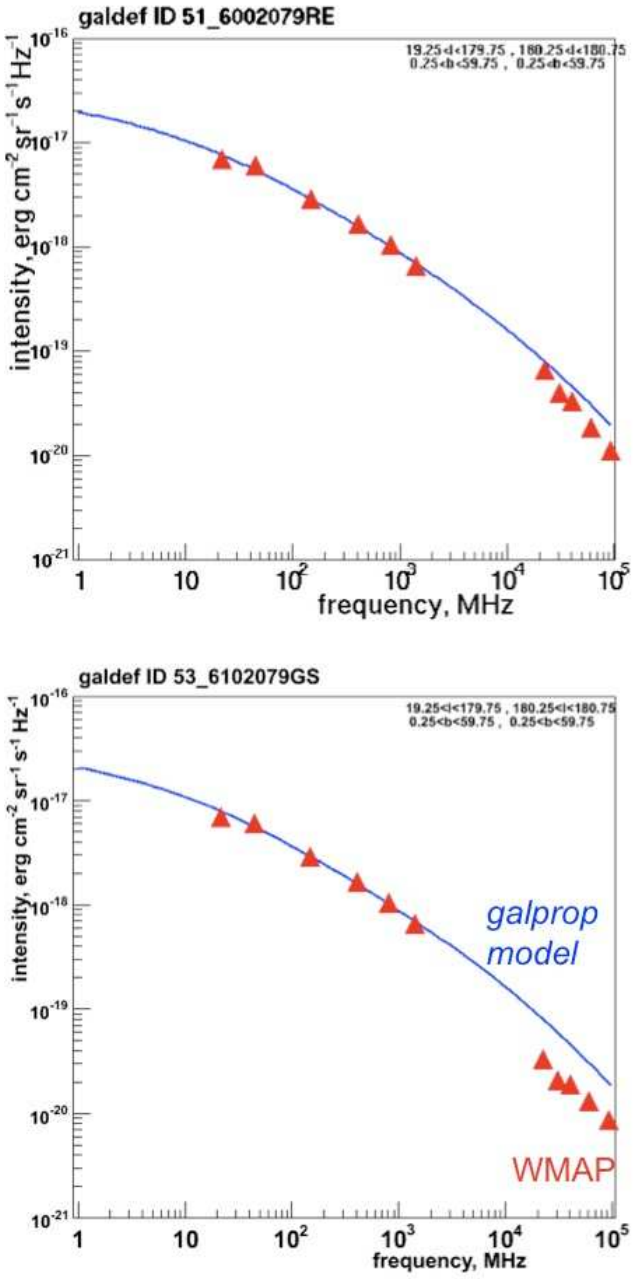

Figure 4.14: Synchrotron spectrum for the optimized model (blue line) of the electron spectrum compared with the data (red points), on top with the old WMAP data, while on bottom with the corrected WMAP data (Miville-Deschenes et al. 2008). Calculations and data are for the northern Galaxy, which ranges are described in the plots. This is calculated for primary electrons only. The effect of secondary electrons and positrons is shown in Fig. 4.16. Data above 20 GHz are from WMAP, while below this energy data are from various radio surveys (Details on radio surveys data will be given in Strong et al. (in prep.)

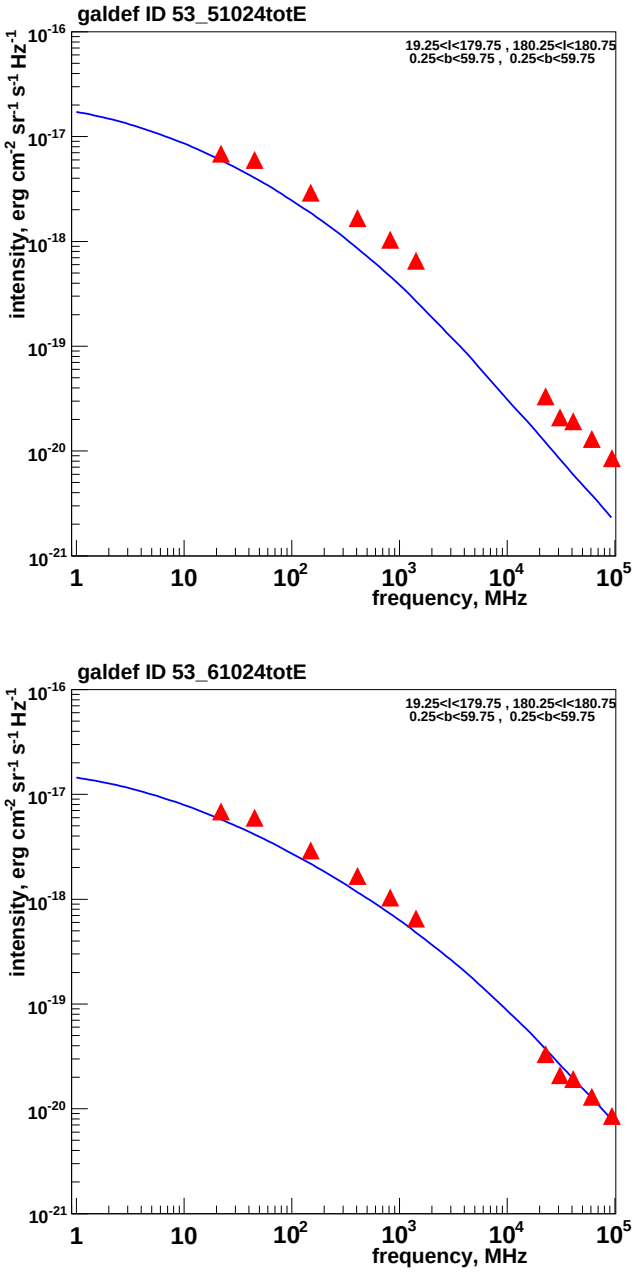

Figure 4.15: Synchrotron intensity spectrum for the conventional (top) and the modified-optimized electron spectrum with the break at 10 GeV (bottom). Blue lines are the models, while red points are the data described in Fig 4.14. Models are calculated for primary electrons only. The effect of secondary electrons and positrons is shown in Fig. 4.16. The magnetic field values are taken in such a way to fit the intensity of the synchrotron emission.

model does not fit the data.

From these figures we can infer that not only the gamma-ray data but also the synchrotron data support the optimized model, confirming the need for a break in the cosmic-ray electron injection spectrum. However, tuning the electron spectrum to fit synchrotron data suggests a break at 10 GeV instead of 20 GeV as previous used for fitting gamma-ray data with the GALPROP code (see previous paragraphs on the gamma-ray emission, Fig. 4.12 and Fig. 4.13 and Strong et al. (2004a) for more details). The magnetic field values are adjusted to fit the intensity of the synchrotron emission. More details on the magnetic field intensity are explained in the next paragraph.

4.4.5 Synchrotron results: model 1

This section considers the synchrotron emission for the electron spectrum with a break at 10 GeV and the magnetic field model 1. We have tuned B_0 in such a way that the ratio of random over local regular component of the magnetic field is fixed to the value 0.57 and we have tested the model to fit the WMAP data. The value of 3 μG taken by Tinyakov & Tkachev (2002) and Miville-Deschenes et al. (2008) gives a synchrotron intensity calculated by GALPROP too low. We took B_0=5 μG and B_{ran}=2.9 μG, in agreement with Miville-Deschenes et al. (2008) ratio and WMAP data.

Synchrotron spectra are shown in Fig. 4.17 for the inner Galaxy and for random, regular and total components of the magnetic field compared with radio surveys. We see that also for the inner Galactic region there is a good agreement with the data. For comparison, the synchrotron intensity for the northern Galaxy was plotted in Fig. 4.16 (bottom).

In Fig. 4.18 and Fig. 4.19 are shown the latitude and longitude profiles for 408 MHz. Plots are for random and regular components of the magnetic field, and also the sum for two different longitude regions. Regarding the latitude profiles, the data are more peaked than the model in the Galactic centre, and in the outer Galactic region the emission is almost constant for the same longitude range, while the model decreases too slowly away from the Galactic centre. For the longitude profiles and for $|b| < 0.75$ deg the model is about a factor of 2 lower than data, while for $|b| < 60$ deg is a good approximation. The same is shown in Fig. (4.20) and (4.21) but for 23 GHz. For the case of the latitude profiles, both for the inner and outer Galaxy and only the emission at the peak has the value expected from the model, while once more the

model decreases too slowly away from the Galactic centre. On the other hand the longitude profiles is well reproduced for $|b| < 0.75$ deg. In general a more rapid decrease of the magnetic field at higher latitude may improve the fit, as discussed in the next section.

4.4.6 Gamma-ray emission: model 1

For comparison Fig 4.22 gives the gamma-ray spectrum calculated with the modified optimized electron spectrum with the break at 10 GeV and with secondary contribution compared with the data. It gives an overprediction of gamma-ray at EGRET low energies.

Hence the adjusted interstellar electron spectrum does not allow the gamma-ray spectrum to be well fitted over the whole energy range. Figure 4.23 and Figure 4.24 show the longitude and latitude distributions of the gamma-ray emission respectively. Also here there is an overprediction of the emission in the Galactic centre region below 300 MeV. This will put a lower limit on the break: it cannot be at energies less than 10 GeV. However the break at higher energies would improve the fit with the gamma-ray data. Model 2 in the next paragraphs will investigate this hypothesis assuming the break at 15 GeV.

4.4.7 Galactic magnetic field: model 2

The synchrotron profiles show that there is not very good agreement with the data. Hence I try a different model of the magnetic field to see if it can improve the fit. In this model the random component is taken as in the previous model, while model of the regular component which can better fulfil these requirements is taken from Tinyakov & Tkachev (2002) BSS-A model. The three spatial components of the magnetic field (x, y, z) are:

$$B_x(r,\theta,z) = B_r\ cos(\theta - \psi\ ln\frac{r}{r_0})\ f(z)\ sin\ (p-\theta);$$
$$B_y(r,\theta,z) = B_r\ cos(\theta - \psi\ ln\frac{r}{r_0})\ f(z)\ cos\ (p-\theta);$$
$$B_z(r,\theta,z) = 0; \qquad (4.15)$$

where p, ψ and r_0 where defined for our previous model and have the same values. The function B_r represent the radial profile of the field's magnitude, with:

$$B_r = B_{SUN}\ (R_{SUN}/r)\ for\ r > 4kpc;$$
$$B_r = const\ for\ r < 4kpc; \qquad (4.16)$$

For the following analysis I took the value B_{SUN}=5μG; R_{SUN} is the Galactic center-Sun distance. The vertical decay is given by the exponential law

$$f(z) = sign(z)\ exp(-|z|/h) \tag{4.17}$$

where the scale height of the Galactic halo, h , is assumed 1.5 kpc in the Tinyakov & Tkachev (2002) model. With respect to the model 1, in the Galactic plane at z=0 the only difference is the increase of the total magnetic field intensity from the solar system towards the Galactic center(GC) till 4 kpc distance from the GC. For the z dependence, an exponential decrease at higher latitude would reflect in a steeper decrease in the synchrotron intensity away from the Galactic centre. This effect could have a positive influence on the quality of the fit. Moreover also a different distance dependence from the Galactic centre may explain the difficulty of the model to explain the peak in the data.

4.4.8 Synchrotron results: model 2

Here a modified-electron spectrum with the break at 15 GeV is used.

Synchrotron spectra are shown in Fig 4.25 for the inner Galaxy and for the northern Galaxy for the magnetic field model 2 compared with radio surveys. We see that also with this spectrum there is a good agreement with the new WMAP data. The synchrotron data including radio surveys below 400 MHz are not well reproduced by the model, however uncertainties in this region of the radio data may be higher.

In Fig. 4.26 are shown the latitude profiles for 408 MHz and 23 GHz. Calculations are made for the modified electron spectrum with the break at 15 GeV, with the model 2 of the magnetic field and including secondary electrons and positrons. The 408 MHz latitude profile in the inner Galaxy improves significantly with this model while the 23 GHz latitude profile in the same region is improved, but is still not completely reproduced. For the outer region of the Galaxy there is a good agreement at 23 GHz, but the 408 MHz profile shows that the intensity of the modelled magnetic field may be too low. With respect to model 1 there is a better agreement with the data.

Figure 4.27 shows the latitude profiles for 408 MHz and 23 GHz, for the modified-electron spectrum with the break at 15 GeV. These profiles do not show any particular improvement with respect to model 1. The agreement is still satisfactory.

4.4.9 Gamma-ray emission: model 2

For comparison Fig 4.28 gives the gamma-ray spectrum calculated with the modified optimized electron spectrum with the break at 15 GeV and with secondary positrons and electrons contribution compared with the data. It still overpredicts the gamma-ray flux at EGRET low energies, but is satisfactory within errors. In this case, the shift of the break from 10 GeV to 15 GeV improves the fit with gamma-ray data, as expected. Figure 4.29 and Figure 4.30 show the longitude and latitude distributions of the gamma-ray emission respectively for electron spectrum break at 15 GeV. There is an overprediction of the emission in the Galactic centre region below 300 MeV, but the fit is still acceptable.

4.4.10 Discussion

Combining the study on the gamma-rays with that on the synchrotron emission we can constrain better the electron spectrum.

On the other hand this study is also important for constraining the Galactic magnetic field using the synchrotron emission. A more structured brightness temperature along the longitude profiles can be achieved also varying the random component of the magnetic field. In fact a future step may be varying the random component following the regular one. In this case the random magnetic field intensity may scale as the regular part, i.e.:

$$B_{RAN} = 0.57 \times B_{REG} \tag{4.18}$$

the random component follows the regular one, and hence the spiral form can have more effect. Figure 4.31 shows this effect for 408 MHz and for the longitude and latitude profile as an example. In this case the regular component intensity is taken as in model 2, while the random component varies proportionally with the regular field. This assumption produces more modulation in the expected emission which can fit better the large scale data. However at the moment a further improvement on the fit is not needed since there are still big uncertainties in the radio data.

In addition, the synchrotron distribution is dependent on the electron density, and hence it varies with position in the Galaxy due to perturbation and accelerating effects and is dependent also on magnetic field variations. Hence, the synchrotron spectral index is expected to vary as a function of position in the Galaxy. However, since the aim is to trace the shape of the synchrotron

profile, not to fit the clumpiness, our model can not reproduce the asymmetries in latitude or fine details of the longitude distribution of synchrotron emission.

4.4.11 Conclusions

The synchrotron and gamma-ray data support the optimized model, and both confirm the need for a break in the cosmic-ray electron injection spectrum. First the break in the spectral index of the electrons was moved from 20 GeV to 10 GeV in order to obtain a better fit with the new results of the analysis of the synchrotron WMAP data. However, I showed that this spectrum does not reproduce the gamma-ray EGRET data at low energy. Hence the break has been moved to 15 GeV. The new electron spectrum at 15 GeV break is called modified-optimized electron spectrum and can can fit better both gamma-ray and synchrotron data. However it may be adjusted in future as at the moment further improvements on the fit are not necessary since there are still big uncertainties in the radio data. I also show that the two magnetic field models used in this analysis do not seem to be confirmed by synchrotron data and hence the spatial variation of the magnetic field may be further adjusted to get a better fit to the main radio surveys for the longitude and latitude profiles. As next step the synchrotron polarisation will be inserted in the GALPROP code.

A parallel study between cosmic rays, gamma rays and synchrotron is very promising, especially in view of the upcoming GLAST, PLANCK missions. PLANCK will extend the measurement of the Galactic synchrotron spectrum beyond the 30-100 GHz range of WMAP. In fact it is designed to work between 30 to 800 GHz. Emission at these frequencies is produced by 20-50 GeV electrons, which have radiative lifetimes of the order of 10^7 years in the diffuse interstellar medium. In addition, inverse-Compton scattering is produced by these and higher-energy electrons in the 10-100 GeV band which is detected by GLAST.

Since Galactic synchrotron is a foreground for CMB studies there is a large overlap of interest between these fields. Exploitation of these data for CR studies has only just begun but is expected to accelerate with the forthcoming Planck mission (Strong et al. 2007).

Using the all-sky multifrequency Planck observations of both intensity and polarisation, an accurate determination of the orientation of the large-scale

magnetic field (B_{reg}) and the magnitude of the turbulent part of the field (B_{turb}) will be possible.

In order to observe the CMB in the 20-200 GHz range it is necessary to separate the CMB and other foreground emissions. The intensity of the emission from the Galactic interstellar medium reaches a minimum in this range, but is still stronger than the CMB over a significant fraction of the sky. Hence, the study of the CMB is complicated by free-free, synchrotron and thermal dust emissions. A model of Galactic synchrotron emission such as that described here may be necessary not only for studies of gamma-rays but also for investigations on the CMB.

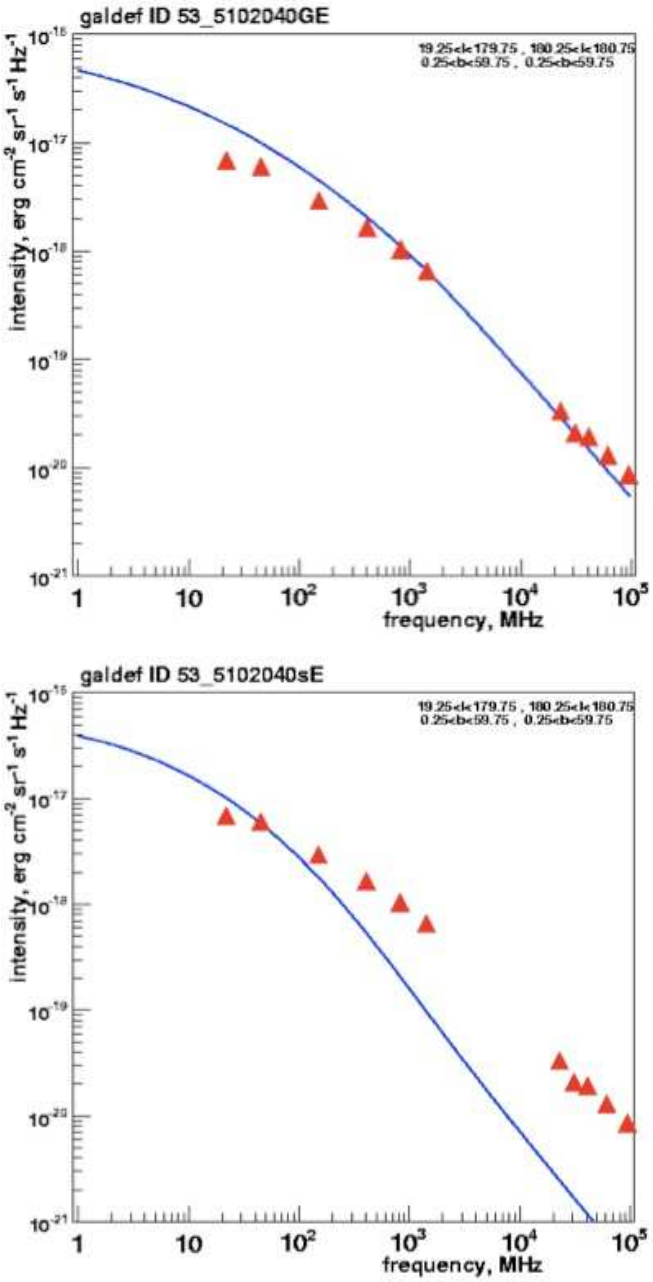

Figure 4.16: Synchrotron intensity spectrum for the conventional electron spectrum with higher magnetic field for primary electrons only (top) and for secondary electrons and positrons only (bottom). Blue lines are the models, while red points are the data described in Fig 4.14. Conventional would not fit the data even if the magnetic field would increase. Moreover including secondary positrons and electrons would make the fit even worse, increasing the intensity below 500 MHz, suggesting the conventional model does not fit the data.

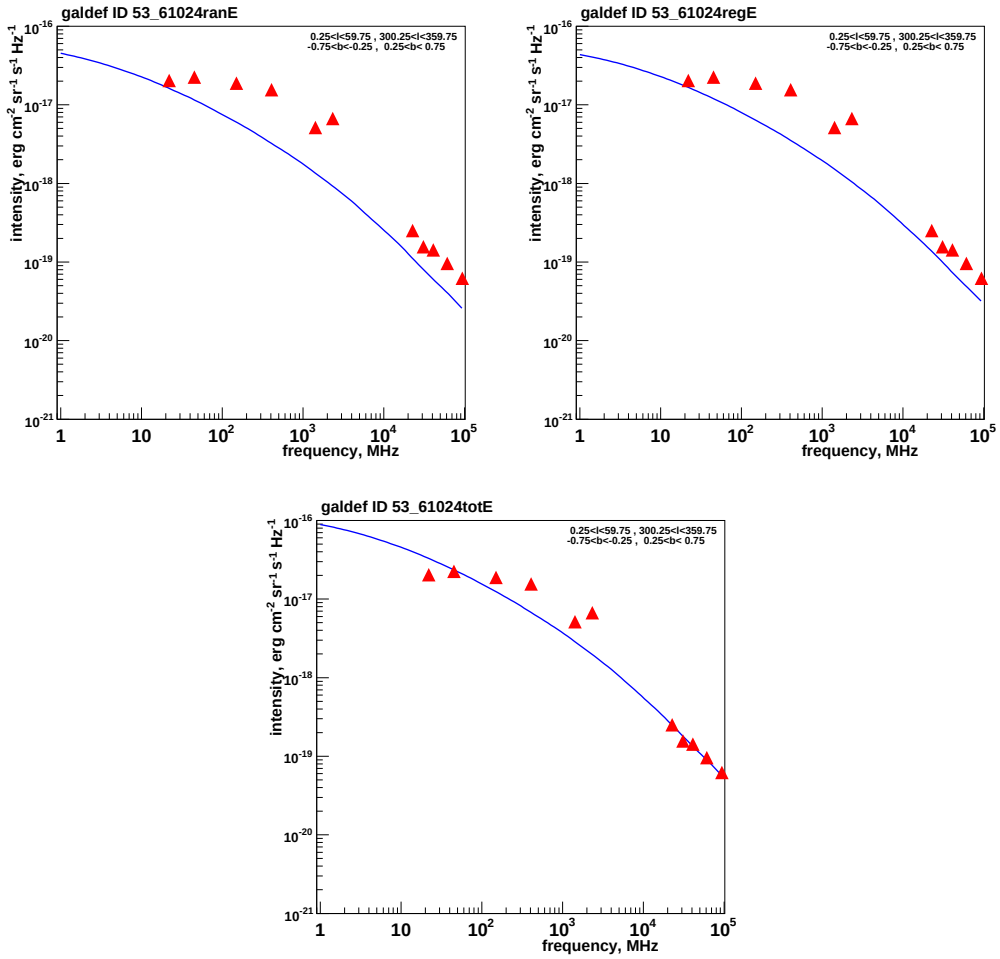

Figure 4.17: Synchrotron spectrum for the inner Galaxy. Up to down, random, regular and total components of the magnetic field compared with radio surveys. The electron spectrum has the break at 10 GeV. Blue lines are the models, while red points are the data described in Fig 4.14 with the new data from Miville-Deschenes et al. (2008). For comparison, the synchrotron intensity for the northern Galaxy was plotted in Fig. 4.16 (bottom).

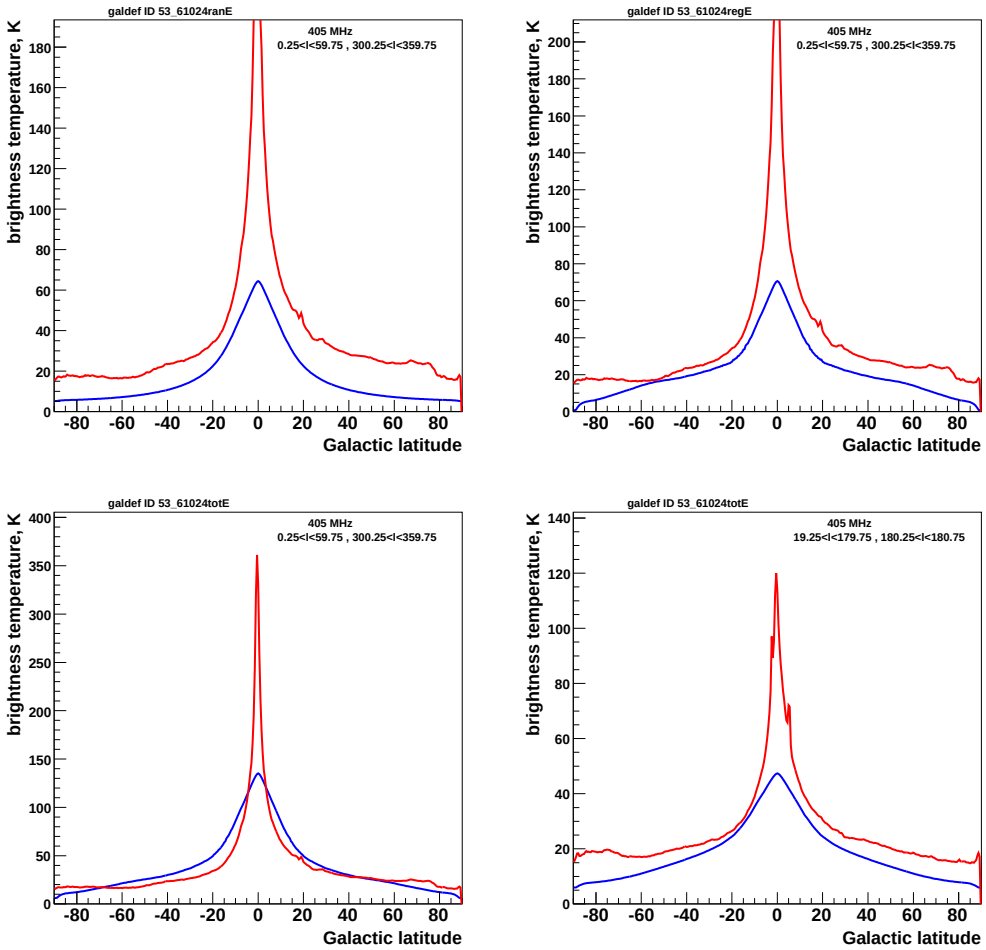

Figure 4.18: Synchrotron latitude profiles at 408 MHz. Upper plots are for random (left) and regular (right) components of the magnetic field, while bottom ones are for the sum for two different longitude regions for the modified-electron spectrum with the break at 10 GeV. Blue lines are the models, while red lines are the data described in Fig 4.14 with the new data from Miville-Deschenes et al. (2008).

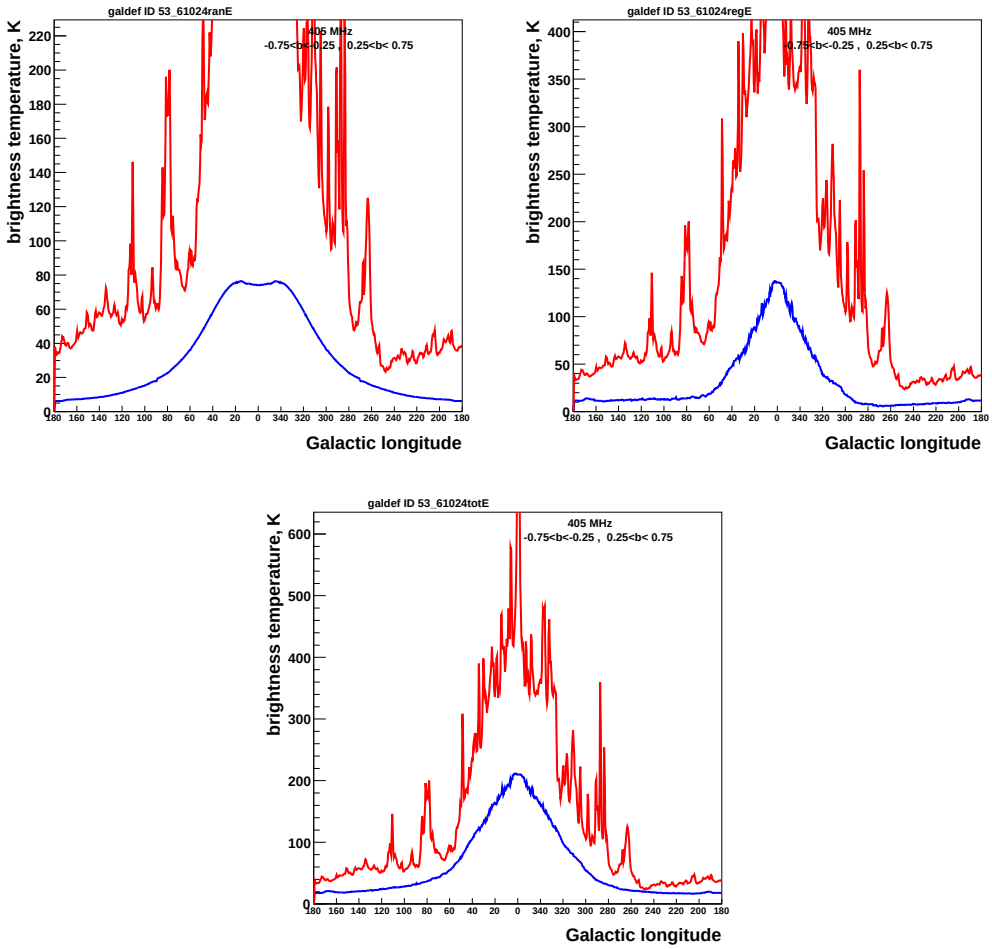

Figure 4.19: Synchrotron longitude profiles at 405 MHz for the modified-electron spectrum with the break at 10 GeV. Upper plots are for random (left) and regular (right) components of the magnetic field, while the bottom one is for the total magnetic field. Blue lines are the models, while red lines are the data described in Fig 4.14 with the new data from Miville-Deschenes et al. (2008).

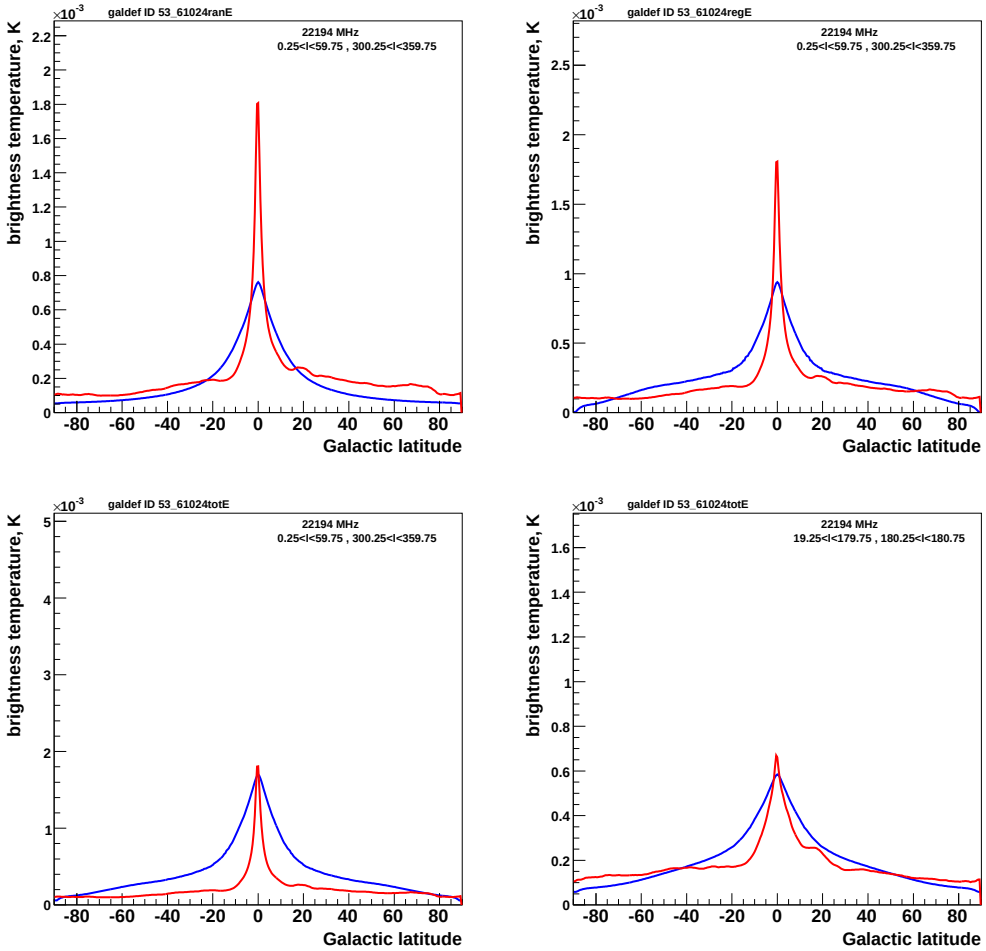

Figure 4.20: Synchrotron latitude profiles at around 23 GHz for the modified-electron spectrum with the break at 10 GeV. Upper plots are for random (left) and regular (right) components of the magnetic field, while the bottom ones are the sum for two different longitude regions. Blue lines are the models, while red lines are the data described in Fig 4.14 with the new data from Miville-Deschenes et al. (2008).

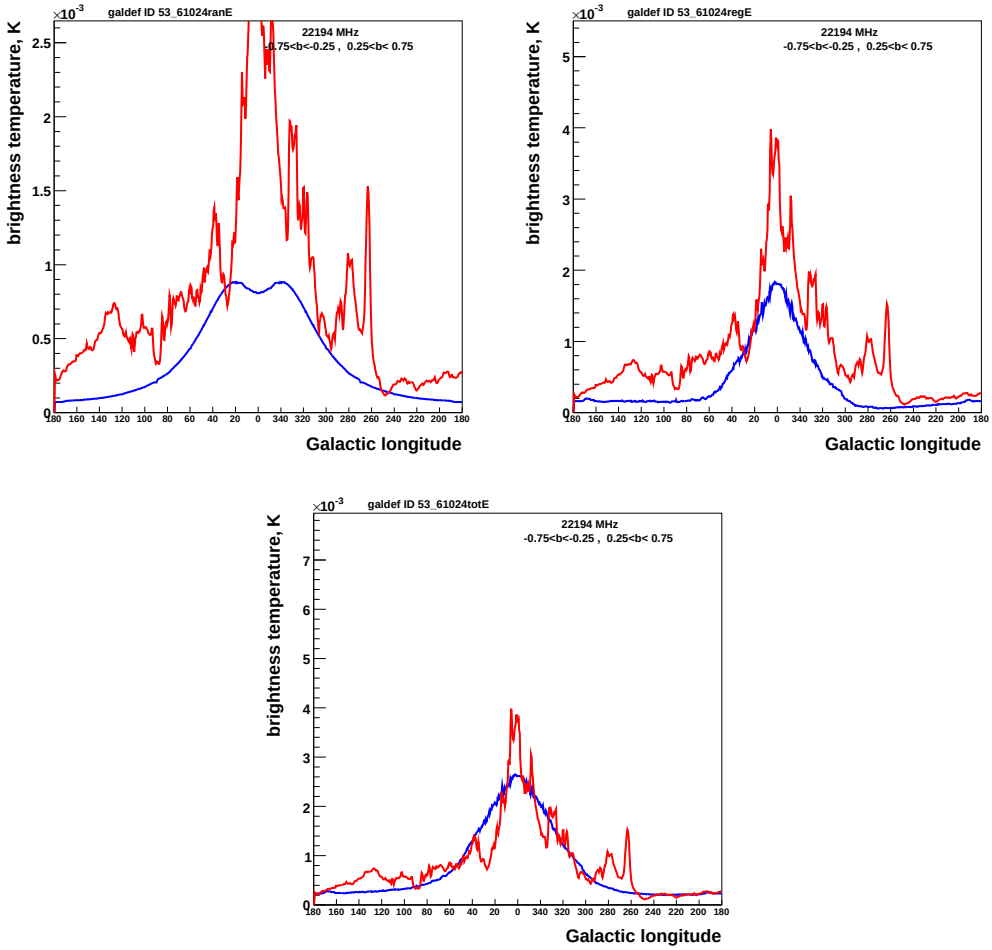

Figure 4.21: Synchrotron longitude profiles at around 23 GHz for the modified-electron spectrum with the break at 10 GeV. Upper plots are for random (left) and regular (right) components of the magnetic field, while the bottom one is for the total magnetic field. Blue lines are the models, while red lines are the data described in Fig 4.14 with the new data from Miville-Deschenes et al. (2008).

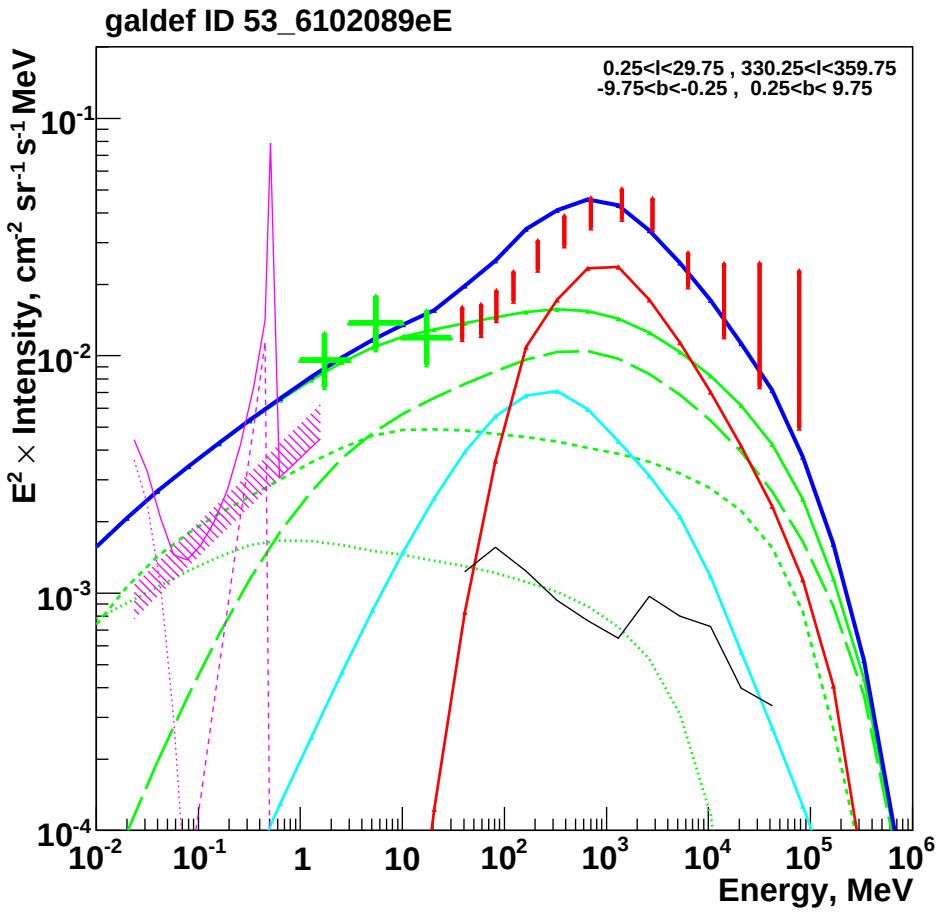

Figure 4.22: Gamma-ray spectrum calculated with the modified optimized electron spectrum with the break at 10 GeV compared with the data. It's visible an overprediction of gamma-ray at EGRET low energies, but still satisfactory. The spectrum includes also secondary positrons and electrons. Line and data styles as for Fig. 4.3

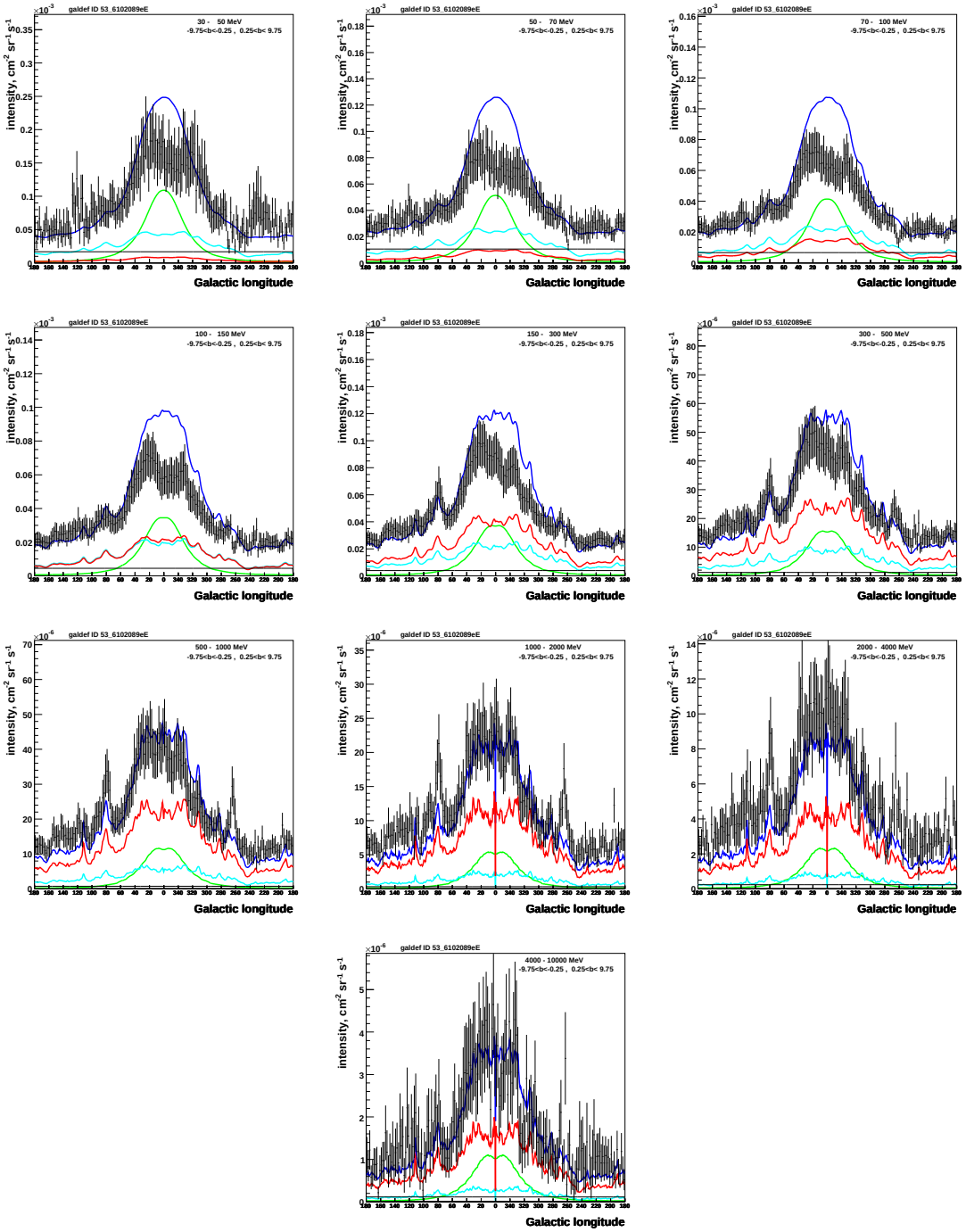

Figure 4.23: Longitude profiles ((|b| $<$ 9 deg) for the modified-optimized model with the break at 10 GeV, compared with data: darker vertical bars: EGRET data. The extragalactic background is added to the total prediction shown as an horizontal black line. The model components are pion decay (red line), IC (green line), bremsstrahlung (cyan line) and total (blue line). The profiles are calculated including secondary positrons and electrons.

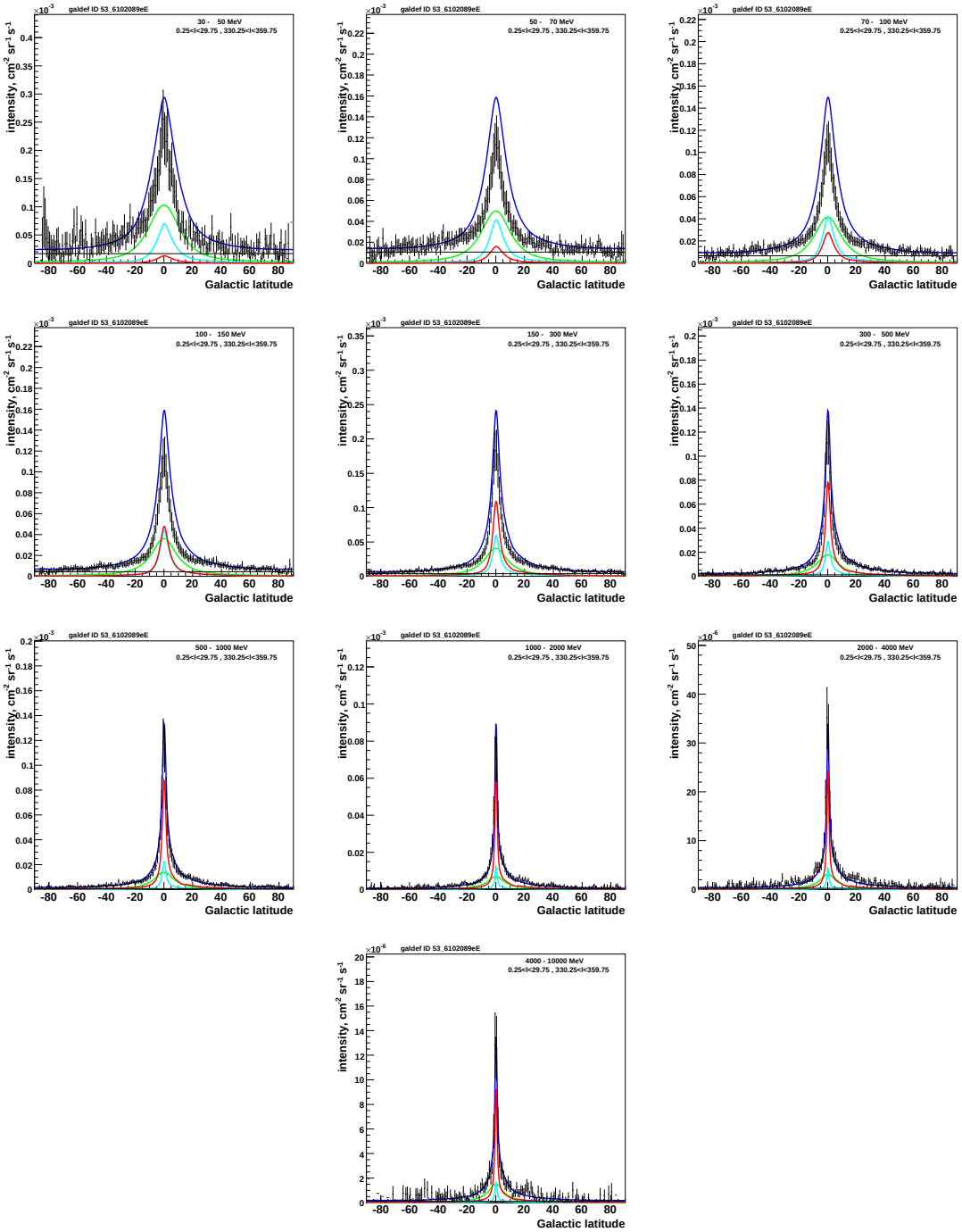

Figure 4.24: Latitude profiles ((|l| <30 deg) for the modified-optimized model with the break at 10 GeV, compared with data: darker vertical bars: EGRET data. The extragalactic background is added to the total prediction shown as an horizontal black line. The model components are pion decay (red line), IC (green line), bremsstrahlung (cyan line) and total (blue line). The profiles are calculated including secondary positrons and electrons.

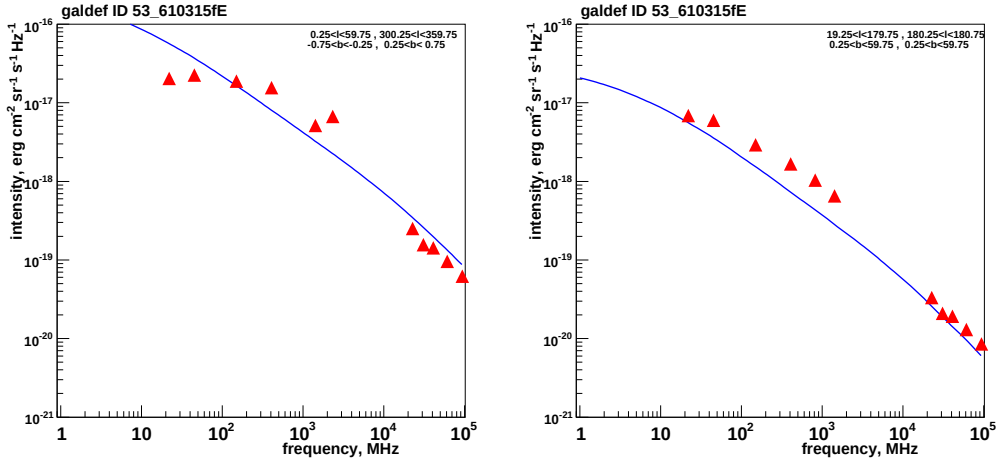

Figure 4.25: Synchrotron spectrum for the inner Galaxy (top) and for the northern Galaxy (bottom) for the model 2 of the total magnetic field compared with radio surveys. The electron spectrum has the break at 15 GeV and calculations are made including the secondary positrons and electrons as well. Blue lines are the models, while red points are the data described in Fig 4.14 with the new data from Miville-Deschenes et al. (2008)

.

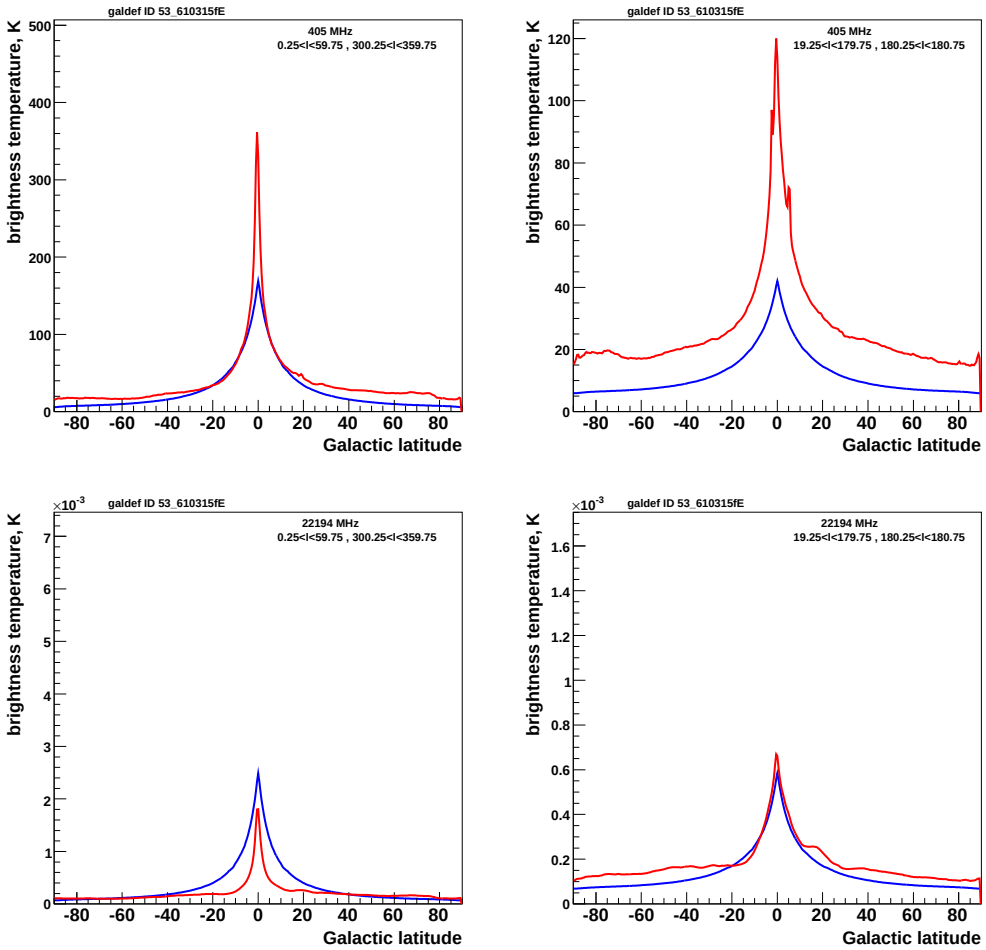

Figure 4.26: Synchrotron latitude profiles at 408 MHz (top) and 23 GHz (bottom). It is shown the for the modified electron spectrum with the break at 15 GeV, for model 2 of the magnetic field and including also secondary positrons and electrons. The plots are for two different longitude regions. Blue lines are the models, while red lines are the data described in Fig 4.14 with the new data from Miville-Deschenes et al. (2008).

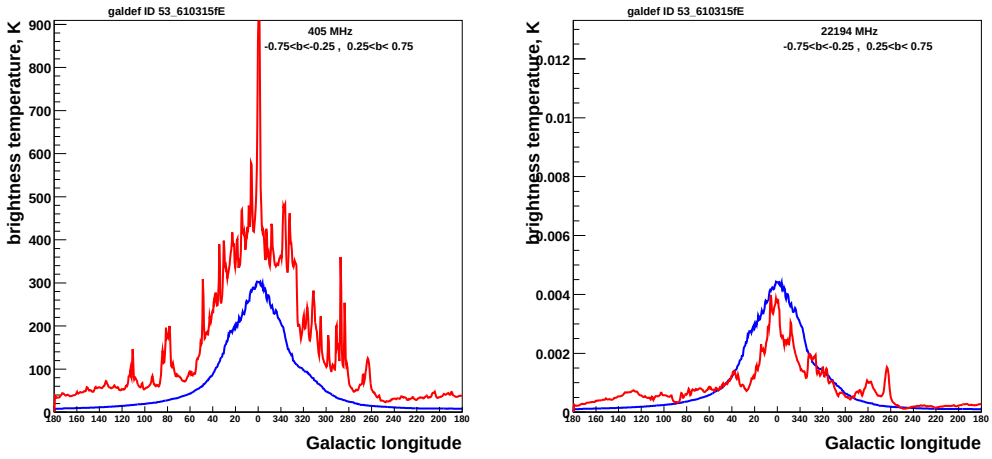

Figure 4.27: Synchrotron longitude profiles at 408 MHz and 23 GHz for the modified electron spectrum with the break at 15 GeV, for model 2 of the magnetic field and including also secondary positrons and electrons. Blue lines are the models, while red lines are the data described in Fig 4.14 with the new data from Miville-Deschenes et al. (2008).

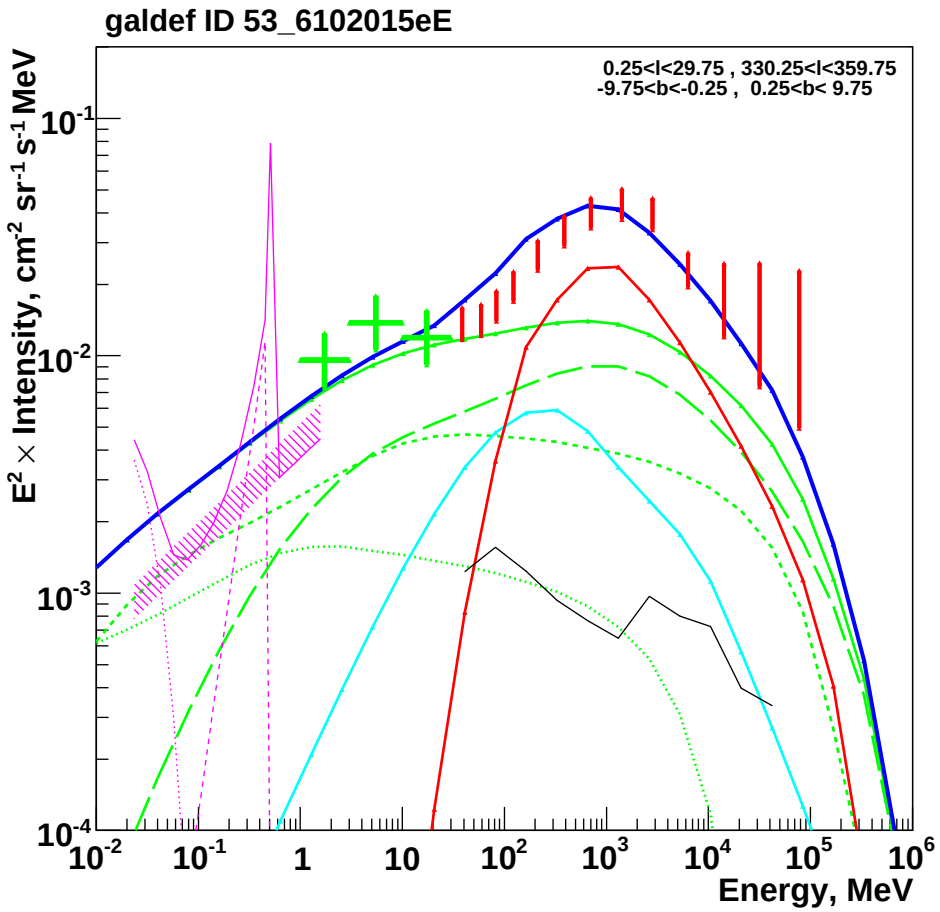

Figure 4.28: Gamma-ray spectrum calculated with the modified optimized electron spectrum with the break at 15 GeV compared with the data. It's visible an overprediction of gamma-ray at EGRET low energies, but still satisfactory. The spectrum calculated including secondary positrons and electrons. Line and data styles as for Fig. 4.3

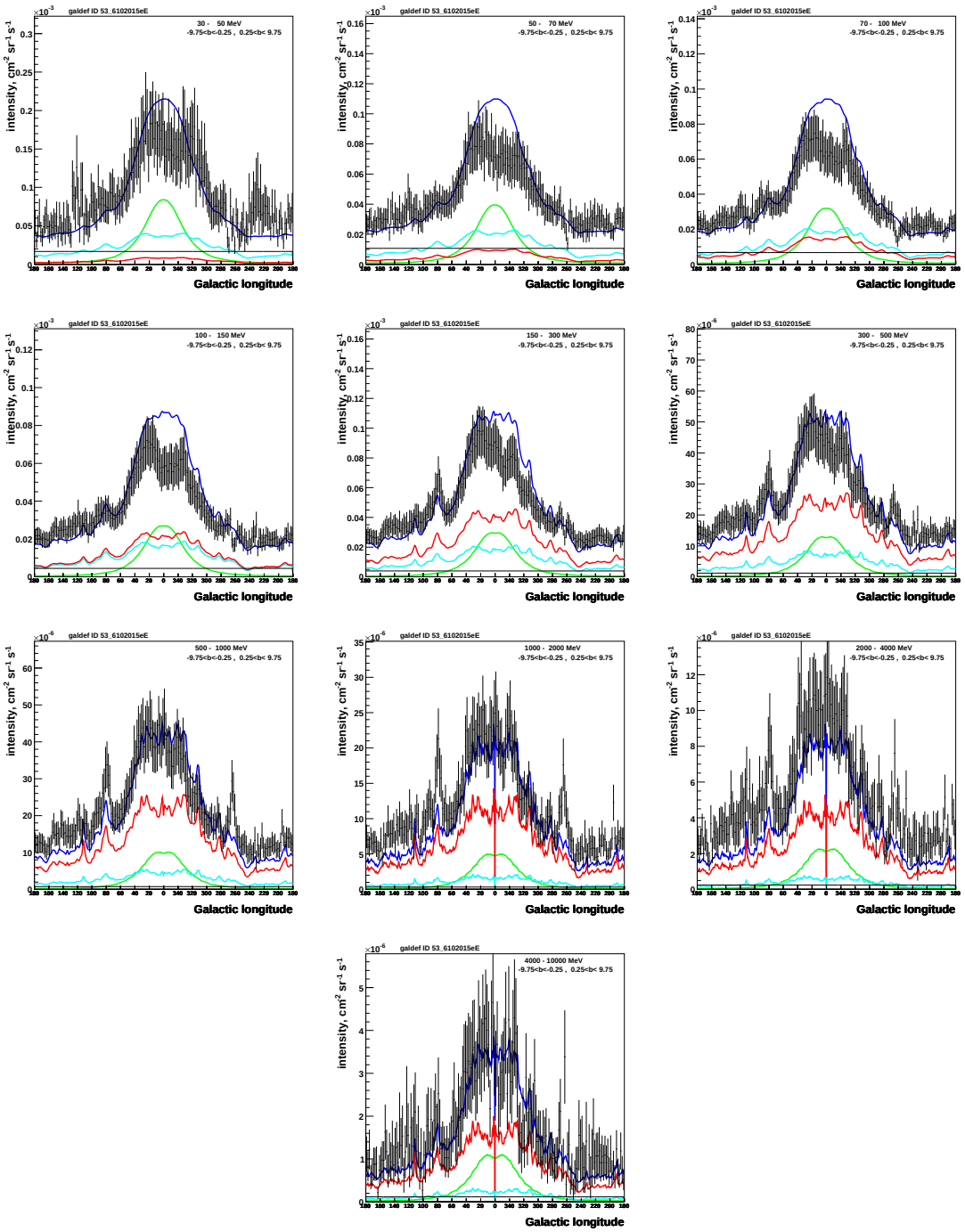

Figure 4.29: Longitude profiles ($|b| < 9$ deg) for the modified-optimized model with the break at 15 GeV, compared with data: darker vertical bars: EGRET data. The extragalactic background is added to the total prediction shown as an horizontal black line. The model components are pion decay (red line), IC (green line), bremsstrahlung (cyan line) and total (blue line). The profiles are calculated including secondary positrons and electrons.

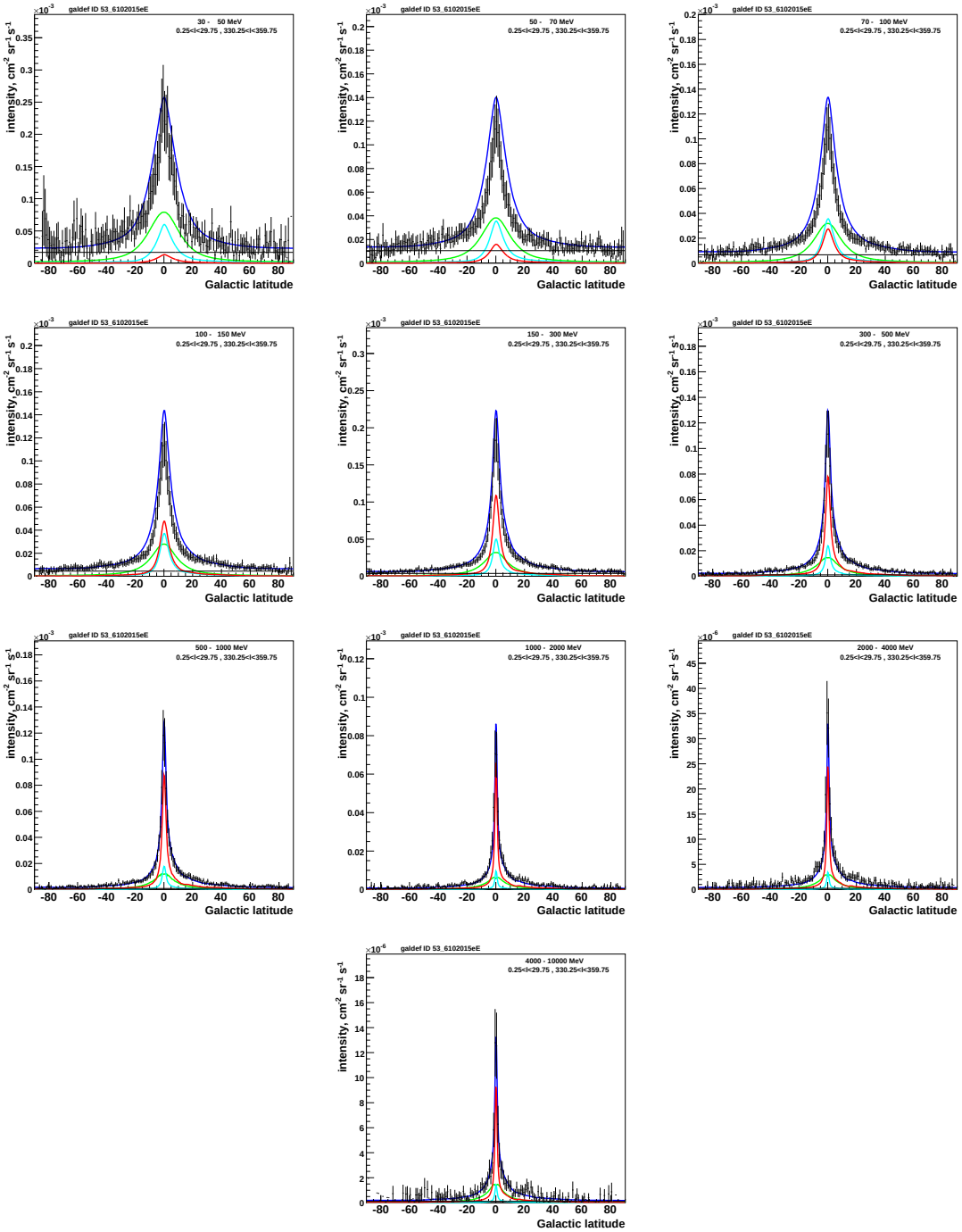

Figure 4.30: Latitude profiles (|l| <30 deg) for the modified-optimized model with the break at 15 GeV, compared with data: darker vertical bars: EGRET data. The extragalactic background is added to the total prediction shown as an horizontal black line. The model components are pion decay (red line), IC (green line), bremsstrahlung (cyan line) and total (blue line). The profiles are calculated including secondary positrons and electrons.

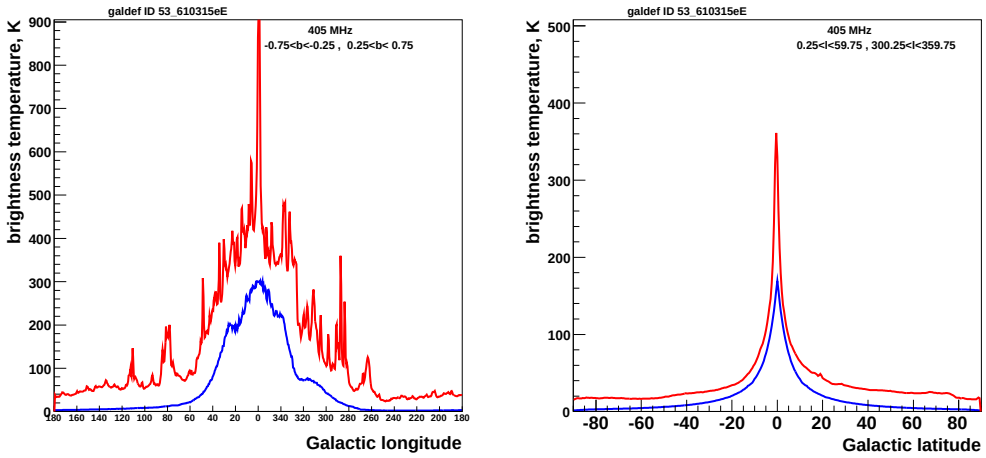

Figure 4.31: Synchrotron longitude and latitude profile at 408 GHz for the inner Galaxy and the total (random and regular) magnetic field. Blue lines are the models, while red lines are the data described in Fig 4.14. In this case the regular component intensity is taken as in model 2, while the random component varies proportionally with the regular field with 0.57 as scaling factor. This assumption produces more modulation in the expected emission.

CONCLUSIONS AND OUTLOOK

In the first part of this work I presented a theoretical model of the diffuse gamma-ray emission by inverse Compton scattering of cosmic-ray electrons on the radiation field around stars. This is the first time this effect has been analyzed. Spectra of gamma-ray emission of stars of different spectral types have been obtained. The most luminous stars within 600 pc have been selected from the Hipparcos catalogue and a list of possible candidates to be detected by GLAST has been produced. The work also showed how the large uncertainties in some parameters of the stars affect the predictions. Even if the predicted flux is below the GLAST threshold, the contribution of the most luminous stars is non-negligible and they can produce significant fluctuations. I developed a model of the Cygnus OB2 association and estimated the inverse-Compton emission. I found the flux to be detectable by GLAST. The spectrum obtained is comparable with the total IC emission from the Cygnus region and the extragalactic background, proving the importance of this effect for OB associations. This study combined with GLAST observations can help in understanding the sources that contribute to the Galactic diffuse emission and cosmic-ray propagation.

I then made a detailed model of the inverse Compton emission in the heliosphere using the anisotropic scattering formulation and the solar modulation of cosmic ray electrons. The latter has been widely studied, but is still not completely understood. Hence, I took into account different models of solar modulation in order to give a more useful description for the analysis of the EGRET data. I studied the solar emission using the EGRET database, accounting for the effect of the emission from 3C 279, the moon, the solar disk emission and other sources, which interfere with the solar emission. The technique has been tested on the lunar gamma emission that is produced by cosmic ray interactions with the lunar surface, giving results consistent with previous work. In this work a gamma-ray emission for the Sun was detected in the EGRET data for the first time. The analysis revealed the gamma ray

flux from the disk produced by cosmic-ray interactions on the solar surface to be in agreement with a previous theoretical model, that had not been confirmed by observations before. Moreover the most important result is that the extended inverse Compton emission was found as predicted, confirming my theory. In fact the observed intensity distribution and the flux are consistent with the predicted model, though within big error bars. The spectrum of the solar disk emission and the spectrum of the extended emission have been obtained. The spectrum of the moon is also given. Since the main uncertainty in the model is the electron spectrum, I wanted to prove which model of solar modulation describe better the EGRET data. Because of the limited sensitivity of EGRET, I could not distinguish between different conditions of solar modulation. This study is very important for deriving the gamma-ray extragalactic background and potentially gives the only method to study the modulation of Galactic cosmic rays so close to the Sun.

The last part of the thesis is focussed on the study of the diffuse emission from the Galaxy produced by cosmic-ray electrons. They give origin both to soft gamma-ray emission via inverse Compton and radio emission via synchrotron. In fact inverse Compton emission by scattering of GeV cosmic-ray electrons on the interstellar radiation field reproduces the non-thermal component of the hard X-ray to soft gamma ray emission from the Galactic ridge, detected by INTEGRAL. Both cosmic-ray primary electrons and secondary electrons and positrons contribute to the emission. The hard X-ray and the gamma-ray continuum are consistent with the predictions in both intensity and spectral index and the agreement in the spectral shape gives confidence that the mechanisms are well reproduced. Moreover the GALPROP code, has been extended to include detailed 3D magnetic field models in order to reproduce the diffuse synchrotron radiation from the Galaxy. A first analysis of the Galactic synchrotron emission produced by the electrons on the new Galactic magnetic field model was given and some information on the electron spectrum gained. The electron spectrum has been modified to agree with the new radio data. The new electron spectrum is called modified-optimized electron spectrum. However, it may be improved in future to match both the forthcoming gamma-ray and synchrotron data. In addition this study shows also that the absolute value and spatial variation of the magnetic field can be adjusted to get a better fit to the main radio surveys for the longitude and latitude profiles.

In outlook, my study performed in this thesis can be taken as basis for future improvements and discoveries.

In addition to OB associations, open clusters are concentrations of young stars surrounded by high density clouds. They contain many early-type stars (OB and Wolf-Rayet type) which produce strong radiation fields and energetic winds and are regions of star formation. Hence, a more detailed study of these regions is needed in view of the upcoming GLAST data. With GLAST it will be important to search for gamma-ray excesses at the positions of OB associations and evaluate the positional coincidences with multi-wavelength observations and comparison with theoretical models. For cases of no detection, the upper limits can be used to constrain the theoretical models.

With GLAST it will be possible to improve the study of the gamma-ray emission from the Sun, not only as a gamma-ray background contribution, but also for heliospheric physics and dark matter investigation. GLAST will detect daily the solar extended emission when the Sun is not close to the Galactic plane. In a few months it will be possible to distinguish between models of modulation. This study of the solar emission with GLAST is the only way to probe the modulation of cosmic-ray electrons in the near proximity of the Sun. Since the solar inverse-Compton emission depends on the electron spectrum and its modulation within the heliosphere, observations in different directions from the Sun can be used to determine the electron spectrum of cosmic rays at different position, even very close to the Sun. The determination of the cosmic-ray spectrum is important also for models of the gamma-ray diffuse emission from the Galaxy, helping to test the Galactic cosmic-ray spectrum. Moreover above 100 MeV the all sky average solar emission is about 10% of the extragalactic emission, and hence is also important for studies on Dark Matter. This extended emission can be a confusing background for other kinds of emission and has to be taken into account for diffuse background studies. Since the diffuse extragalactic background is weak compared to the Galactic background, its determination depends on the model of the Galactic diffuse and the solar diffuse contribution. The GLAST mission covers the range 20 MeV - 300 GeV with a sensitivity two orders of magnitude better than EGRET. In contrast to the EGRET analysis, with the GLAST sensitivity a time resolution study will be possible to follow the time variation of other sources coming close to the Sun and modelling the diffuse Galactic emission with GALPROP. By using the model of the Galactic diffuse emission, the Sun and the sources fitted with GLAST observations one can estimate the residual

extragalactic emission. Also a few normal galaxies will be detected by GLAST and they can be modelled using GALPROP-type models. Hence, it is possible also to investigate if such a background can be accounted for by a sum of various classes of discrete objects, or if a diffuse component of extragalactic gamma-ray emission is required.

An important question is still open on the Galactic gamma-ray diffuse emission. For example the spectrum of gamma-rays calculated under the assumption that the proton and electron spectra in the Galaxy resemble those measured locally (conventional model), reveals an excess at 1 GeV in the EGRET spectrum, the so-called GeV excess. Since the excess is seen with the same spectrum in all sky directions, it can be explained with very different assumptions: adjustments in the injection spectra of protons and electrons (optimized model), with respect to the local interstellar spectrum or an error in the estimation of the EGRET sensitivity at energies above 1 GeV. Only with GLAST it will be possible to increase the quality and accuracy of the gamma-ray data. To conclude, in the next few years the new missions will increase the quality and accuracy of cosmic-ray data (PAMELA), gamma-ray (GLAST, and high energy telescopes) and radio (PLANCK), so that elaborate models such as those presented here and a parallel study of the observational data is very promising.

Bibliography

CHAPTER 1

Berezhko, E. G., & Völk, H. J. 1997, Astroparticle Physics, 7, 183

Berezinskii, V. S., Bulanov, S. V., Dogiel, V. A., & Ptuskin, V. S. 1990, Amsterdam: North-Holland, 1990, edited by Ginzburg, V.L.,

Berezinsky, V., Gazizov, A., & Grigorieva, S. 2004, Nuclear Physics B Proceedings Supplements, 136, 147

Gaisser, T. K., & Stanev, T. 2006, Nuclear Physics A, 777, 98

Greisen, K. 1966, Physical Review Letters, 16, 748

Gaisser, T. K., & Stanev, T. 2006, Nuclear Physics A, 777, 98

Hess, V. F. 1922, Physical Review , 19, 73

Hess, V. F. 1932,Journal of Geophysical Research, 37, 399

Hillas, A. M. 2005, Journal of Physics G Nuclear Physics, 31, 95

Kampert, K.-H. 2007, Nuclear Physics B Proceedings Supplements, 165, 294

Kobayashi, T., Nishimura, J., Komori, Y., & Yoshida, K. 2001, Advances in Space Research, 27, 653

Longair, M. S. 1994, Cambridge University Press, Vol 2

Millikan, R. A., & Bowen, I. S. 1926, Physical Review , 27, 353

Peters, B. 1959, Nuovo cimento, Suppl., 14:No. 2, 436

Strong, A. W., Moskalenko, I. V., & Reimer, O. 2004, ApJ , 613, 956

Strong, A. W., Moskalenko, I. V., & Ptuskin, V. S. 2007, Ann. Rev. Nuc. Part. Sci., 57, 285

Zatsepin, G. T., & Kuz'min, V. A. 1966, Soviet Journal of Experimental and Theoretical Physics Letters, 4, 78

CHAPTER 2

Abdo, A. A., et al. 2007, ApJL , 658, L33

Aharonian, F., et al. 2002, A&A , 393, L37

Aharonian, F., et al. 2005, Science, 307, 1938

Aharonian, F., et al. 2007, A&A , 467, 1075

Alcaraz, J., et al. 2000, Physics Letters B, 484, 10

Bednarek, W. 2007, MNRAS, 382, 367

Boezio, M., et al. 2000, ApJ 532, 653

Chen, W., & White, R. L. 1991 ApJ, 381, L63

Davidson, K., & Humphreys, R. M. 1997, ARAA, 35, 1

DuVernois, M. A. 2001, ApJ 559, 296

Fullerton, A. W., Massa, D. L., & Prinja, R. K. 2006, ApJ , 637, 1025

GLAST web-site, http://www glast.stanford.edu

Grimani, C., et. al. 2002, A&A 392, 287

The Hipparcos and Tycho Catalogues. ESA SP 1200 1997, http://www.rssd.esa.int/Hipparcos/catalog.html,

Knödlseder, J. 2000, A&A, 360, 539

Kobayashi, T. 1999, International Cosmic Ray Conference, 3, 61

Lamers, H. J. G. L. M., & Leitherer, C. 1993, ApJ, 412, 771

Moskalenko, I. V., & Strong, A. W. 2000, ApJ , 528, 357

Moskalenko, I. V., et al. 2007, Nuc. Phys. B. Supp., 173, 44

Orlando, E., & Strong, A. W. 2007, Ap&SS, 309, 359

Orlando, E., & Strong, A. W. 2007, ArXiv e-prints, 709, arXiv:0709.3841

Orlando, E., & Strong, A. W. 2008, A&A , 480, 847

The Pierre Auger Collaboration, et al. 2007, Science, 318, 938

Reimer, A. 2007, ArXiv e-prints, 710, arXiv:0710.3526

Scuderi, S., Panagia, N., Stanghellini, C., Trigilio, C., & Umana, G. 1998, A&A , 332, 251

Strong, A. W., & Moskalenko, I. V. 1998, ApJ , 509, 212

Strong, A. W., et. al. 2004, ApJ 613, 956

Strong, A. W., et. al. 2004, ApJ 613, 962

Torres, D. F. et al. 2004, ApJ 601, L75

Torres, D. F. 2006, ArXiv Astrophysics e-prints, arXiv:astro-ph/0611710

CHAPTER 3

Bevington, P. R., Robinson, D. K., & Bunce, G. 1993, American Journal of Physics, 61, 766

Caballero-Lopez, R. A., & Moraal, H. 2004, Journal of Geophysical Research (Space Physics), 109, 1101

EGRET web-site, http://heasarc.gsfc.nasa.gov/docs/cgro/egret/

Eparvier, F. G., & Woods, T. N. 2003, Solar Variability as an Input to the Earth's Environment, 535, 209

Fairbairn, M., Rashba, T., & Troitsky, S. 2007, Physical Review Letters, 98, 201801

Fujii, Z., & McDonald, F. B. 2005, Advances in Space Research, 35, 611

Gieseler, J et al. 2007, International Cosmic Ray Conference

Gleeson, L. J., & Axford, W. I. 1968, ApJ , 154, 1011

Hartman, R. C., et al. 1999, ApJS , 123, 79

Hudson, H. S., 1989, Proc Gamma Ray Observatory Workshop (Greenbelt: Goddard Space Flight Center), 4-351

Jokipii, J. R., & Thomas, B. 1981, ApJ , 243, 1115

Kunow, H., Wibberenz, G., Green, G., Müller-Mellin, R., Witte, M., Hempe, H., & Hasler, H. G. 1975, International Cosmic Ray Conference, 12, 4268

Mattox, J. R., et al. 1996, ApJ , 461, 396

McDonald, F. B., Fujii, Z., Heikkila, B., & Lal, N. 2003, Advances in Space Research, 32, 633

Morales-Olivaresi, O.G. & Caballero-Lopez, R.A. 2007, International Cosmic Ray Conference, in press.

Moskalenko, I. V., Porter, T. A., & Digel, S. W. 2007, ApJL , 664, L143

Moskalenko, I. V., & Strong, A. W. 2000, ApJ , 528, 357

Moskalenko, I. V., & Porter, T. A. 2007, ApJ , 670, 1467

Müller-Mellin, R., Witte, M., Hempe, H., Kunov, H., Wibberenz, G., & Green, G. 1977, International Cosmic Ray Conference, 11, 214

Oncica, A., Popescu, M. D., Mierla, M., & Mariş, G. 2002, Solar Variability: From Core to Outer Frontiers, 506, 193

Orlando, E., & Strong, A. W. 2007, Ap&SS, 309, 359

Orlando, E., Petry, D., & Strong, A. 2007, American Institute of Physics Conference Series, 921, 502

Orlando, E., & Strong, A. W. 2007, ArXiv e-prints, 709, arXiv:0709.3841

Orlando, E., & Strong, A. W. 2008, A&A , 480, 847

Petry, D. 2005, High Energy Gamma-Ray Astronomy, Proceedings of the conference, 745, 709

Seckel, D., Stanev, T., & Gaisser, T. K. 1991, ApJ , 382, 652

Strong, A. W., Diehl, R., Halloin, H., Schönfelder, V., Bouchet, L., Mandrou, P., Lebrun, F., & Terrier, R. 2005, A&A , 444, 495

Strong, A. W. 1985, A&A , 150, 273

Strong, A. W., & Moskalenko, I. V. 1998, ApJ , 509, 212

Strong, A. W., Moskalenko, I. V., & Reimer, O. 2004, ApJ , 613, 956

Strong, A. W., Moskalenko, I. V., & Reimer, O. 2004, ApJ , 613, 962

Thompson, D. J., Bertsch, D. L., Morris, D. J., & Mukherjee, R. 1997, Geogr. Res., 102, 14735

Wilks, S. S. 1938, Ann. Math. Stat., 9, 60

CHAPTER 4

Abdo, A., et al. 2007, ApJ , 658, L33

Aharonian, F., et al. 2007, Nature, 439, 695

Baes, M. & Dejonghe, H. 2001, MNRAS, 326, 722

Beacom, J. F., & Yüksel, H. 2006, PRL, 97, 071102

Berezinskii, V. S., Bulanov, S. V., Dogiel, V. A., & Ptuskin, V. S. 1990, Amsterdam: North-Holland, 1990, edited by Ginzburg, V.L., Astrophysics of Cosmic Rays

Bleach, R.D., et al. 1972, ApJ , 174, L101

Bohlin, R. C., Savage, B. D., & Drake, J. F. 1978, ApJ , 224, 132

Bouchet, L., et al. 2005 ApJ , 635, 1103

Bouchet, L., Jourdain, E., Roques, J.-P., Strong, A., Diehl, R., Lebrun, F., & Terrier, R. 2008, ApJ , 679, 1315

Dermer, C. D. 1986, ApJ , 307, 47

Dermer, C. D. 1986, A&A , 157, 223

Dogiel, V.A., et al. 2002, A&A , 382, 730

Dogiel, V.A., et al. 2002, ApJ , 581, 1061

Draine, B. T. & Li, A. 2001, ApJ , 551, 807

Dwek, E., et al. 1997, ApJ , 475, 565

Ebisawa, K., et al. 2001, Science, 293, 1633

Ebisawa, K., et al. 2006, ApJ , 635, 214

Freudenreich, H. T. 1998, ApJ , 492, 495

Garwood, R. & Jones, T. J. 1987, PASP, 99, 453

Gilli, R., Comastri, A., & Hasinger, G. 2007, A&A , 463, 79

Gondolo, P., et al. 2004, J. Cosmology Astropart. Phys. 7,8

Hams, T., et al. 2007, Proc. $30^{\rm th}$ ICRC, Merida, in press

Han, J. L., & Qiao, G. J. 1994, A&A , 288, 759

Hands, A. D. P., et al. 2004, MNRAS, 351, 31

Haslam, C. G. T., Salter, C. J., Stoffel, H., & Wilson, W. E. 1982, A&A Supplement Series, 47, 1

Henyey, L. G. & Greenstein, J. L. 1941, ApJ , 93, 70

Hickox, R. C., & Markevitch, M. 2007, ApJL , 661, L117

Hiltner, W. A. 1949, ApJ , 109, 471

Hunter, S. D., et al. 1997, ApJ , 481, 205

INTEGRAL web-site, www.rssd.esa.int/Integral

Kamae, T., et al. 2005, ApJ , 620, 244

Kelner, S. R., et al. 2006, Phys. Rev. D., 74, 034018

Kinzer R. L., et al. 1999, ApJ , 515, 215

Kinzer R. L., et al. 2001, ApJ , 559, 282

Knödlseder, J., et al. 2005, A&A , 441, 513

Koch, H. W., & Motz, J. W. 1959, Rev. Mod. Phys., 31, 920

Koyama, K., et al. 1986, PASJ, 38, 503

Krivonos, R., et al. 2007, A&A , 463, 957

Kuiper, L., et al. 2006, ApJ , 645, 556

Kylafis, N. D. & Bahcall, J. N. 1987, ApJ , 317, 637

Lebrun, F. 2004, Nature, 428, 293

Li, A. & Draine, B. T. 2001, ApJ , 554, 778

Longair, M. S. 1994, Cambridge University Press, Vol 2

Lorimer, D. R. 2004, Proc. COSPAR, 35, 1321

Mashnik, S. G., et al. 2004, Adv. Space Res., 34, 1288

Michelson, P. F. 2007, AIP Conf. Proc., 921, First Int. GLAST Symp., ed. Ritz, S. et al. (Melville: AIP), 8

Miville-Deschenes, M., Ysard, N., Lavabre, A., Ponthieu, N., Macias-Perez, J. F., Aumont, J., & Bernard, J. P. 2008, ArXiv e-prints, 802, arXiv:0802.3345

Moskalenko, I. V., & Strong, A. W. 1998, ApJ , 493, 694

Moskalenko, I. V., & Strong, A. W. 2000, ApJ , 528, 357

Moskalenko, I. V., et al. 2002, ApJ , 565, 280

Moskalenko, I. V., Strong, A. W., & Reimer O. 2004, Astrophysics and Space Science Library, vol 304, 279

Moskalenko, I. V., Porter, T. A., & Strong, A. W. 2006, ApJ , 640, L155

Moskalenko, I. V., et al. 2007, Nuc. Phys. B. Supp., 173, 44

Page, L., et al. 2007, ApJS , 170, 335

Pickles, A. J. 1998, PASP, 110, 863

Porter, T. A., Moskalenko, I. V., & Strong, A. W. 2006, ApJL , 648, 29

Porter, T. A., Moskalenko, I. V., Strong, A. W., Orlando, E., & Bouchet, L. 2008, ApJ , 682, 400

Press, W. H., et al. 1992, Numerical Recipes in FORTRAN. The art of scientific computing, ed. Cambridge Univ. Press

Ptuskin, V. S., et al. 2006, ApJ , 642, 902

Purcell, W. R., et al. 1996, A&AS, 120, 389

Rand, R. J., & Kulkarni, S. R. 1989, ApJ , 343, 760

Revnivtsev, M., et al. 2006, A&A , 452, 169

Revnivtsev, M. & Sazonov, S. 2007, A&A , 471, 159

Revnivtsev, M., et al. 2007, A&A , 473, 857

Ritz, S. 2007, in AIP Conf. Proc., 921, First Int. GLAST Symp., ed. Ritz, S. et al. (Melville)

Seo, E. S. & Ptuskin, V. S. 1994, ApJ , 431, 705

Sodroski, T. J., et al. 1997, ApJ , 480, 173

Strong, A. W., & Moskalenko, I. V. 1998, ApJ , 509, 212

Strong, A. W., Moskalenko, I. V., & Reimer, O. 2000, ApJ , 537, 763

Strong, A. W., et al. 2003, A&A , 411, L447

Strong, A. W. 2003, A&A , 411, L127

Strong, A. W., Moskalenko, I. V., & Reimer, O. 2004, ApJ , 613, 956

Strong, A. W., Moskalenko, I. V., & Reimer, O. 2004, ApJ , 613, 962

Strong, A. W., et al. 2004, Proc. 5th INTEGRAL Workshop, ESA SP-552, eds. V. Schönfelder, G. Lichti & C. Winkler, p. 507; astro-ph/0405023

Strong, A. W., et al. 2004, A&A , 422, L47

Strong, A. W., et al. 2005, A&A , 444, 495

Strong, A. W., Moskalenko, I. V., & Ptuskin, V. S. 2007, Ann. Rev. Nuc. Part. Sci., 57, 285

Terrier, R., et al. 2004, 5th INTEGRAL Workshop on the INTEGRAL Universe, 552, 513

Tinyakov, P. G., & Tkachev, I. I. 2002, Astroparticle Physics, 18, 165

Wainscoat, R. J., et al. 1992, ApJS , 83, 111

Weingartner, J. C. & Draine, B. T. 2001, ApJ , 548, 296

Worrall, D. M., et al. 1982, ApJ , 255, 111